https://doi.org/10.35662/unine-thesis-2888

University of Neuchâtel, Switzerland
Faculty of Science
Center for Hydrogeology and Geothermics (CHYN)

and

Sorbonne University, France
ED 398 Géosciences Ressources Naturelles et Environnement

Direct simulation of non-additive variables on unstructured grids: the case of permeability

A thesis presented for the degree of

Doctor of sciences

by

Pauline MOURLANETTE

Directeurs de thèse :	Philippe Renard	University of Neuchâtel
	Benoît Nœtinger	IFPEN
Rapporteurs :	Insa Neuweiler	University of Hannover
	Guillaume Caumon	University of Lorraine
	Julien Straubhaar	University of Neuchâtel
Examinateurs :	Valérie Plagnes	Sorbonne University
	Pierre Biver	TOTAL
	Gérard Massonnat	TOTAL

Defended on the 23^{rd} of September, 2020

UNIVERSITÉ DE NEUCHÂTEL

Faculté des Sciences
Secrétariat-décanat de Faculté
Rue Emile-Argand 11
2000 Neuchâtel – Suisse
Tél : + 41 (0)32 718 21 00
E-mail : secretariat.sciences@unine.ch

IMPRIMATUR POUR THÈSE DE DOCTORAT

réalisée en cotutelle avec Sorbonne Université de Paris, France

La Faculté des sciences de l'Université de Neuchâtel autorise l'impression de la présente thèse soutenue par

Madame Pauline MOURLANETTE

Titre:

"Direct simulation of non-additive variables on unstructured grids: the case of permeability"

sur le rapport des membres du jury composé comme suit, selon la convention de cotutelle:

- Prof. titulaire Philippe Renard, co-directeur de thèse, Université de Neuchâtel, Suisse
- Dr Benoît Noetinger, co-directeur de thèse, IFPEN, Sorbonne Université, Paris France
- Prof. Guillaume Caumon, Université de Lorraine, Nancy, France
- Dr Julien Straubhaar, Université de Neuchâtel, Suisse
- Prof. Insa Neuweiler, Université d'Hanovre, Allemagne
- Prof. Valérie Plagnes, Sorbonne Université, Paris, France
- Dr Pierre Biver, Total, France
- Dr Gérard Massonat, Total, France

Neuchâtel, le 12 octobre 2020

Le Doyen, Prof. A. Bangerter

"There's nothing you can make that can't be made. No one you can save that can't be saved. Nothing you can do, but you can learn how to be you in time. It's easy. All you need is love."

— John Lennon for the Beatles

Acknowledgements

I would like to thank Total for funding this research, in particular the research project Reservoir Earth Modeling for the financial and technical support and the team Geostatistics and Uncertainties for hosting me. This PhD results from the partnership between Total and the Association Nationale de la Recherche et de la Technologie (ANRT) under the CIFRE contract number 2017/0222. My PhD was made with a co-supervision from the Center for Hydrogeology and Geothermics (CHYN) of the University of Neuchâtel and the PhD school 398 GRNE from Sorbonne University. I would like to thank both of these schools for welcoming me and providing the technical and scientific resources for my work.

Remerciements

Je tiens à commencer mes remerciements par mes trois encadrants de thèse, sans qui cette aventure n'aurait pas existée.

Merci en premier lieu à Pierre Biver d'avoir cru en moi dès mon stage en 2016, alors que moi même je n'y croyais pas. Tes remarques et suggestions ont eu un impact immense sur la qualité de ma thèse, et m'ont permis de rendre aujourd'hui un travail dont je suis fière. Je sors grandie de cette expérience, notamment grace aux connaissances et à la rigueur que tu as su me transmettre.

Un grand merci ensuite à mon directeur de thèse Philippe Renard, pour son incroyable bienveillance. Merci pour la richesse de nos échanges scientifiques, et pour avoir toujours discuté avec moi d'égal à égal. Ta façon de valoriser les résultats, qu'ils soient bons ou mauvais, a été un grand réconfort dans les moments de doutes. Combiné avec ton exigence permanente envers mes travaux et tes contributions scientifiques nombreuses, je peux dire avec assurance que je n'aurais pas pu espérer de meilleur directeur de thèse.

Merci également à mon co-directeur de thèse Benoît Noetinger, pour sa connaissance pointue du sujet qui a permis de mettre en lumière les bons côtés et les failles de mon travail. Merci d'avoir ammené un aspect plus théorique à ma thèse, afin d'équilibrer avec le côté industriel.

Je tiens ensuite à remercier les membres de mon jury de thèse, en commençant par les rapporteur(e)s : Guillaume Caumon, Insa Neuweiler et Julien Straubhaar. C'est un honneur pour moi que vous vous soyez impliqués dans l'évaluation de mon travail. La soutenance,

tant redoutée au cours de la thèse, a été riche en échanges, et j'en ressort avec beaucoup d'idées et une confiance en mes capacités accrue. Merci également à Guillaume pour son implication pendant ma thèse et notamment lors de l'écriture de mon article. Je tiens aussi à remercier Valérie Plagnes, examinatrice et présidente du jury, pour sa bienveillance et son regard extérieur sur mon travail. Merci enfin à Gérard Massonnat, pour s'être impliqué en tant qu'examinateur lors de ma soutenance mais aussi tout au long de ma thèse, avec des remarques toujours pertinentes.

A Total, je tiens à remercier mes collègues pour leur pédagogie et leurs conseils divers. Merci donc à tous mes collègues du service Geostatistiques et Incertitudes pour s'être toujours assurés que ma thèse avance dans les meilleures conditions possibles. Merci également à mes collègues de mon projet de recherche, Reservoir Earth Modeling, et plus particulièrement à Jean-Paul Rolando, pour m'avoir chaleureusement accueillie et accompagnée durant mes trois années de thèse, ainsi qu'à David Ledez, pour ses conseils techniques et son suivi pertinant de mes travaux.

Enfin, j'adresse un grand merci à Simon Fuet, Stéphanie Berthelin et Dimitri d'Or d'Ephesia, qui ont toujours répondu à mes questions avec bienveillance et ont résolu avec une efficacité irréprochable certains de mes problèmes de code.

La réalisation de cette thèse, et sa réussite, je la dois à beaucoup de personnes. Je commence par Floriane, l'amie de toujours, merci de n'avoir jamais hésité à venir jusqu'à Pau pour m'offrir des distractions bienvenues, même si ça impliquait une marche arrière compliquée en bord de ravin. Merci à Pauline et Agathe, sans qui la prépa aurait eu une toute autre saveur. Vous avez été le supplément fromage de mon supplément jambon dans mon gratin de pâtes, ce petit truc en plus qui permet d'aller de l'avant. Merci à tous mes amis de Géol, trop nombreux pour être cités, mais en particulier à Typhaine, qui a su me requinquer, encore aujourd'hui, avec sa bonne humeur constante et communicative. Un grand merci à mes collocs de fin, ceux qui ont partagé mes dernier instants à l'école, Dan et Etienne, pour m'avoir accueillie à Putiers, soutenue dans les moments de doute et surtout nourrie à coup d'alligot. Enfin, un merci tout spécial aux Géol Num, pour cette année extraordinaire passée à vos côtés, et les conseils, blagues et encouragements partagés sur la TT et la GG depuis.

Après mes études, il y a eu la thèse. Cette thèse, je ne l'aurais pas traversée sans mes deux guides, Grégoire et Mikaël. Merci de m'avoir

appris a manoeuvrer pour sortir des moments compliqués la tête haute, notamment lorsque j'étais bloquée dans un peu trop de beurre et pas assez de sucre. Merci à mes super collègues, Natalia, Zinyat, Daniel et Norman, pour les moments de rire, mais aussi le sérieux dans lequel il était possible de travailler à vos côtés. Autour de moi, il y a eu d'autres personnes formidables, qui n'ont jamais, ou presque, hésité à venir m'aider à me battre contre mon environnement Eclipse, ce sont mes collègues et amis du bureau EnHM: Jean-Romain, Thomas, Alexandre, Natacha, et Guillaume. Je remercie également Jérôme, qui, avec le sourire et parfois de très bonnes crêpes, a su me sortir de plusieurs impasses avec mon code. Merci au duo inséparable, Emmanuel et Thomas, pour les afterworks pleins d'humour et surtout pour votre maniement du croco qui m'a obligée à devenir vigilante. Dans la lignée, je remercie Alix, pour m'avoir accueillie au Bourbaki palace avec de bons petits plats et un verre de vin les jours où ça devenait difficile, et les jours normaux aussi. Enfin, merci à mon acolyte de Neuchâtel, Dan, d'avoir rendu mes séjours en Suisse et ailleurs si agréables, et d'avoir maintenu mon contact avec l'unine en me racontant tout ce qu'il s'y passait.

Plus largement, cette thèse n'aurait pas été la même sans mes amis "palois". Je remercie Alysée, Antoine, Arthur, Gaby, Johanna, Salomé, Sara et tant d'autres pour les nombreux moments d'évasion. Mention spéciale à Samy, pour son écoute à la salle et en dehors, et son amitié sans failles du début à la fin de cette aventure. Merci également à mes nageuses et amies, Anne, Camille, Julie, Laura, Séverine, Sonia et Virginie, de m'avoir laissée me défouler sur elles lors des entrainements, et de me suivre dans presque toutes mes folies créatives.

Enfin, cette thèse ne serait rien sans ma famille. Papa, maman, merci d'avoir fait de moi la femme que je suis aujourd'hui. Merci papa, d'avoir toujours vu en moi ce qu'il y a de meilleur, de m'avoir encouragée et accompagnée dans toutes les étapes de ma vie. Merci maman, de m'avoir toujours écoutée, conseillée, encouragée, avec une infinie douceur et juste ce qu'il faut de fermeté. Merci à mes frères et soeurs, Jean, François, Jade et Léa, d'être les personnes formidables que vous êtes, de m'avoir portée jusqu'ici par votre amour et votre présence continue à mes côtés.

Je termine par celui qui deviendra mon mari dans quelques mois. Brieuc, je ne pourrais jamais exprimer en quelques mots toute l'admiration que j'ai pour toi et ta determination à accomplir de grande choses. Merci d'avoir su me soutenir jusqu'ici, et d'être toujours présent pour m'aider à avancer...

"Sometimes, you can't make it on your own"

Abstract

Uncertainties related to permeability heterogeneity can be estimated using geostatistical simulation methods. Usually, these methods are applied on regular grids with cells of constant size, whereas unstructured grids are more flexible to honor geological structures and offer local refinements for fluid-flow simulations. However, cells of different sizes require to account for the support dependency of permeability statistics (support effect).

This work presents a novel workflow based on the power averaging technique. The averaging exponent ω is estimated using a response surface calibrated from numerical upscaling experiments. Using spectral turning bands, permeability is simulated on points in each unstructured cell, and later averaged with a local value of ω that depends on the cell size and shape, but also on the proportion of each facies inside the cell.

The method is first illustrated on a synthetic case, with a single facies. The simulation of a tracer experiment is used to compare this novel geostatistical simulation method with a conventional approach based on a fine scale Cartesian grid. The results show the consistency of both the simulated permeability fields and the tracer breakthrough curves. The application to an industrial case with two facies is then presented and shows both consistent permeability fields and computational costs acceptable for the industry. Indeed, the computational cost for several realizations is much lower than the conventional approach based on a pressure-solver upscaling.

The method works for the presented cases, but its theoretical robustness can still be improved. A discussion on pressure solver upscaling parameters selection and power averaging limits is available in the conclusion, as well as a few research perspectives on multiple facies and non stationary proportions inclusion, the management of anisotropy and the extension to multiphase flow.

Résumé

Les incertitudes liées à l'hétérogénéité de la perméabilité peuvent être estimées par des méthodes de simulations géostatistiques. En général, ces méthodes sont implémentées sur des grilles régulières dont les cellules ont des tailles constantes. Cependant, l'utilisation de maillages non structurés, plus flexibles, permet une meilleure représentation des structures géologiques et des performances de simulations réservoir améliorées. Ces grilles possédant des cellules de tailles différentes, il est nécessaire de prendre en compte la sensibilité des statistiques de la perméabilité à la taille du support (effet de support).

Ce travail de thèse présente un nouveau workflow basé sur la moyenne en puissance de la perméabilité. Le coefficient de moyennage ω est estimé en utilisant une surface de réponse calibrée à partir d'expériences numériques d'upscaling. A l'aide des Spectral Turning Bands, la perméabilité est simulée sur des points dans chaque cellule non structurée, puis ces valeurs ponctuelles sont moyennées avec une valeur locale de ω qui dépend de la taille et la forme de la cellule traitée, mais aussi de la proportion de chaque facies dans la cellule.

La méthode est illustrée sur un cas synthétique à un seul facies. Une expérience de traceur est utilisée pour comparer cette nouvelle méthode à une approche conventionnelle basée sur une grille fine Cartésienne. Les résultats sont cohérents, tant d'un point de vu champs de perméabilité que courbes de production du traceur. La méthode est ensuite appliquée à un cas industriel avec deux facies. Les résultats montrent à la fois la cohérence des champs de permeabilité obtenus et des coûts de calcul acceptables pour l'industrie. En effet, ces coûts pour plusieurs réalisations sont bien plus faibles que ceux de l'approche conventionnelle basée sur un upscaling par solveur de pression.

La méthode est fonctionnelle dans les cas présentés, mais sa solidité peut encore être améliorée. Une discussion sur la sélection des paramètres d'upscaling et les limites de la loi en puissance peut être retrouvée en conclusion. Egalement, plusieurs perspectives sont présentées: l'inclusion de multiples facies et de proportions non-stationaires, la gestion des anisotropies ou encore l'extension de la méthode dans des cas multiphasiques.

Keywords

Permeability; Support effect; Unstructured grids; Power averaging; Upscaling; Geostatistics.

Mots-Clés

Perméabilité; Effet de support; Maillages non structurés; Loi en puissance; Upscaling; Géostatistique.

Contents

Chapter 1

Introduction

1.1 General context

Subsurface phenomena cannot be observed directly due to inaccessibility and scale issues. In hydrogeology, the high spatial variability of rock types and the associated permeability field, as well as the important spatial and temporal variability of fluid types and displacements, are main sources of uncertainties. Estimating these uncertainties is particularly important in a context of engineering design and decision making. Examples of applications include the management of over-exploited aquifers or the propagation of dangerous contaminants (de Marsily et al., 1998). Similar uncertainty issues coupled with decision-making are encountered in other applied geoscience engineering, such as oil and gas industry (Preux, 2016), CO_2 storage in aquifers (Michael et al., 2010; Akhurst et al., 2015), or geothermal energy production (Vogt et al., 2010; Quinlivan et al., 2015; Witter et al., 2019).

There are many ways to improve the quality of the subsurface models such as for example: more accurate and faster flow simulators, varying simulation supports, improved characterization of the parameter fields using improved inverse techniques, or assimilation of novel data types. This PhD thesis focuses on the spatial modeling of permeability fields. Indeed, due to rock heterogeneity, a measurement at one location is usually not sufficient to determine accurately the value at another location. To assess the uncertainty related to this interpolation problem, one can use geostatistical simulation methods (Deutsch and Journel, 1992; Goovaerts, 1997; Chilès and Delfiner, 2012). Common algorithms use a mesh as a support that represents the area of study. Each cell of this mesh has to be populated with ground properties. In places where

measurements are known from wells or human exploration, cells are assigned an exact value (not considering measurement errors). In between those cells, geostatistical simulations are used to derive the most realistic or plausible set of values regarding the statistics of the geostatistical model.

Classical meshes used for simulation, widely called regular structured grids, are composed of hexahedral cells in three dimensions. Typically, their cells all share the same size and shape. They are practical for the rapidity of calculation but imply an approximation on the geometry of the geological structures. To solve this problem, more flexible grids have been developed and allow improving numerical precision around the areas of interest such as wells and the geometrical representation of geological structures. These grids, that can be either irregular structured or unstructured grids, can have cells of different shapes and sizes.

The main drawback of unstructured grids is that, by having cells of different sizes, they call for more complexity in the geostatistical simulations. Indeed, the statistics of the permeability (and the other variables) are support dependent (i.e., in stationary settings, smaller cells tend to have a smaller internal variability and larger inter-cell variability). This support effect is well documented both theoretically and experimentally (Matheron, 1967a; Dagan, 1993; Tidwell and Wilson, 1997): the probability distribution function of the permeability is different for cells of different volumes, as well as the spatial correlation. This phenomenon highlights the role of the interaction between the geometry and size of the block and the integral scale that may characterize the internal structure of the reservoir. If these support effects are not accounted for, the simulation of the petrophysical variables can result in distorted and possibly wrong fluid paths. It is therefore crucial to use appropriate geostatistical methods for unstructured grids.

The simplest approach to account for the support effect implies an underlying fine-scale grid to represent the domain of interest and a numerical upscaling. However, modeling the domain of interest at measurement-support (typically a few cubic centimeter for petrophysical core measurements) is particularly challenging in terms of time and memory resources. To bypass this problem, a solution is to simulate directly the property on the unstructured grid accounting for support effect. But a second challenge arises, coming from the non-additivity of permeability. A property is said to be additive (porosity for example) when the averaging can be carried out using a (weighted) arithmetic mean. This is possible because quantities of the underlying physical

property can be added together in a meaningful manner. For example, volumes of pores in two parts of a sample can be added together to produce the total volume of pores in the sample. For additive properties, some direct geostatistical simulation methods exist and be discussed in this manuscript. However, they can not be applied directly to non-additive variables such as permeability.

1.2 Objectives and main contribution

The aim of this PhD thesis is to introduce a new approach to simulate permeability directly on any unstructured grid, accounting for the support effect and avoiding the use of an underlying fine grid.

The method transforms permeability into an additive property using power averaging with local exponents which depend on the geometry and size of the cells. The exponents are estimated using a limited set of numerical experiments and an experimental design approach. The simulation process then relies on a Spectral Turning Bands methodology (Mantoglou and Wilson, 1982; Emery and Arroyo, 2017). This overall strategy permits to generate efficiently a set of realizations on the unstructured grid. The approach is illustrated and tested in the case of the simulation of a multigaussian field. In a second step, it is extended to a binary media by including proportions of facies in the estimation of power averaging local exponents. The binary media is modeled in two steps. First, the facies are obtained using a pluriGaussian technique, and then the two facies are filled with multiGaussian fields for the permeabilities.

Both methods, i.e. with and without facies, are applied to a synthetic case. The method without facies is compared by running tracer test simulations on the unstructured grid and on a classical fine grid model. It gives similar results, with a reasonable difference due to the coarser cells of the unstructured grid.

Finally, we emphasize that the two methods have been implemented in the Sismage environment, the industrial geomodelling platform of Total, and are already applicable in a practical, industrial, context. The results obtained on a real field study that are presented in this work illustrate this aspect.

1.3 Structure of the thesis

This PhD thesis contains seven main chapters (excluding introduction and conclusion):

- Chapter 2 provides a state of the art concerning the main concepts and tools that are used in this thesis such as the types of grids, existing geostatistical simulations on unstructured grids and upscaling of permeability.
- Chapter 3 presents two preliminary studies concerning the estimation of the exponents ω. The first part aims at choosing a numerical upscaler and the second assesses the main factors controling the variations of the power averaging exponent.
- Chapter 4 contains the main novel part of the work. It explains in detail the proposed methodology for simulating the permeability directly on unstructured grids.
- In Chapter 5, the applicability of the method is illustrated on a synthetic case including tracer test simulations and an analysis of the computation times. The content of Chapters 4 and 5 has been published in the journal Advances in Water Resources (Mourlanette et al., 2020).
- Chapter 6 introduces the extension of the method to binary media by taking into account facies proportions in the power averaging exponent determination.
- Chapter 7 describes the tests of the extended method on the same synthetic case as in Chapter 5.
- Finally, Chapter 8 presents an application of the methods (without and with facies) to a real case study called Field X. It includes the geological description of the field as well as simulation results.

The method with a single facies (Chapter 4) was presented in the Fourth EAGE Conference on Petroleum Geostatistics, Florence, Italy, in an oral presentation corresponding to the following extended abstract:

Mourlanette, P., Biver, P., Renard, P. & Noetinger, B. (2019). Direct Geostatistical Simulation on Unstructured Grids II: A Proposal for Non-additive Variables. Conference Proceedings, *Petroleum Geostatistics 2019*, p.1-5.

Chapter 2

Simulation on unstructured grids and change-of-support for permeability

This chapter summarizes the key concepts and knowledge required to understand the context of the proposed method. After defining and presenting the different types of grids, we will explain the existing methods to perform geostatistical simulations on unstructured ones. Then, as permeability is strongly support-dependent and unstructured grids cells have different sizes, we review existing approaches for the change of support of permeability.

2.1 Types of meshes

To represent the spatial variability and solve flow and transport equations with numerical methods, a mesh is used and its cells are populated with petrophysical properties. In this section, we will describe the types of meshes that are commonly used in the oil and gas industry. A more complete overview of meshes for geomodelling is available in Bennis et al. (2013). Generally, meshes are classified in three categories: structured, unstructured and hybrid. Hybrid meshes will not be presented here, as they are not used in this manuscript. They combine several types of elements: regular hexahedral cells and more flexible cells such as tetrahedra or pyramids, more details can be found in Botella (2016).

2.1.1 Structured grids

Classical meshes used in geostatistics are called *structured grids*. A mesh is qualified as *structured* if there is a regular connectivity between all its vertices, i.e. if its inner vertices all have the same number of neighbours (e.g. Hirasaki and O'Dell, 1970; Caumon et al., 2005) (Fig. 2.1 and Fig. 2.2). In this case, we say that a vertex's neighbors are known implicitly, because they can be deducted by construction.

A mesh can be *regular structured*, which means that *its cells all share the same size*. If the elements of the grid are squares in 2D or cubes in 3D, the grid is called Cartesian (Fig. 2.1a). The elements of regular structured grids can also be rectangles (or rectangular cuboids in 3D) (Fig. 2.1b), regular triangles like isosceles or equilateral triangles (Fig. 2.1c), or hexagons (Fig. 2.1d).

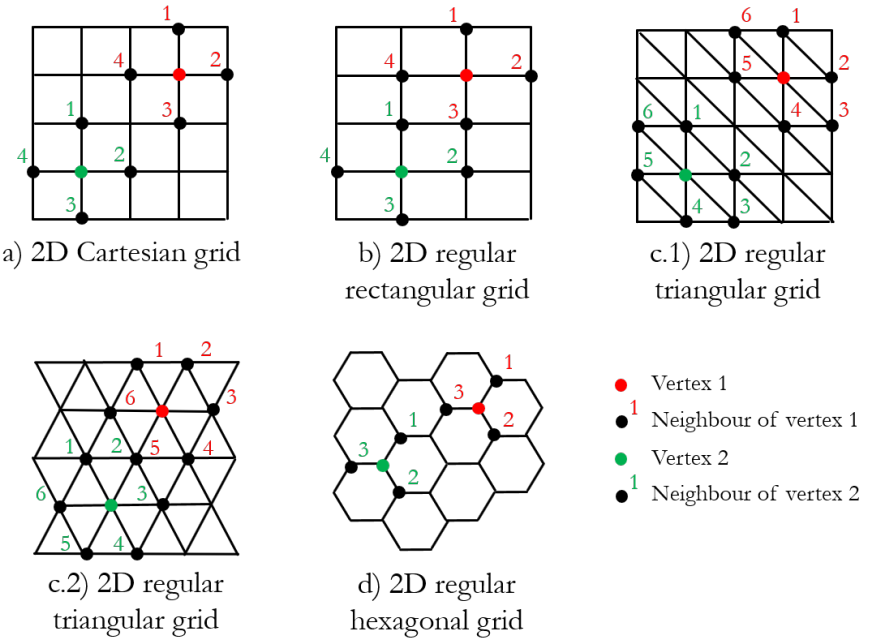

Figure 2.1: Examples of regular structured grids in 2D: a) Cartesian; b) rectangular; c) triangular with c.1) isosceles triangles and c.2) equilateral triangles; d) hexagonal. All vertices (here we only represented two vertices, one green and one red), have the same number of neighbours.

A mesh can also be *irregular structured* or *stratigraphic*, which means that, while inner vertices still have the same numbers of neighbours, the

cells can have different sizes and shapes (Fig. 2.2). The use of distorted hexahedra allows a better representation of some geological features. Cells can be rectangular but of different sizes, giving an irregular rectangular grid also called "tartan" grid (Fig. 2.2a). They can also have any quadrilateral or triangular shape in 2D, with linear or curvilinear edges (Fig. 2.2b and c).

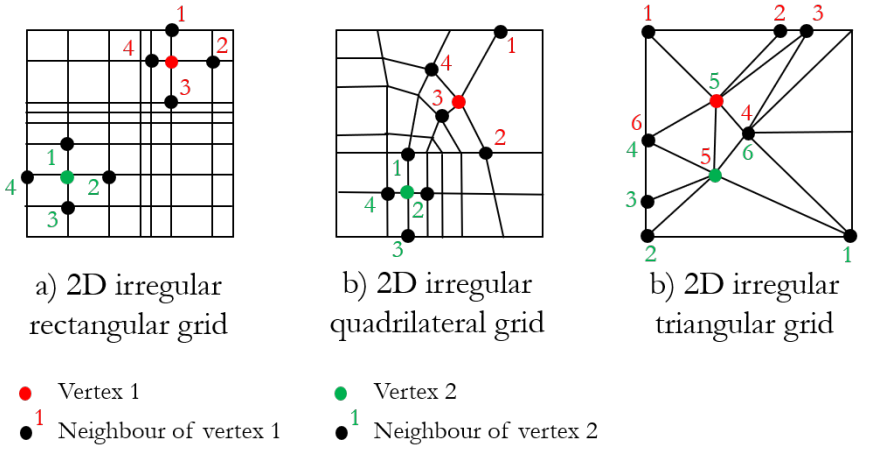

Figure 2.2: Examples of irregular structured grids in 2D: a) rectangular; b) quadrilateral; c) triangular. All vertices (here we only represented two vertices, one green and one red), have the same number of neighbours.

Regular and irregular structured grids are practical for the rapidity of calculation but they present some drawbacks: some cells can be degenerated for high thickness variations, the geometry of the intersections between faults or wells and the geological structure are approximated, and the constant cell volume hypothesis used in geostatistical modeling is not honored (Bertoncello et al., 2008).

2.1.2 Unstructured meshes

To address the above-mentioned issues, *unstructured grids* can be used, where *each vertex can have a different number of neighbours* (e.g. Löhner, 1997) (Fig. 2.3). The grid has an explicit definition, in which each node position and each polyhedron composition is given. The cell's sizes can vary. Indeed, the areas that present more interest or stronger variations for flow estimations can be refined and other parts coarsened (Palagi and Aziz, 1994; Heinemann, 1994; Prévost et al., 2005). Usu-

ally, to minimize numerical errors, the grid is refined around wells or faults but it can also be optimized based on flow patterns (Mlacnik et al., 2003). In addition, the cells can have various shapes such as tetrahedron or Voronoï polyhedron, offering more flexibility to adapt to geological heterogeneities (Blessent et al., 2011; Merland et al., 2014). The particularity of a centroïdal Voronoï mesh is that each of its cell is defined such that any point in this cell is closer to the center of the cell than to any other cell center. As a result, any segment joining two cell centers is perpendicular to the interface between these two cells, i.e. Voronoï grids are locally orthogonal. It is why they are also called perpendicular bisector grids or PEBI. This grid type is generally the preferred choice for reservoir simulations in the oil and gas industry, because its cell arrangement simplifies the solution of flow equations. A discussion on Voronoï grids and reservoir simulations is available in Palagi and Aziz (1994).

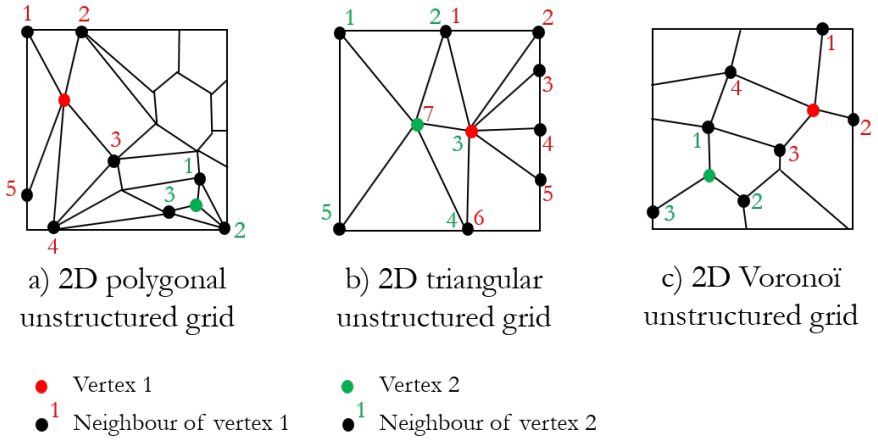

Figure 2.3: Examples of unstructured grids in 2D: a) polygonal; b) triangular; c) Voronoï. Vertices (here we only represented two vertices, one green and one red), have a different number of neighbours.

In this manuscript, two types of unstructured meshes will be used: a 2.5D Voronoï mesh, i.e. a mesh with Voronoï cells extruded vertically (Fig. 2.4a), and a 2.5D prismatic mesh, with triangular based prisms (Fig. 2.4b). "Extruded" means that the grid is designed in two dimensions and projected along depth. The methodology developed, however, is not restricted to these types of meshes.

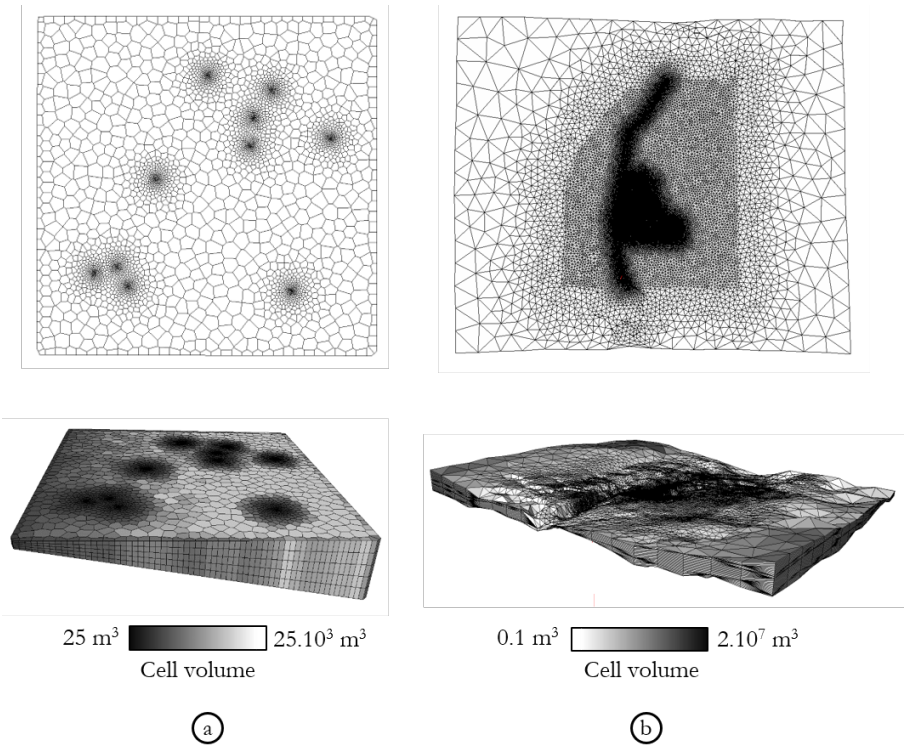

Figure 2.4: Two grids used in the manuscript: a) 2.5D Voronoï grid and b) 2.5D prismatic grid, in top and perspective views.

2.2 Geostatistical simulations on unstructured grids

The statistics of permeability (and other variables) are support dependent: in stationary settings, smaller cells tend to have a smaller internal variability and larger inter-cell variability. This *support effect* is well documented both theoretically and experimentally (Matheron, 1967a; Dagan, 1993; Tidwell and Wilson, 1997): the probability distribution function and the spatial correlation of permeability are different for cells of different volumes. Intuitively, small cells will follow the geostatistical properties defined at the point-support scale, keeping their local average and covariance. In opposition, for very large blocks having a size greater than the structures defined by point-support statistics, the associated permeability value may stabilize to the so-called effective permeability (Nœtinger and Gautier, 1998; Nœtinger and Zargar,

2004; Boschan and Nœtinger, 2012). It highlights the role of the interaction between the geometry and size of the block and the integral scale that characterizes the internal structure of the reservoir. If these support effects are not accounted for, the simulation of petrophysical variables can result in distorted and possibly wrong fluid paths. It is therefore crucial to use appropriate geostatistical methods for unstructured grids. Various methods already exist and they can be divided in two categories because of the nature of the simulated variables: continuous simulations, for variables such as porosity and permeability, and categorical simulations, i.e. facies simulation for instance. Continuous variables will be classified in two groups: the additive and non-additive variables. A property is said to be additive (porosity for example) when the averaging can be carried out using a (weighted) arithmetic mean. This is possible because quantities of the underlying physical property can be added together in a meaningful manner.

2.2.1 Use of a fine grid

The simplest approach to account for the support effect, referred to as "fine-scale simulation approach" by Zaytsev et al. (2015), is to use a fine scale Cartesian grid overlaid by a coarse, irregular or unstructured grid (Fig. 2.5a). The properties are simulated on the fine grid using a geostatistical model defined at the scale of the measurements (Fig. 2.5b). The values of the large cells are computed by upscaling, analytically or numerically, the values of the fine cells contained within the larger unstructured grid cells (e.g., He et al., 2002; Caumon et al., 2005; Durlofsky, 2005). Such a method to honor support effect is illustrated in Gross and Boucher (2015) for an arbitrary variable (Fig. 2.6).

If the property is additive, the averaging can be carried out using a direct arithmetic average of the underlying property. If the property is not additive (permeability for example), one needs to select an upscaling technique to obtain the value on the large cell. For instance, the upscaling can be based on a pressure solver that solves the local cell problem required by homogenization (e.g. de Marsily et al., 1998). It is the case in Manchuk et al. (2012), which uses multipoint flux approximation technique to obtain transmissibility matrices at the coarse scale. The particularity of Manchuk et al. (2012) method is that the underlying fine grid is a triangular grid that conforms to the coarse one (Fig. 2.7). The same idea is applied by Khan and Dawson (2004), but with an underlying fine Voronoï grid.

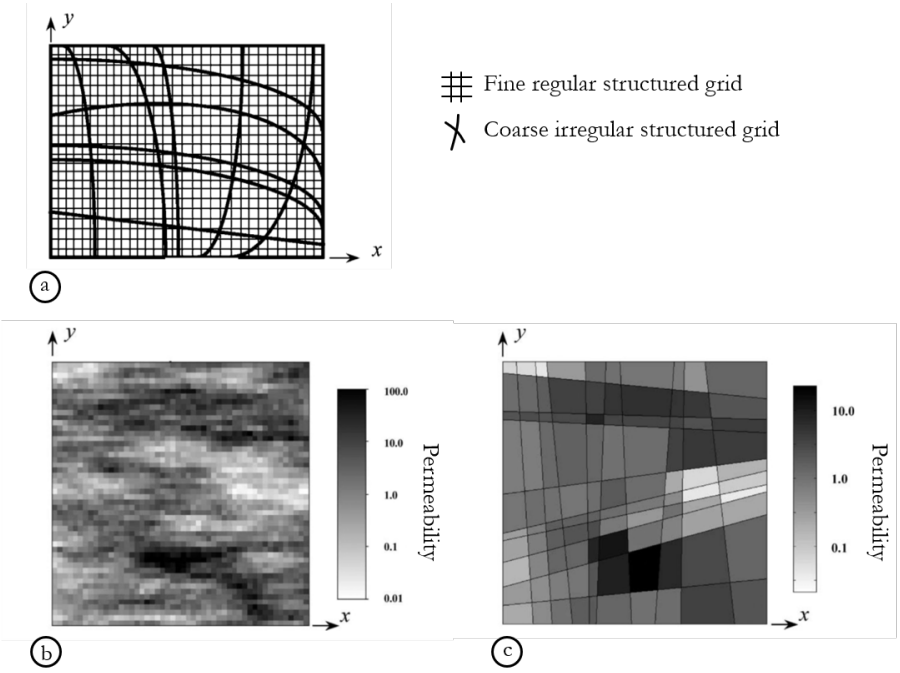

Figure 2.5: a) example of a coarse, irregular, quadrilateral grid overlaying a fine regular structured grid. b) Permeability simulated on the fine grid. c) Corresponding upscaled permeability on an irregular quadrilateral grid. Modified from He et al. (2002).

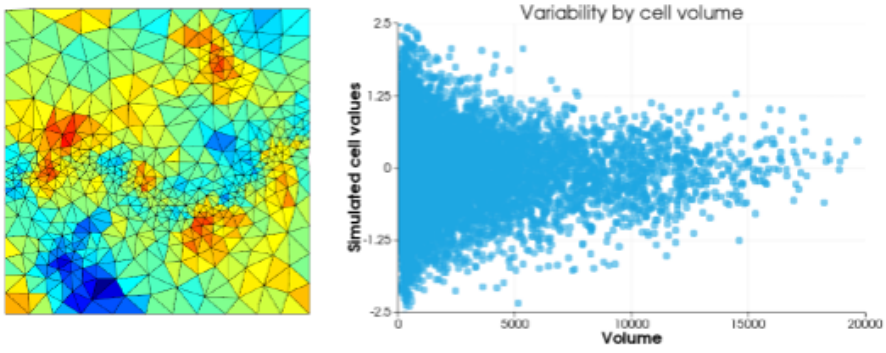

Figure 2.6: Simulated values on a tetrahedral unstructured grid, using the fine scale simulation and upscaling approach. The variability in simulated values decreases as the volume of the cell increases: it is the support effect. Taken from Gross and Boucher (2015).

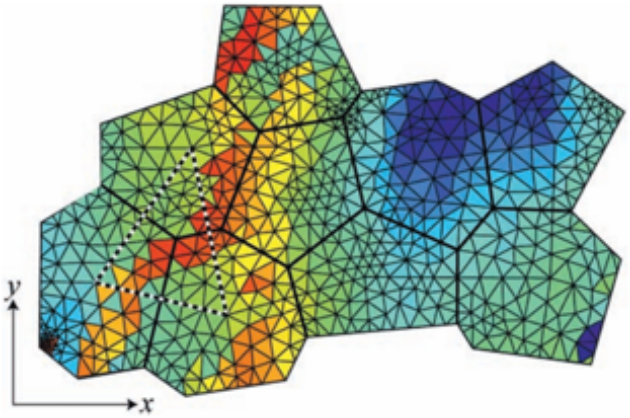

Figure 2.7: Example of triangular fine grid colored by permeability with an arbitrary scale. An interaction zone between three coarse cells is highlighted with a dashed line. Taken from Manchuk et al. (2012).

Another possibility is to replace the numerical upscaling of permeability by an analytical approximation allowing to go faster. Deutsch et al. (2002) suggests using power averaging. Others apply an approximate upscaling using, for instance, an averaging of Cardwell and Parsons bounds or a fast renormalization as presented in Renard et al. (2000).

The approach using a fine grid is simple and the geostatistical parameters are kept at the point support scale: point conditioning data, with the associated histogram and covariance model. However, it is computationally expensive because a potentially large fine grid is made and stored and, in cases where numerical upscaling is chosen, it is time consuming (e.g., Zaytsev et al., 2015). It is even more time consuming for multi-realizations of petrophysical variables such as permeability, often performed in the industry, where the numerical upscaling has to be performed several times.

2.2.2 Use of a point-support

Another approach allowing to avoid the storage of a fine grid is presented in Gross and Boucher (2015) as an extension of the method of Boucher and Dimitrakopoulos (2009). In this method, blocks are sequentially simulated at point scale using LU decomposition before being upscaled (for details on LU decomposition see Davis (1987)). The simulation on points accounts for hard data and the blocks already sim-

ulated. This approach still uses a discretization of the cells, but there is no need for the generation of a fine grid. Moreover, only the block values are kept, i.e. points are deleted, allowing a low memory cost.

Biver et al. (2019) develops a method based on this approach: each cell is filled with points and a value is evaluated at the points using Spectral Turning Bands as implemented in Emery and Arroyo (2017). Turning bands were introduced in Matheron (1973) and further developed by many authors including Mantoglou and Wilson (1982), Tompson et al. (1989), Lantuéjoul (2002) and Emery and Lantuéjoul (2006). The general principle of this technique is to reduce a D dimensions simulation problem to a one-dimensional simulation. The first step is to generate L lines θ_i such that their orientation is uniformly distributed over the unit sphere. A 1D simulation is made along each line using the one-dimensional field covariance C_{θ_i} resulting from the D-dimensional covariance C. Numerous methods for simulating a one-dimensional random field knowing its covariance C_{θ_i} are found in the literature. They can be classified into continuous spectral simulation using cosine functions (Mantoglou and Wilson, 1982; Shinozuka and Jan, 1972); discrete spectral simulation using Fast Fourier Transform (Tompson et al., 1989); and circulant embedding (Dietrich, 1995). From these simulated lines, the simulated value at any point can be obtained by projection and summation. For additive variables, a simple arithmetic average allows to obtain values on the blocks, an example is given for porosity (Fig. 2.8).

2.2.3 Direct simulation using block covariances

The last type of approach is the direct population of the unstructured cells using block covariances. The existing methods are based on the analytical or numerical estimation of the covariance between data points and cells of different support and geometries.

Among them, one method is to use the Direct Sequential Simulation or DSS, that needs no transformation of the original variable (e.g., Deutsch et al., 2002). DSS is based on two mathematical tools: the sequential simulation available in Goovaerts (1997) and the simple kriging principle of Journel (1994). The sequential simulation principle makes it possible to simulate a multivariate random vector in a sequential manner, assuming all conditional distributions of a variable given all previously simulated variables are known. The simple kriging principle states that the sequential simulation reproduces the target covariance model if the mean and variance of the conditional distribution at each algorithm iterations are determined by simple kriging. It ensures a correct

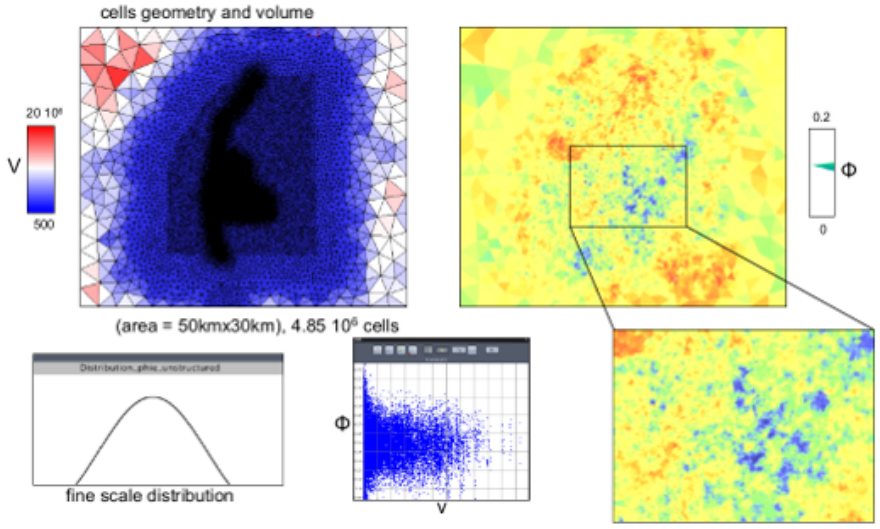

Figure 2.8: Results of porosity simulation process on a real field unstructured grid. Taken from Biver et al. (2019).

reproduction of the block-to-block covariances. Two DSS algorithms are considered for extension on unstructured grids in Zaytsev (2016): DSS 1 (Soares, 2001) and DSS-HR (Oz et al., 2003). Since DSS 1 does not respect the simple kriging principle, and thus may not reproduce correctly block-to-block covariances, only DSS-HR is deemed applicable to unstructured grids. The algorithm is an implementation by Oz et al. (2003) of Deutsch et al. (2000) proposition, that has been extended in Tran et al. (2001). Application of DSS-HR to simulations on unstructured grids was proposed in Manchuk et al. (2005). The key idea is to use a table of conditional distributions that allows accounting for plenty of possible shapes for the final block values histogram. In this table, the distributions are indexed by their mean and variance values. A location u is chosen randomly in the grid, and the mean and variance of the local distribution at u is obtained by simple kriging using all input data and previously simulated values. The closest conditional distribution in terms of mean and variance is retrieved from the table. A simulated value is then drawn from the conditional distribution chosen, by Monte Carlo simulation. Once all values on points are simulated, the results are transferred from point to block support: the mean value of one block is obtained through the mean of the point-support random field and the variance through the point-support covariance.

In general, DSS guarantees that the spatial covariance of the variable of interest is reproduced, but the univariate histogram is not controlled unless applying a post processing (e.g., Journel and Xu, 1994). The advantage of DSS-HR, compared to classical DSS, is that it ensures the reproduction of the global histogram. Moreover, DSS algorithms can be parallelized to reduce computation times (Nunes and Almeida, 2010).

However, Zaytsev (2016) highlights some theoretical drawbacks of this method:

1. The Direct Sequential Simulation, like all sequential simulation algorithms, uses a limited neighborhood for the simulation. This local neighborhood implies an underestimation of the theoretical covariance between blocks. This effect of local neighborhood on model statistics has been demonstrated in Emery (2004).

2. The Central Limit Theorem states that the normalized sum of independent random variables tends toward a normal distribution, even if the variables are not normally distributed. Zaytsev (2016) has tested the DSS-HR methodology to see if the marginal distribution obtained for a selected block, here a large block offering a strong reduction in variance, converges to a normal distribution. On this test, with a non-smooth CDF function at point-support (Fig. 2.9a), the marginal distribution at block support does not tend toward the normal (Fig. 2.9b). This problem is less visible for smooth CDF functions at point support. All in all, this test shows that the applicability of DSS-HR has to be tested for every possible shapes of CDF and every block sizes: DSS-HR seems difficult to use in general context for unstructured grids.

Another possible method is the Discrete Gaussian Model or DGM (Matheron, 1976), that has been investigated and implemented by Emery and Ortiz (2011) and Zaytsev et al. (2015). The aim is to simulate a variable Z, by working on its Gaussian transformation Y, knowing Z point support distribution and covariance $C(x, x')$. The support effect on unstructured grids is represented by a change of support coefficient r_v specific to each unstructured grid block v. To identify the value r_v for each block v , Zaytsev (2016) computes each block variance using point-support covariance C. The block-to-block covariances for each couple of blocs (v_p, v_q) is then obtained through a sextuple integral. Finally, the simulation of the random field Z is performed with Sequential Gaussian Simulation (SGS), using varying variances and covariances previously calculated.

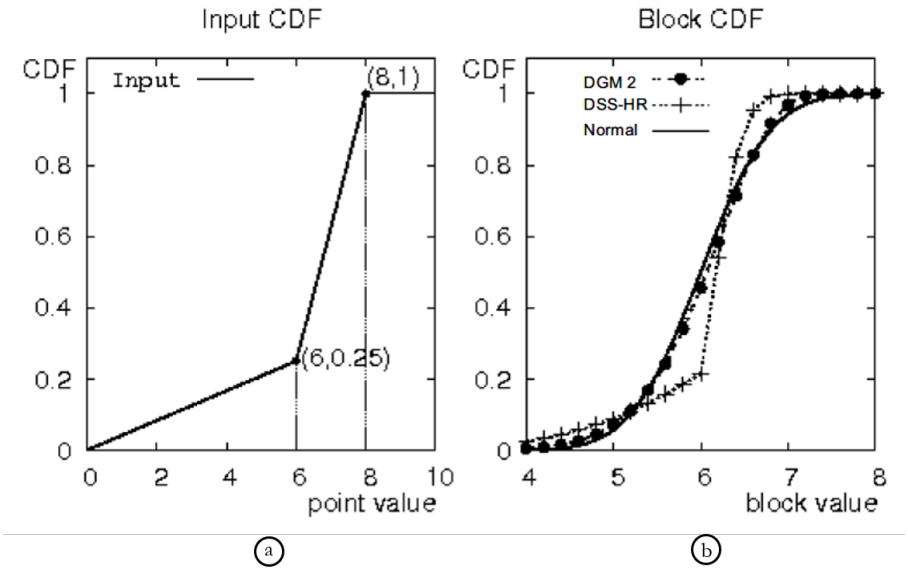

Figure 2.9: Marginal distribution at a) point support and b) selected block support for DSS-HR, DGM and Gaussian distribution. Taken from Zaytsev (2016).

An advantage of using the DGM on unstructured grids, compared to DSS, is that the true marginal distributions of the block values is well reproduced, independently from the size of the block. It has been demonstrated for small changes of support in Matheron (1985). Computationally speaking, the advantage of such a simulation is that the memory needed is reduced compared to the fine-scale simulation approach. However, it presents some drawbacks:

1. The calculation of block covariances, a sextuple integral, is really time consuming and needs to be efficient. A discussion on covariances computation is available in Zaytsev (2016). An idea is to discretize each block with a finite number of points N, and to take the arithmetic mean of the point-to-point covariances as the block-to-block covariance (Journel and Huijbregts, 1978; Goovaerts, 1997). Several discretization strategies have been studied by Zaytsev (2016): regular, Gaussian quadratures, pseudo-random points and Sobol' quasi-random sequences (Antonov and Saleev, 1979). Among them, the Sobol' quasi-random sequences discretization is the most efficient (Fig. 2.10). However, the computation times are still large: theoretically, considering a multi-

processor computer able to compute the matrix of block-to-block covariance in the same time t as one block-to-block covariance (which in practice is not necessarily the case), the covariance computations step only, for a grid with 10^6 cells, takes 16.5 minutes, a significant amount of time. In practice, it appeared that one porosity simulation on a grid of 5.10^6 cells took twenty hours.

2. DGM, in its final step, uses a Sequential Gaussian Simulation, which, just like DSS, implies a limited neighborhood. It has a negative effect on the reproduction of the input data, as soon as the number of neighbours chosen is too low. A simple solution to this problem is to replace the sequential algorithm by another method of Gaussian random vector simulation. An example given in Zaytsev (2016), is a Gibbs Sampler (Geman and Geman, 1984), as implemented by Lantuéjoul and Desassis (2012).

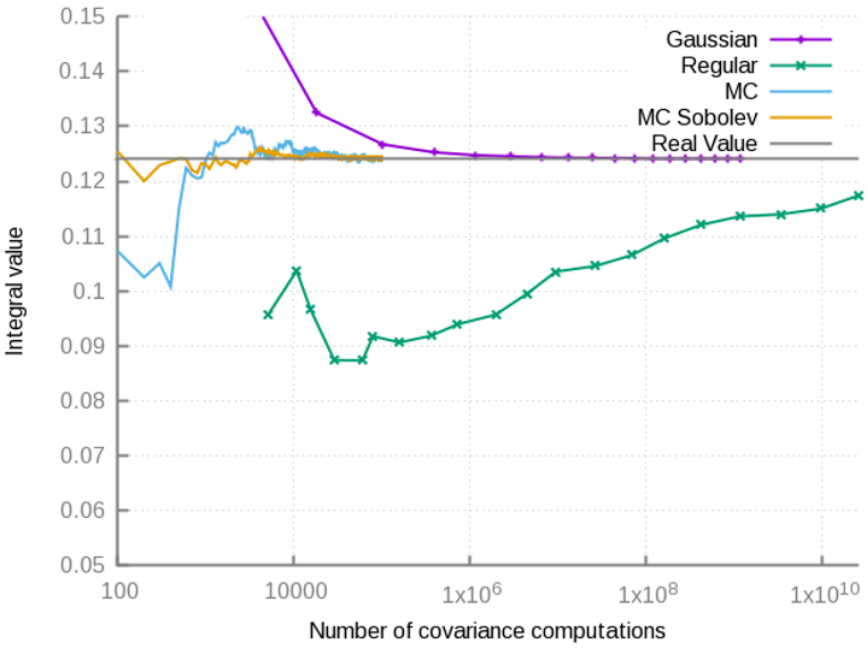

Figure 2.10: Comparison of the efficiency of four methods of discretization for the block-to-block covariances computation. The efficiency is represented by a number of point-to-point covariances computation needed, in abscissa. Taken from Zaytsev (2016).

For the two above-mentioned methodologies, the main problem is

that to simulate permeability, a non-additive variable, additional assumptions have to be made in order to transform permeability to a variable that averages linearly.

An idea for direct simulation of permeability at block support is presented in Tran (1996), based on the approach proposed by Gómez-Hernández (1991). Although it was only applied to structured grids, it offers a solution that could be applied to unstructured grids. The general idea is to approach numerically the covariances between points and blocks. To do so, several point calibration images are obtained through SGS, honoring the point-support statistics (Fig. 2.11a). A numerical upscaling is performed on these images, obtaining block calibration images (Fig. 2.11b). From the block calibration images, the spatial statistics at block-support are derived (Fig. 2.11c). The block statistics are entered into a simulated annealing program that performs the simulation at block support. Tran (1996) transfers point-support conditioning data to block-support by using a geometric average of the point-support data and a rank-preserving quantile transform (Fig. 2.11d). In the annealing simulation, the conditioning block data remain unchanged.

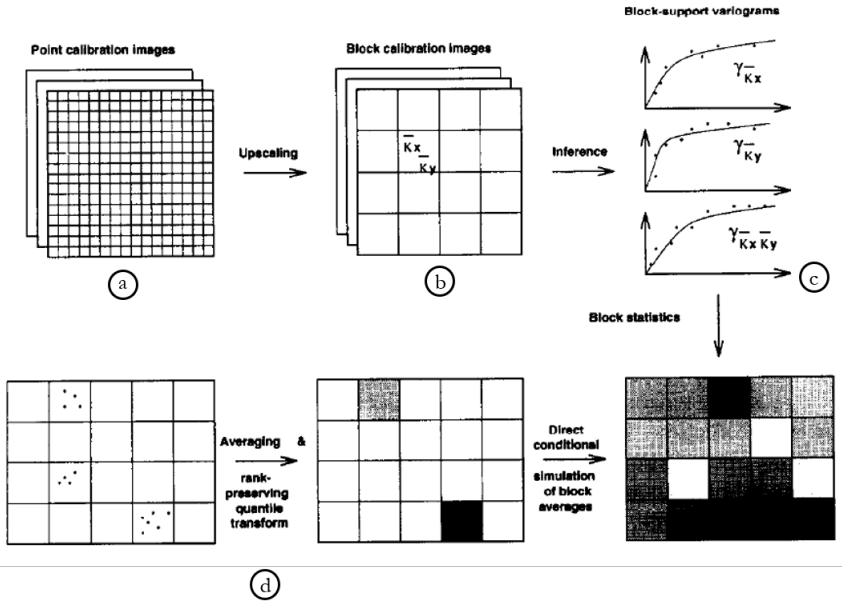

Figure 2.11: Direct simulation of block effective properties using numerical calibration and rank-preserving quantile transform for conditioning. Taken from Tran (1996).

2.2.4 Simulation of categorical variables

Discrete properties simulation on unstructured grids is also impacted by support effect. Indeed, assigning each block, independently from its size, a discrete variable leads to a loss of information. If the support effect is not respected, the input spatial statistics will not be reproduced and it can have an impact on future flow simulations. It is more rigorous to consider a vector of proportions of facies for each unstructured cell.

The simulation of facies proportions on unstructured grids implies more difficulties than the simulation of continuous properties. A reason for that, among others, is that all proportions in each cell must sum to one. So far, there are only a few existing approaches to simulate facies taking into account support effect. An idea is to generalize common algorithms such as Sequential Indicator Simulation (SIS), Truncated Gaussian Simulation (TGS) or Pluri-Gaussian Simulation (PGS) for unstructured grids. Such a generalization of PGS called PG-DGM is presented by Zaytsev (2016). However, the block-to-block covariance reproduction is approximated and the marginal distribution of facies i proportion is not reproduced if facies i is bounded on both sides by other facies in the truncation diagram (Fig. 2.12).

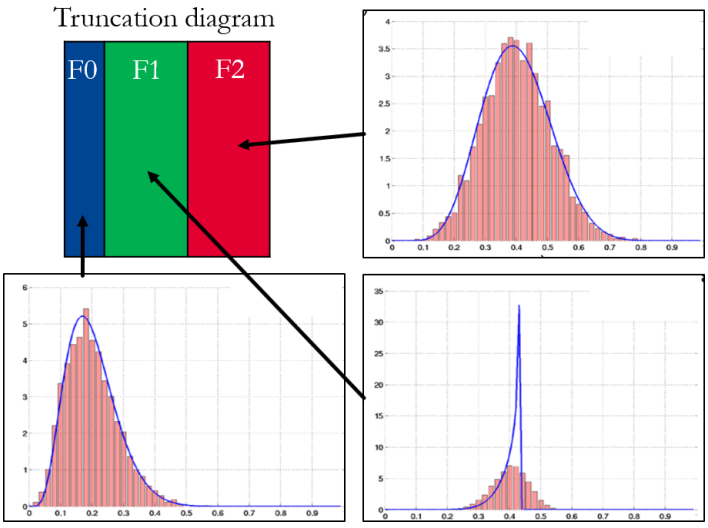

Figure 2.12: Truncation diagram with facies F1 bounded by F0 and F2. (Pink) The reference distribution obtained by Monte Carlo simulation. (Blue) The predicted distribution by PG-DGM. Modified from Zaytsev (2016).

An alternative solution is to proceed with a fine grid and an upscaling to the unstructured grid, just like the common solution for continuous properties. To avoid that, the solution presented in Gross and Boucher (2015) and described earlier is also applicable to facies proportions simulation. LU decomposition and truncated Gaussian formalism allow the computation of facies at point support. The proportions of facies in each block are then calculated by averaging point values (Fig. 2.13). The same approach, replacing LU decomposition by Spectral Turning Bands, is available in Biver et al. (2019) (Fig. 2.14).

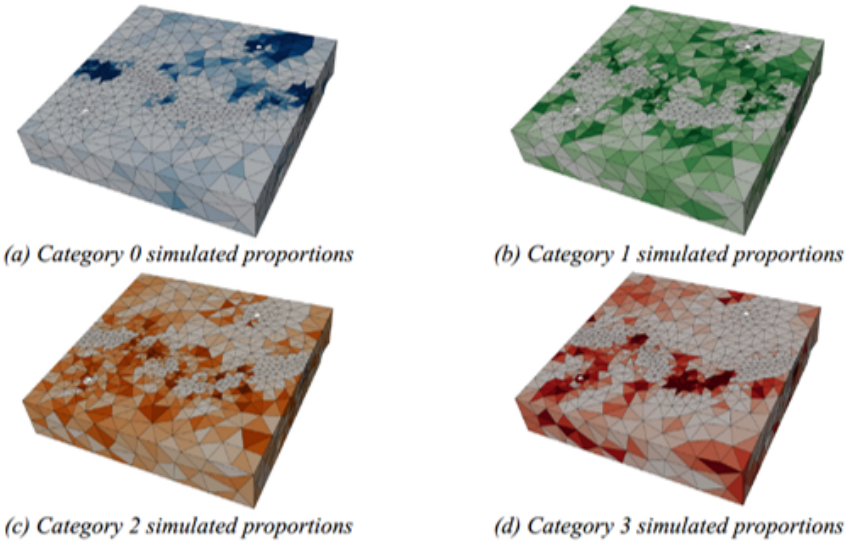

Figure 2.13: Truncated Gaussian Simulation on a tetrahedral unstructured grid. Four categories of facies are simulated, and the result is a map of proportion for each. Taken from Gross and Boucher (2015).

2.2.5 Limits of the existing methods

We presented above several methods for simulating continuous and categorical variables on unstructured grids, along with their advantages and limits.

The so-called fine-scale simulation approach is the simplest, and it allows a good reproduction of point-support statistics. Moreover, it is applicable to all types of variable: continuous, additive or not, and categorical. However, for permeability, it requires an upscaling step that can be expensive, especially for multi-realizations. Overall, it calls for

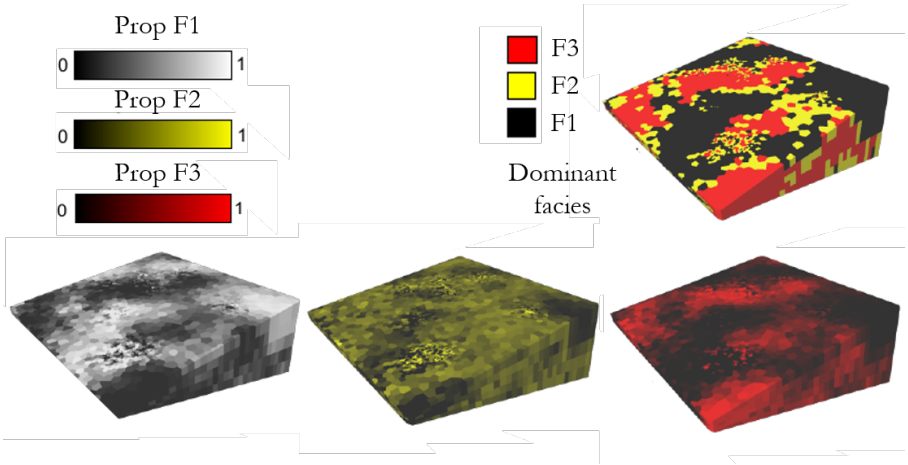

Figure 2.14: Simulated proportions of facies on a synthetic unstructured grid. Modified from Biver et al. (2019).

the making and storing of a large fine grid, implying a lot of computer resources.

The Direct Sequential Simulation of Oz et al. (2003) (DSS-HR) ensures a good reproduction of the point support statistics, and it can be fastened by parallelization. But, like all sequential simulations, it uses a local neighborhood that can lead to an underestimation of the theoretical covariance between blocks. Moreover, it is not always compatible with the Central Limit Theorem, especially when the input distribution is non-smooth.

The Discrete Gaussian Model extended to unstructured grids (Zaytsev et al., 2015) respects both point-support statistics and the Central Limit Theorem. It avoids the use of a potentially costly fine grid, but the calculation of block covariances through a sextuple integral is computationally difficult. For both DSS and DGM, one of the main problems is that the algorithms are applicable to additive variables only. Permeability would hence necessitate a transformation to make it additive. The application of the DGM formalism to PGS and facies simulations shows incorrect reproduction of the input statistics. Moreover, the last step of DGM algorithm uses the Sequential Gaussian Simulation, with the drawbacks of the local neighborhood. An idea for improving the reproduction of the theoretical covariance between blocks is to choose carefully the path to populate the grid with SGS (Nussbaumer et al., 2018). Otherwise, this problem can easily be solved by replacing the

sequential algorithm by another method to simulate Gaussian random vectors given a correlation matrix. A fast review of such methods is available in Emery and Lantuéjoul (2006). Zaytsev (2016) suggests the use of a Gibbs Sampler (Geman and Geman, 1984), as implemented by Lantuéjoul and Desassis (2012). This technique is based on Markov chains, where a number M of scans are performed, one scan being an iteration on all the components of the simulated Gaussian random vector. SGS could also be replaced by Spectral Turning Bands presented previously. The advantage of STB compared to other techniques of Gaussian random fields simulation is that it has the computational cost of a one-dimensional simulation. Moreover, the version presented in Emery and Lantuéjoul (2006) and extended in Emery and Arroyo (2017) allows an accurate reproduction of the desired covariance model, while SGS and continuous spectral methods offer an approximation.

The method proposed in this work is based on the approach of Gross and Boucher (2015) and Biver et al. (2019). The idea is to use an algorithm to simulate values on points and average these values on the blocks. In this work, we use Spectral Turning Bands (STB) as the tool for simulating variables on points independently from the grid. Simple arithmetic averaging will be used for additive properties and facies proportion simulation. The change of support for permeability, however, is not simple. A review on permeability upscaling is made in the following section and will be followed by the explanation of our simulation and upscaling technique.

2.3 Change-of-support for permeability

Petrophysical variables are strongly scale-dependent. For additive variables such as porosity, it is easy to change from core scale to block scale by using simple averaging. For non-additive variables, however, the change of support is not straightforward. One of the main non-additive variables controlling flow mechanisms is the absolute permeability. While using unstructured grids, permeability will be dependent on the different sizes and facies content of cells. Permeability upscaling is hence a major step for the direct geostatistical simulations of permeability on unstructured grids.

2.3.1 Problem statement

In this section, permeability will be considered at different scales. Absolute permeability is the property at the fine-scale, also called core-scale. The upscaled permeability, i.e. the permeability at block-scale, is called equivalent permeability. It covers two different notions: effective permeability and block permeability. Effective permeability is a property inherent to a large scale statistically homogeneous medium and thus is independent from boundary conditions (e.g., Matheron (1967b); Nœtinger (1994)). Block permeability represents the equivalent permeability of a defined, finite, block. It is usable for non-stationary permeability fields, with a value of block permeability varying from one grid cell to another. As a contrast to effective permeability, block permeability depends of boundary conditions and thus is not inherent to the medium only (e.g. Durlofsky (1992); Renard and de Marsily (1997)). In this section, we will use the word *permeability* to describe absolute permeability at fine scale and *equivalent permeability* to describe the permeability at block-scale.

The permeability k is a three-dimensional, strictly positive definite, symmetrical tensor (Matheron, 1967b):

$$k = \begin{pmatrix} k_{xx} & k_{xy} & k_{xz} \\ k_{xy} & k_{yy} & k_{yz} \\ k_{xz} & k_{yz} & k_{zz} \end{pmatrix} \tag{2.1}$$

For monophasic incompressible fluid flow in porous media, Darcy's law expresses the relation between the flux of the fluid and the driving forces (pressure gradient and gravity):

$$q = -\frac{k}{\mu}\left(\nabla p - \rho g\right) \tag{2.2}$$

with q the Darcy flux vector, k the rock's permeability tensor, μ the dynamic viscosity of the fluid, p the fluid pressure, ρ the density of the fluid and g the acceleration of gravity. For the heterogeneous media, the so-called "fine problem" in steady-state is described as follows:

$$\begin{cases} q = -\frac{k}{\mu}\left(\nabla p - \rho g\right) & \textit{Darcy's law} \\ \nabla \cdot q = 0 & \textit{mass balance equation} \end{cases} \tag{2.3}$$

The upscaling aims to find an equivalent permeability tensor $\widetilde{k}$ such that the coarse problem solution is the closest possible from the fine

scale solution.

$$\begin{cases} \widetilde{q} = -\frac{\widetilde{k}}{\mu}\left(\bigtriangledown \widetilde{p} - \rho g\right) & Darcy's\ law \\ \nabla \cdot \widetilde{q} = 0 & mass\ balance\ equation \end{cases} \tag{2.4}$$

To define $\widetilde{k}$, two main criteria are used to define the similarity between the fine and coarse problems:

- Identical flow: for the same head gradient, the total flow going through the domain should be equal for the heterogeneous and the homogeneous equivalent media (e.g. Warren and Price, 1960).
- Identical dissipated power: for the same boundary conditions, the energy dissipated by the viscous forces through the domain should be equal for the heterogeneous and homogeneous equivalent media (e.g. Indelman and Dagan, 1993; Matheron, 1967b; Le Loc'h, 1987).

Because of these different definitions and because the problem cannot be solved analytically in the general case, the computation of the equivalent permeability is not easy, except for some particular cases such as stratified media. Several methods have been proposed during the past decades, reviews can be found in Wen and Gomez-Hernandez (1996); Renard and de Marsily (1997); Farmer (2002); Sanchez-Vila et al. (2006); Dagan et al. (2013); Colecchio et al. (2020). The upscaling of permeability is a vast topic and we limit our study to monophasic fluid flow in porous media. Numerous studies can be found in other contexts such as fractured media (e.g. Bonnet et al., 2001; Bourbiaux et al., 2002; Painter and Cvetkovic, 2005; Weijermars and Khanal, 2019), two-phase fluid flow (e.g. Artus and Nœtinger, 2004; Eichel et al., 2005) or unsaturated fluid flow (e.g. Neuweiler and Vogel, 2007; Chen et al., 2020), but they will not be detailed here.

2.3.2 Bounds for equivalent permeability

Identifying the possible range of variation of the equivalent permeability has been a main topic of research for decades. The following part presents the principal known bounds.

Fundamental inequality

Several authors have proven that the equivalent permeability is always bounded by the arithmetic mean, as an upper limit, and the harmonic mean as a lower limit (e.g. Wiener (1912); Cardwell and Parsons

(1945); Matheron (1967b); Dagan (1986)). This fundamental inequality is expressed below:

$$\mu_H = H(k) \leq \widetilde{k} \leq A(k) = \mu_A \tag{2.5}$$

The arithmetic mean represents the equivalent permeability in the case of stratified layers or cells parallel to the flow. The flow will easily go through the highest permeability layer and thus the arithmetic mean corresponds to the highest possible permeability. The harmonic mean, on the other hand, corresponds to the case in which the layers are perpendicular to the flow, or, as an analogy to electricity, to cells in series perpendicular to the flow. In this situation the layer having the lower permeability will act as a barrier and thus the harmonic mean corresponds to the lowest possible permeability (Fig. 2.15).

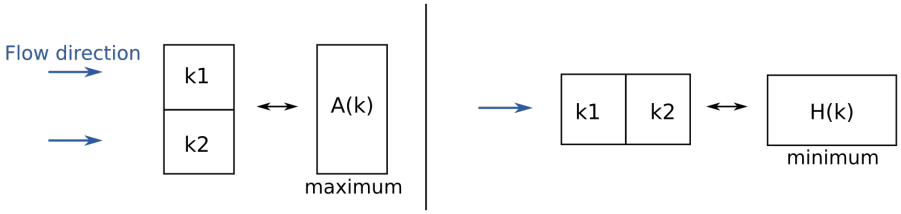

Figure 2.15: Local averaging of permeability for a group of two cells. A(k) is the arithmetic mean when cells are in parallel and H(k) is the harmonic mean when the cells are in series. Modified from Renard et al. (2000)

Cardwell and Parsons bounds

Starting from the fundamental inequality, Cardwell and Parsons (1945) defined tighter bounds for equivalent permeability in one direction:

- The lower limit is the arithmetic mean of the harmonic means of the fine cells permeabilities, taken by dividing the initial porous block into a set of thin cell rows parallel to the main flow (Fig. 2.16 top).
- The upper limit is the harmonic mean of the arithmetic means of the fine cells permeabilities, taken by dividing the initial block into thin slices perpendicular to the main flow (Fig. 2.16 bottom).

The inequality is written as follows:

$$\mu_H \leq \mu_A^z(\mu_A^y(\mu_H^x)) \leq \widetilde{k}_{xx} \leq \mu_H^x(\mu_A^y(\mu_A^z)) \leq \mu_A \tag{2.6}$$

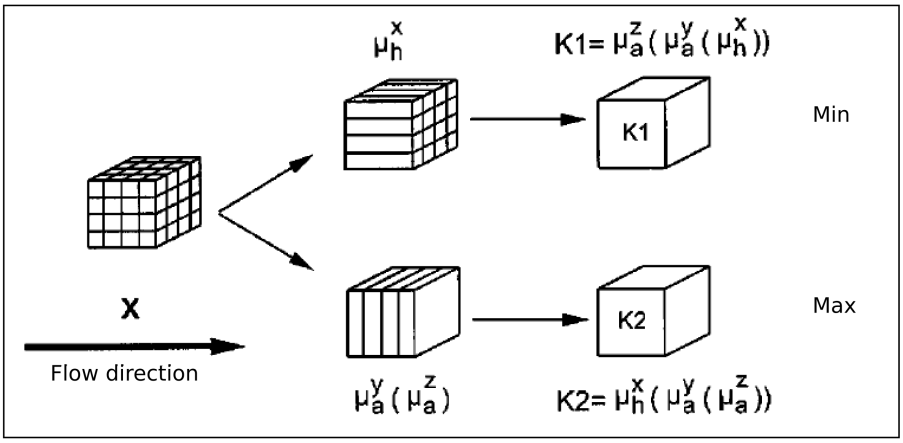

Figure 2.16: Calculating Cardwell and Parsons bounds, taken from (Renard, 1997). K1 is the arithmetic means of the harmonic means. K2 is the harmonic mean of the arithmetic means.

Specific equivalent permeability bounds

In the case of an isotropic binary medium, one can use the Hashin and Shtrikman bounds (Hashin and Shtrikman, 1962). The model considered is homogeneous at a large scale but heterogeneous at fine scale. It is a set of spheres composed of two isotropic components: the inside sphere of permeability K_{in} and a concentric shell of permeability K_{out} (see Renard and de Marsily (1997)). Let f_0 and f_1 be respectively the proportion of medium of permeability k_0 and the proportion of medium of permeability k_1. We consider $k_1 > k_0$ and D the space dimension. Then:

- If $K_{in} < K_{out}$, i.e. $K_{in} = k_0$ and $K_{out} = k_1$:

$$\widetilde{k} \leq \mu_A - \frac{f_1 f_0 (k_1 - k_0)^2}{(D - f_1)k_1 + f_1 k_0} \tag{2.7}$$

- Else if $K_{in} > K_{out}$, i.e. $K_{in} = k_1$ and $K_{out} = k_0$:

$$\widetilde{k} \geq \mu_A - \frac{f_1 f_0 (k_1 - k_0)^2}{(D - f_0)k_0 + f_0 k_1} \tag{2.8}$$

Hashin and Shtrikman bounds are considered as the tightest theoretical bounds for transport properties without information on the topology and distribution of phases (Brovelli and Cassiani, 2010). Renard and de Marsily (1997), however, have shown that there is no large difference between the fundamental bounds and Hashin and Shtrikman ones.

In two dimensions, for an isotropic random mosaic with two phases, Matheron (1993) defines tighter bounds for equivalent permeability. He obtains:

$$K_{ac} = ((f_0 - f_1)(k_1 - k_0) + \sqrt{(f_0 - f_1)^2(k_1 - k_0)^2 + 4k_0k_1})/2 \quad (2.9)$$

And demonstrates that:

- If $f_0 \leq 0.5$, $\widetilde{k} \geq K_{ac}$
- If $f_0 \geq 0.5$, $\widetilde{k} \leq K_{ac}$
- If $f_0 = f_1 = 0.5$, $\widetilde{k} = \sqrt{k_0k_1}$

2.3.3 Analytical methods to approach equivalent permeability

The aforementioned methods do not rely on the solving of flow equations, i.e. they are mostly based on theoretical bounds averaging. Several methods will be detailed in the following section.

Averaging fundamental bounds

Matheron (1967b) studies fundamental bounds averaging and concludes on the importance of the number N of space dimensions. In an isotropic statistically homogeneous medium, he suggests that permeability is at a half or two-third of the way between harmonic and arithmetic means, for N=2 or N=3, and translates it into the following formula:

$$\widetilde{k} = \frac{N-1}{N}\mu_A + \frac{1}{N}\mu_H \quad (2.10)$$

Averaging Cardwell and Parsons bounds

Le Loc'h (1989) suggests using the following formula as a primary fast estimator of equivalent permeability in two dimensions:

$$\widetilde{k} = \sqrt{K_1K_2} \; with \; K_1 = \mu_H^x(\mu_A^y) \; and \; K_2 = \mu_A^y(\mu_H^x) \quad (2.11)$$

Guerillot et al. (1990) used this formula for more general applications and compared results to experimental ones. Lemouzy (1991) extended this estimator to three dimensional cases:

$$\begin{array}{lcll} K_1 & = & \mu_H^x(\mu_A^y(\mu_A^z)) & = \mu_H^x(\mu_A^z(\mu_A^y)) \\ K_2 & = & \mu_A^y(\mu_A^z(\mu_H^x)) & = \mu_A^z(\mu_A^y(\mu_H^x)) \\ K_3 & = & \mu_A^y(\mu_H^x(\mu_A^z)) & \\ K_4 & = & \mu_A^z(\mu_H^x(\mu_A^y)) & \end{array} \quad and \; K_{eqv}^{xx} = \sqrt[6]{K_1^2 K_2^2 K_3 K_4} \tag{2.12}$$

Power averaging

Journel et al. (1986) proposed using power averaging formula to determine equivalent permeability in a binary medium. It can be used in 2D and 3D, and is expressed as follow:

$$\begin{array}{lcl} \widetilde{k}_\omega & = & (f_0(k_0)^\omega + f_1(k_1)^\omega)^{\frac{1}{\omega}} \quad for\ \omega \neq 0 \\ \widetilde{k}_\omega & = & (k_0)^{f_0} \cdot (k_1)^{f_1} \quad for\ \omega = 0 \end{array} \tag{2.13}$$

with f_0 and k_0 (respectively f_1 and k_1) the proportion and permeability of medium 0 (resp. 1). ω is the power averaging exponent.

A more general expression of the power averaging can be used for a medium with a continuous distribution of permeability (Journel et al., 1986; Desbarats, 1992; Ababou, 1996; Deutsch et al., 2002) to estimate the equivalent permeability $\widetilde{k}$ of a block:

$$\widetilde{k}_\omega = \left(\frac{1}{n} \sum_{i=1}^{n} k_i^\omega \right)^{\frac{1}{\omega}}, \tag{2.14}$$

with n representing the number of fine cells in a coarse block, k_i the permeability value in the cell i and ω the averaging exponent.

The exponent ω belongs to the interval $[-1, 1]$, $\omega = 1$ corresponds to the arithmetic mean, $\omega = -1$ corresponds to the harmonic mean and the limit of $\widetilde{k}_\omega$ when ω tends toward zero is the geometric mean.

$$\lim_{\omega \to 0} \widetilde{k}_\omega = \exp\left(\frac{1}{n} \sum_{i=1}^{n} \log(k_i) \right). \tag{2.15}$$

Several studies have given estimates of the value of ω for some specific distributions of permeability. In two dimensions, when the permeability k and its inverse ($h = 1/k$) have the same probability distributions, Matheron (1967a) proves that the equivalent permeability is the geometric mean if the statistics of the spatial distributions of k and h are

invariant by rotation, i.e. $\omega = 0$. A case that satisfies the previously mentioned conditions is a 2D isotropic medium with a log normal permeability distribution. In three dimensions, Nœtinger (1994) proposes an approximation for this specific case: $\omega = 1/3$. The validity of this formula up to the fourth order (small perturbation) has been demonstrated by Dagan (1993). However, de Wit (1995) and Abramovich and Indelman (1995) later showed using a sixth order development that in three dimensions it is not strictly valid and would necessitate a correction.

For anisotropic media, Desbarats (1992); Duquerroix et al. (1993); Kruel Romeu (1994); Ababou (1996); Nœtinger and Haas (1996) suggest a simple analytical form. Let $\lambda = L_H/L_V$ be the geometrical anisotropy depending on the ratio of the variogram ranges and $\kappa = k_V/k_H$ be the petrophysical anisotropy ratio. Changing variables in the Laplace Darcy equation allows to define a global anisotropy ratio through $\alpha = \sqrt{\kappa}/\lambda$. The proposed value of ω is (Fig. 2.17a):

$$\omega(\alpha) = \frac{arctan(\alpha)}{\pi - arctan(\alpha)} \tag{2.16}$$

Massonnat (2009) introduces ω_H for the horizontal permeability and ω_V for the vertical (Fig. 2.17b):

$$\omega_H(\alpha) = \frac{arctan(\alpha)}{\pi - arctan(\alpha)} \tag{2.17}$$

and

$$\omega_V = -2\ \omega_H + 1 \tag{2.18}$$

For isotropic random media, horizontal permeability is approximately equal to vertical permeability with $\omega = 1/3$ as discussed above. Massonnat (2009) introduces two additional coefficients ϵ_H and ϵ_V to account for the cell dimension for the global anisotropy ratio (Fig. 2.17c). These coefficients represent non ergodicity relative to horizontal and vertical directions.

$$\alpha = \frac{L_H}{L_V}\sqrt{\frac{k_V}{k_H}}\epsilon_H\epsilon_V \tag{2.19}$$

The parameter $\kappa = k_V/k_H$ can be estimated from core measurements, but it is not always done. A table of values has been proposed for turbiditic facies (Wigniolle and Massonnat, 2013). However, the main difficulty revolves around the dependency of ω to the coefficients ϵ_H and ϵ_V, that are hardly possible to estimate without empirical curves.

Liao et al. (2020) propose a new approach based on power average with an analytical determination of ω. However, this method is not sufficiently accurate compared to a numerical upscaling, unless it is applied to Gaussian random fields with moderate variance.

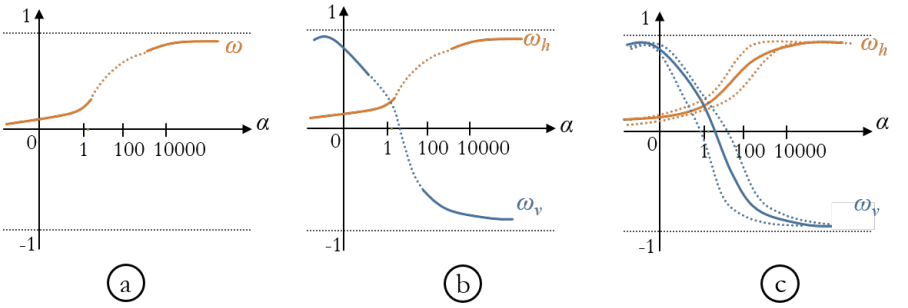

Figure 2.17: ω variations as shown in a) Nœtinger and Haas (1996), a single ω varying under α influence; b) Massonnat (2009), two different ω: one horizontal and one vertical; c) Massonnat (2009), taking into account cell sizes and an uncertainty linked to facies organization inside the cells.

Several authors used power averaging in specific contexts. Deutsch (1989) investigates 2D binary media made of a sand matrix and shale lenses using flow simulations. He observes that the power averaging model is efficient and proposes a simple equation to determine the averaging power ω as a function of the length of the shale inclusions. Also in binary media, Hosseini et al. (2008) conducted experiments in which an ω is fitted on an ensemble of numerically upscaled images, and power law is applied on a sand-shale medium in the form given in Equation 2.13. For intermediate porosity values, the permeability $\widetilde{k}_\omega$ appears too high. The reason for that is that the permeability of the sands k_1 depends of the fraction of shale f_0. They propose an extended power law formalism, that decreases the average sands permeability depending on the proportion of shales f_0:

$$log(\bar{k}_1(f_0)) = log(\bar{k}_{cs}) - \frac{f_0}{0.25}[log(\bar{k}_{cs}) - log(\bar{k}_1(0.25))] \tag{2.20}$$

where $\bar{k}_1(f_0)$ is the average reduced sand permeability for a given f_0, $\bar{k}_{cs}$ is the average clean sand permeability and $\bar{k}_1(0.25)$ is the reduced sand permeability at $f_0 = 0.25$ obtained by fitting to experimental data. The methodology is tested in comparison to a flow simulation and shows

good results. Still in binary media, Masihi et al. (2016) present new methods to estimate the equivalent permeability based on a weighted power averaging. They expressed the equivalent permeability using percolation theory, as dependent from geometric mean k_g and permeability threshold k_{th}:

$$\widetilde{k} = (f_0 k_{th}^m + f_1 k_g^m)^{\frac{1}{m}} \tag{2.21}$$

with the exponent m as the fractal dimension of the percolation minimal path. It gives reliable estimates for very heterogeneous models. Later, in a two phase flow context, Rabinovich et al. (2016) present a method for calculating effective relative permeability using both geometric mean and power averaging. In another context, Nasr et al. (2018) apply power averaging to upscale contaminant transport, choosing an ω value which minimizes the difference between the average velocity field in both a fine reference grid and the coarse target grid.

de Dreuzy et al. (2010) study the relevance of power averaging through a variety of 2D and 3D tests. They recall that power averaging is strictly valid for 2D cases only (e.g. Boschan and Nœtinger, 2012). For the 3D case, they conclude that, although not exact, power averaging gives a first approximation of upscaling at a few percents of precision.

The conclusion from this overview is that numerical experiments must be conducted to estimate ω, as there is no simple analytical solution. Further experiments have been performed to better understand the variations of ω. They are presented in the next chapter.

2.3.4 Numerical upscaling methods

We specified earlier that the equivalent permeability depends on the physical phenomena occurring in the reservoir at hand. For permeability upscaling, these phenomena are described using Darcy's law and mass balance equation. Numerical methods presented here, also called upscaling by pressure solver, rely on the resolution of the diffusivity equation:

$$\nabla \cdot \left[\frac{k}{\mu} \nabla (p - \rho g) \right] = 0 \tag{2.22}$$

We consider a block divided in several smaller cells. The fine-scale permeability field k is assumed known. The equivalent permeability is then calculated by solving the diffusivity equation using a pressure solver. To do so, one needs to define the boundary conditions. Different types of boundary conditions can be used:

Confined conditions

Two opposites sides of the block have constant head conditions (Fig. 2.18 left) and the others have "no-flow" conditions (sealed sides). Flow simulation is repeated applying boundary conditions in each direction. These experiments are often interpreted by computing only the total flux and the block permeability as a diagonal tensor. It is however simple to obtain the complete tensor from these experiments (Renard et al., 2001).

Unconfined conditions

All the sides of the block have prescribed and linearly varying pressure conditions (Fig. 2.18 right). It is roughly similar to the conditions of a block plunged in a homogeneous medium with uniform flow. By applying unconfined boundary conditions in each direction, one obtains all the terms of the permeability tensor.

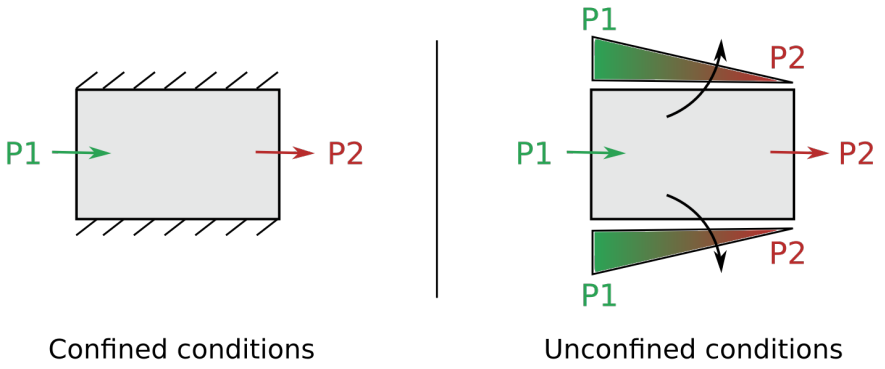

Figure 2.18: On the left, confined conditions with two sealed sides and imposed potentials P1 and P2. On the right, unconfined conditions, with no sealed sides, obtained by applying a potential P on each side. Modified from (Corre, 1991).

Boundary conditions can also be periodic with a constant head gradient for each set of two points on opposite cell sides. For more details, see the articles of Durlofsky (1991) or Boe (1994).

After defining the boundary conditions (Fig. 2.19a), we have to solve the partial differential equation (PDE) defined by the diffusivity equation. The aim is to obtain the value of the pressure p at each cell of the block, either at the center or at the corners of the cells, depending on the method chosen (Fig. 2.19b).

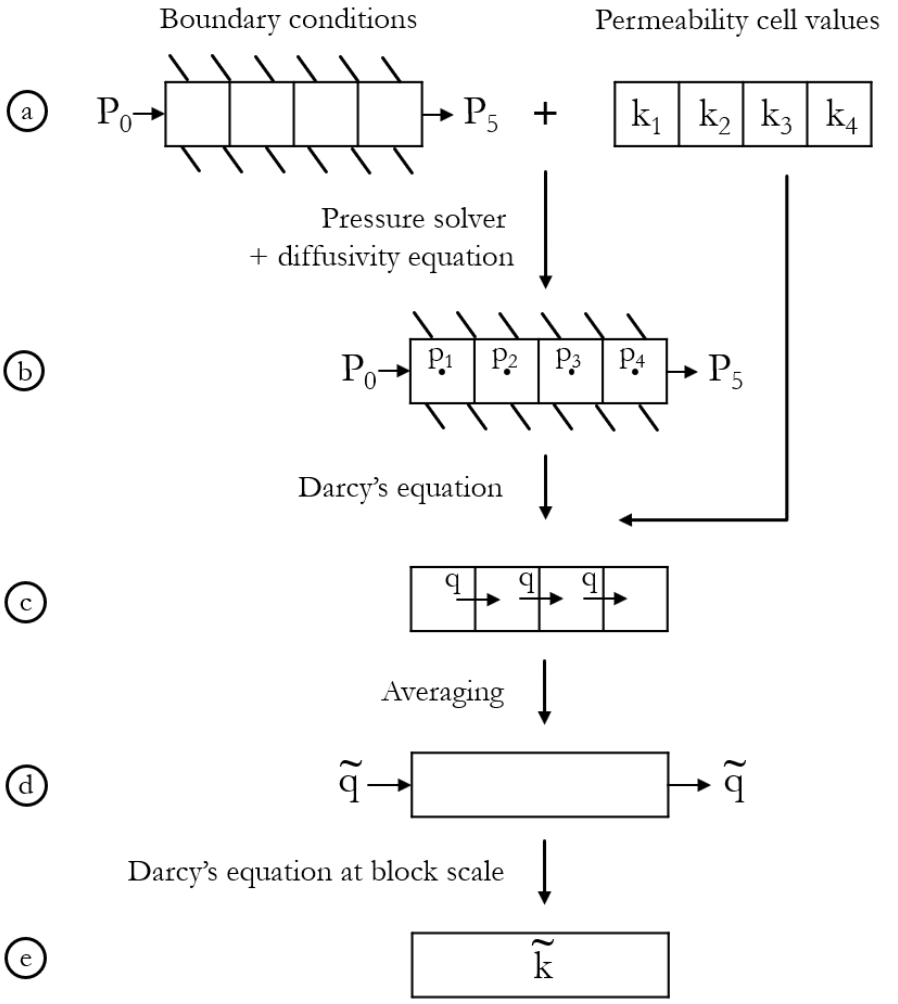

Figure 2.19: Numerical upscaling process. a) Boundary conditions and permeability at the fine scale are given as input. b) A pressure solver allows solving the diffusivity equation, obtaining a field of pressure. c) From this field of pressure and Darcy's law, Darcy's flows are computed. d) By averaging, we obtain the total flow on the block. e) Using darcy's law at block scale, the tensor of permeability $\widetilde{k}$ of the block is calculated.

The pressure field, together with transmissibility[1] values given to the upscaler as input, allow the calculation of the Darcy's flow q between

[1]In Eclipse Software manual, 'transmissibility' is the word used to describe inter-block conductivity (Schlumberger, 2014). However, in Eclipse files the word 'trans-

cells, through Darcy's equation (see Equation 2.2)(Fig. 2.19c). The total flow $\widetilde{q}$ through the block is then calculated from the local flows q (Fig. 2.19d). By applying Darcy's law at the scale of the block, the permeability tensor $\widetilde{k}$ of the block is found (Fig. 2.19e).

A difficulty is that, in general in 2D or 3D heterogeneous cases, and independently from the boundary conditions, there is no analytical solution to the PDE defined by the diffusivity equation, i.e. there is no direct and exact way to determine the field of pressure p over the domain. The solution is to use a numerical method to solve the differential equations. Three main approaches are used: finite differences, finite elements and finite volumes. All the numerical methods are based on some discrete approximations that depend on a discretization scheme. It is in general possible to refine the mesh and obtain highly accurate solutions but this implies a very high computational cost that is often not bearable for stochastic studies in which a very large number of flow problems have to be solved.

Finite-difference method

In this method, the value of the pressure p is calculated at the center of each cell discretizing the domain (e.g. de Marsily, 1986). Each cell can have a different permeability. The pressure is obtained by replacing the derivatives of the diffusivity equation by differences. For the cells presented in Figure 2.19, aligned along x axis and with centers separated by Δx, the partial derivative of $p(x)$ between the cells 2 and 3 is approximated by:

$$\frac{\partial p}{\partial x} \approx \frac{p_3 - p_2}{\Delta x} \tag{2.23}$$

and the second order partial derivative is approximated by:

$$\frac{\partial^2 p}{\partial x^2} \approx \frac{p_3 - 2p_2 + p_1}{\Delta x^2} \tag{2.24}$$

By applying these approximations in the diffusivity equation to every cell and every direction, one obtains a system of equations where the only unknowns are the pressures p_1, p_2, p_3 etc.

The advantages of such a method are its simplicity of formalism, easily applied to the code, and the low computation cost. However, it is limited to some simple geometries for the cells (square, rectangles)

missivity' is also used and should not be confused with hydro-geology transmissivity which is the permeability multiplied by the thickness of a cell.

and some boundary conditions are difficult to take into account (see de Marsily, 1986; Goncalvès da Silva, 2007).

Finite-elements method

In this method, the domain is paved with elements that can have more complex geometries, usually as segments, triangles or quadrangles (in 2D)(e.g. Pinder and Gray, 1977). The nodes or vertex are located at the edges of the elements, for example at the corners of a triangle. The unknown of the system are the pressure p_i at the nodes. The pressure distribution $p(x, y)$ over the whole domain is approximated by summing the nodal values and multiplying them by elementary base functions $b_i(x, y)$ such that:

$$p(x, y) = \sum_{i=1}^{m} p_i \; b_i(x, y) \tag{2.25}$$

The functions b_k can be chosen as polynomials of degree one, also called finite elements of degree one, or of degree two or more. The second step of the finite element method is to integrate the diffusivity equation over the domain to derive a set of expressions relating the discrete values of p_i for each node and taking into account all elements. These equations define a linear system where the unknown are the pressures at each node.

The advantages of this method are the high flexibility to represent complex geometries and a faster theoretical convergence of the results toward the real solution. The problem is that this method is slightly more complex to program (e.g., de Marsily, 1986; Goncalvès da Silva, 2007).

Finite-volumes method

In this method, the pressure is supposed constant in each cell and equal to a value close to the average over the cell (e.g. Goncalvès da Silva, 2007). Cell by cell, the PDE defined by the diffusivity equation is integrated. The mass conservation (the divergence of the flux) over the volume V is expressed by a surface integral:

$$\int_V \nabla \cdot q \; dV \approx \int_S q \cdot n \; dS \tag{2.26}$$

where the second integral represents the sum of the fluxes going through each face of the cell, with n_{face} the normal of the face going outward

and S the surface of the face:

$$\int_S q.n \; dS = \sum_{face} q_{face} \cdot n_{face} S \tag{2.27}$$

q_{face} is an approximation of the flux q through a face of the cell, and it is approached with a chosen numerical scheme. A well known numerical scheme is the Two Point Flux approximation, where the flow going through a cell's surface is equal to the head gradient through this face ∇h multiplied by the transmissibility value T. By expressing these balance equations for all the volumes, one obtains again a system of linear equations allowing to obtain all the pressures for every cell.

This method has the advantage of being applicable to complex geometries, with any shape of cells (provided that we use another numerical scheme than TPFA), and is better suited for different boundary conditions such as Neumann conditions, i.e. when the values of the derivatives is given at the boundary of the domain (e.g. Goncalvès da Silva, 2007).

All these pressure solvers, combined with Darcy's equation, allow calculating an approximate equivalent permeability $\widetilde{k}$ for any fine-scale permeability field k and any boundary conditions. They all present some advantages and drawbacks and must be chosen depending on impacting parameters, such as the type of mesh used to perform the upscaling. As a consequence, numerical upscaling methods present varying levels of accuracy, depending on the method chosen and level of discretization.

In addition, the results obtained with numerical upscaling techniques generally depend on the choice of the boundary conditions (e.g. Holden et al., 2000; Farmer, 2002). The local-global procedures, using a global coarse scale solution to define boundary conditions guiding the local upscaling, are among the more precise approaches (Durlofsky, 2005). Generally, numerical methods are more accurate than analytical methods (e.g. Christie et al., 2001). However, their dependence to boundary conditions as well as the computational cost they involve are to take into account when choosing an upscaling method.

Chapter 3

Preliminary studies on numerical upscalers and power averaging exponent

Before implementing our method, two problems needed to be investigated. First, a numerical upscaler had to be chosen as a reference to compute the equivalent permeability for the method presented after in this manuscript. Then, an experimental study needs to be performed to assess the variations of ω and the factors influencing these variations.

3.1 Choosing a numerical upscaler

To choose the reference upscaler, three numerical tools have been compared:

- **Zhou upscaler:** Zhou et al. (2010) published an open source code based on the finite difference method to solve the flow equation, assuming incompressible, single phase, steady-state groundwater flow. It allows the use of a 'skin' to reduce the impact of the boundary conditions, reproducing (for an infinitely large skin) the behavior of the whole reservoir or aquifer. This method computes automatically the transmissibility values used by finite difference codes to solve the flow equation (instead of the usual transmissibility calculation by averaging the neighbouring cells permeabilities). Zhou upscaler allows calculating a full tensor of equivalent permeability.

- **WakeUp upscaler:** This is Total's internal code working with a finite volume method for the solution of the flow equation (Jaquet et al., 2017). The flux approximation scheme is a Two Point Flux Approximation or TPFA, where the flow going through a cell surface is equal to the head gradient through this face multiplied by the transmissibility value. This value is obtained by averaging the permeabilities of the two cells sharing the target face either arithmetically, geometrically, or harmonically. The finite volume linear system is solved using a conjugate gradient solver.

- **Homog upscaler:** Total's previous internal code using homogenization theory (Samier, 1990). It allows obtaining a full equivalent permeability tensor. To determine its components, a pressure $P(x, y, z) = x$ is applied to the sides of the block discretized in several smaller cells. Using a finite elements method, the pseudo-pressure P_x is determined at every internal node of the block. From this, the component $\widetilde{K}_{xx}$ is obtained. By repeating these steps several times, for $P = y$ and $P = z$, every component of the full tensor is calculated.

The benchmark started by comparing the upscalers with a known analytical solution. The equivalent permeability of a 2D medium with a log-normal distribution of permeability, having small and isotropic correlation lengths as compared to the size of the domain is the geometric mean (Warren and Price, 1960; Matheron, 1967a). Numerical upscaling techniques must therefore give this result. A fine grid is taken into account, with 500x500x1 cells measuring 2x2x2 meters. The permeability distribution is a log-normal of mean 100mD and standard deviation 200mD. An exponential variogram with a single structure of ranges 800x800x1m is chosen. The coarse grid has 10x10x1 cells of 100x100x1m, which implies an upscaling ratio of 50x50x1. As shown on Figure 3.1, it is the case for all upscalers, with a small offset due to the method chosen for the calculation of equivalent transmissibility: the harmonic mean will give values slightly underestimated while the geometric mean will give an overestimation. WakeUp is computationally much faster than the two others.

The next experiments aim mainly at testing that WakeUp gives consistent results, as its CPU time is clearly much better than the two others. The tests are performed on a fine structured grid of 300x300x30 cells of 10x10x1 meters. A multi-Gaussian permeability field is simulated on this grid using SGS with a Gaussian distribution of mean

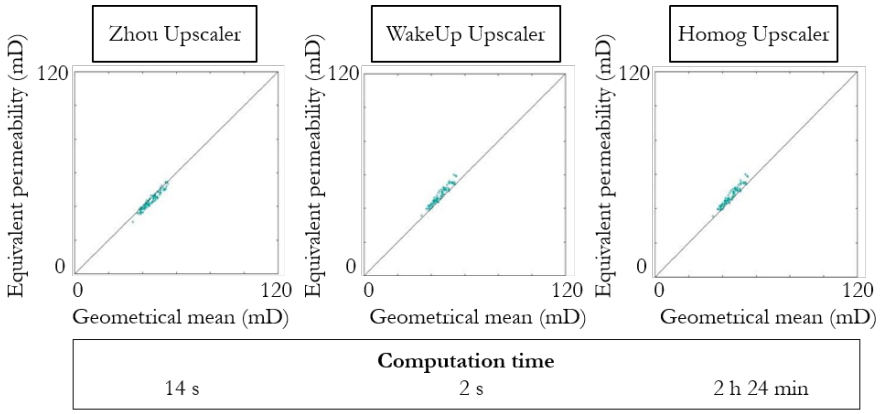

Figure 3.1: Comparison between upscaled permeability and geometrical mean for different upscalers. On this case, the exact solution is the geometrical mean.

100mD and standard deviation 1300mD. The variogram has a single exponential structure of ranges 800x800x1m. The boundary conditions for the upscaler are taken unconfined, and the equivalent transmissibilities are calculated with an harmonic mean. Several upscaling of this permeability field are performed, by varying the dimension of the upscaled blocks in the horizontal direction from 50 to 500 meters and keeping the vertical dimension equal to 6 meters. As presented on Figure 3.2, the results for horizontal permeability given by each upscalers are rather similar, even though the results obtained with WakeUp are closer from those obtained with Homog than those obtained with Zhou upscalers. For vertical permeability, WakeUp overestimates the equivalent permeability as compared to Zhou (Fig. 3.3). This overestimation is larger when comparing to Homog. In terms of computation times, for the smallest upscaling ratio (horizontal cell size of 50m), WakeUp takes 46 seconds, whereas Zhou takes almost 7 minutes and Homog 1 hour and 38 minutes. Based on this comparison only, it is not possible to conclude whether WakeUp gives the most reliable results or not. Therefore, other situations were analyzed: a case with SIS facies simulation, varying the proportion of shale, and a case with object based facies simulation, varying the proportion of channels, i.e. proportion of sand. When more heterogeneity is added, the correlation between equivalent permeabilities decreases. However, the same tendencies are kept: for the horizontal permeability, WakeUp is more correlated to Homog, and for the vertical permeability, WakeUp is more correlated to Zhou's upscaler.

A further analysis, including simulations at the scale of the reservoir, could be performed to pursue this analysis. However, the decision was taken to select the WakeUp upscaler because, in addition of being the most efficient computationally speaking, it provides results that are in general close to one or the other upscaler. The choice of the type of boundary conditions is another open question that will be discussed in this PhD.

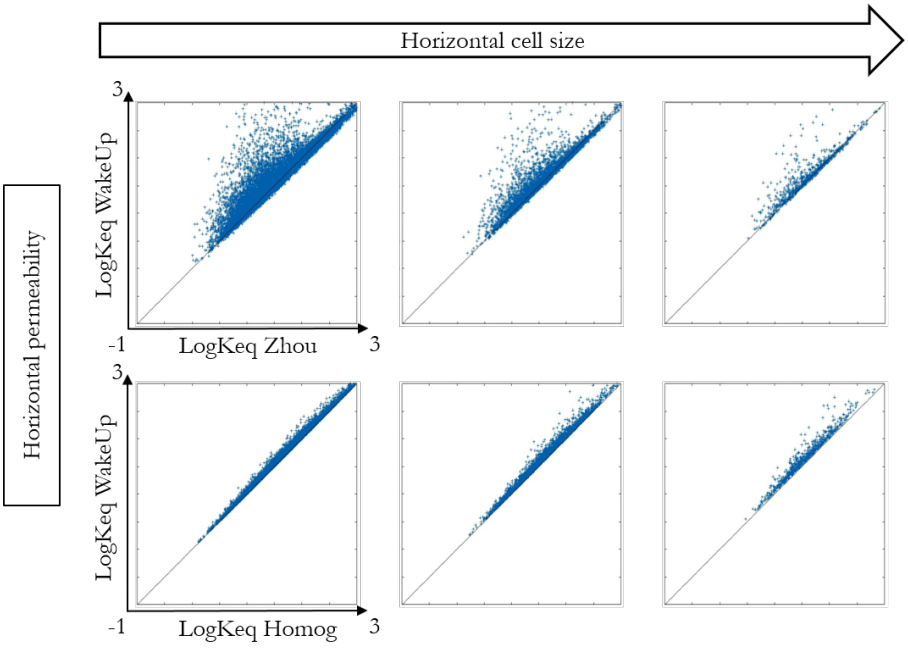

Figure 3.2: Comparison between upscaled horizontal permeability obtained with WakeUp and the ones obtained with Zhou upscaler and Homog. The upscaled blocks have sizes, from left to right, of 50x50x6m, 100x100x6m and 250x250x6m.

3.2 Studying the exponent omega variations

In this work, a new algorithm is proposed to directly simulate permeability on unstructured grids and avoid the use of a fine grid. The method is based on the transform of permeability into an additive property using power averaging (see Section 2.3.3), as suggested by Deutsch

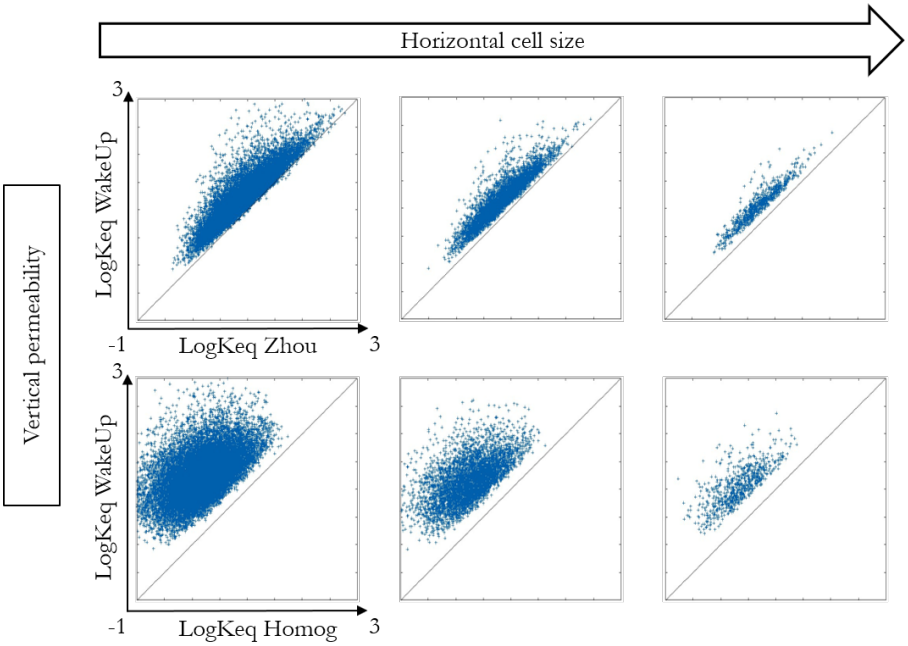

Figure 3.3: Comparison between upscaled vertical permeability obtained with WakeUp and the ones obtained with Zhou upscaler and Homog. The upscaled blocks have sizes, from left to right, of 50x50x6m, 100x100x6m and 250x250x6m.

et al. (2002):

$$K_\omega = \left(\frac{1}{n} \sum_{i=1}^{n} k_i^\omega \right)^{\frac{1}{\omega}} \tag{3.1}$$

with n the number of points or fine cells in a block, k_i the permeability at point i and ω the averaging exponent.

This section presents a preliminary study of the factors influencing the variations of ω. The idea is to know from which factors ω depends, so that our calculation of ω can take them into account. It also acts as a reference for our results, to see if the variations are respected through our method. Nœtinger and Haas (1996) have shown that ω depends on the variogram ranges, and Massonnat (2009) adds two factors: the cell sizes and the facies organization inside those cells. Our experiments aim to determine how ω is influenced by these three factors.

3.2.1 Impact of cell sizes versus variogram ranges

The experiments are performed on a fine structured grid of 300x300x30 cells measuring 10x10x1 meters. Multi-Gaussian permeability fields are simulated on this grid using SGS with a Gaussian distribution of mean 10mD and standard deviation 13mD, and varying exponential variogram ranges: 100x100x1m, 100x100x8m, 800x800x1m and 800x800x8m. Figure 3.4a shows the permeability field on the fine grid for variogram ranges of 800x800x1m.

To assess the influence of the cell size on ω variations, the initial grid is divided in blocks having different horizontal sizes D_H and the same vertical sizes: 50x50x6m, 100x100x6m, 250x250x6m and 500x500x6m. For each block, the reference horizontal and vertical permeabilities are computed with the numerical upscaler and denoted K_{refH} and K_{refV} (see Figure 3.4b for horizontal reference). Then, for each upscaled block b, one ω_H horizontal and one ω_V vertical are determined such as $K^b_{ref} - K^b_\omega = 0$, K_ω being calculated by using the power averaging formula. By doing so, we obtain a distribution of ω_H and one of ω_V for each cell size (see Figure 3.4c for ω_H distributions).

The average of these distributions is calculated, giving an averaged ω for each cell size. The plots on Figure 3.5 show the variation of averaged ω values depending on the cell size and the variogram ranges used for permeability simulation.

On this case, the influence of the horizontal cell size on ω_H is limited: the values of ω remains almost constant. However, it is not the case with all the experiments performed. For ω_V, the cell size influence is marked by a variation of ω of 0.3 for the most laminated case. It appears that the effect of cell sizes on the variations of ω_V is stronger when the cell sizes are small compared to the variogram range. Moreover, in a strongly laminated infinite medium, all ω_H should be equal to 1 and ω_V to -1. This tendency is respected with the more laminated (but not infinite) case plotted in blue, which gives a hint of the robustness of the results. The same protocol has been applied with a variation of vertical cell sizes, obtaining similar results.

3.2.2 Impact of shale proportion

For the facies proportion, a similar methodology was applied. SIS was first used to simulate the facies with different prior shale proportions (0%, 20%, 40%, 60%, 80% and 100%). MultiGaussian fields obtained with SGS using the parameters shown in Figure 3.6a are then used to

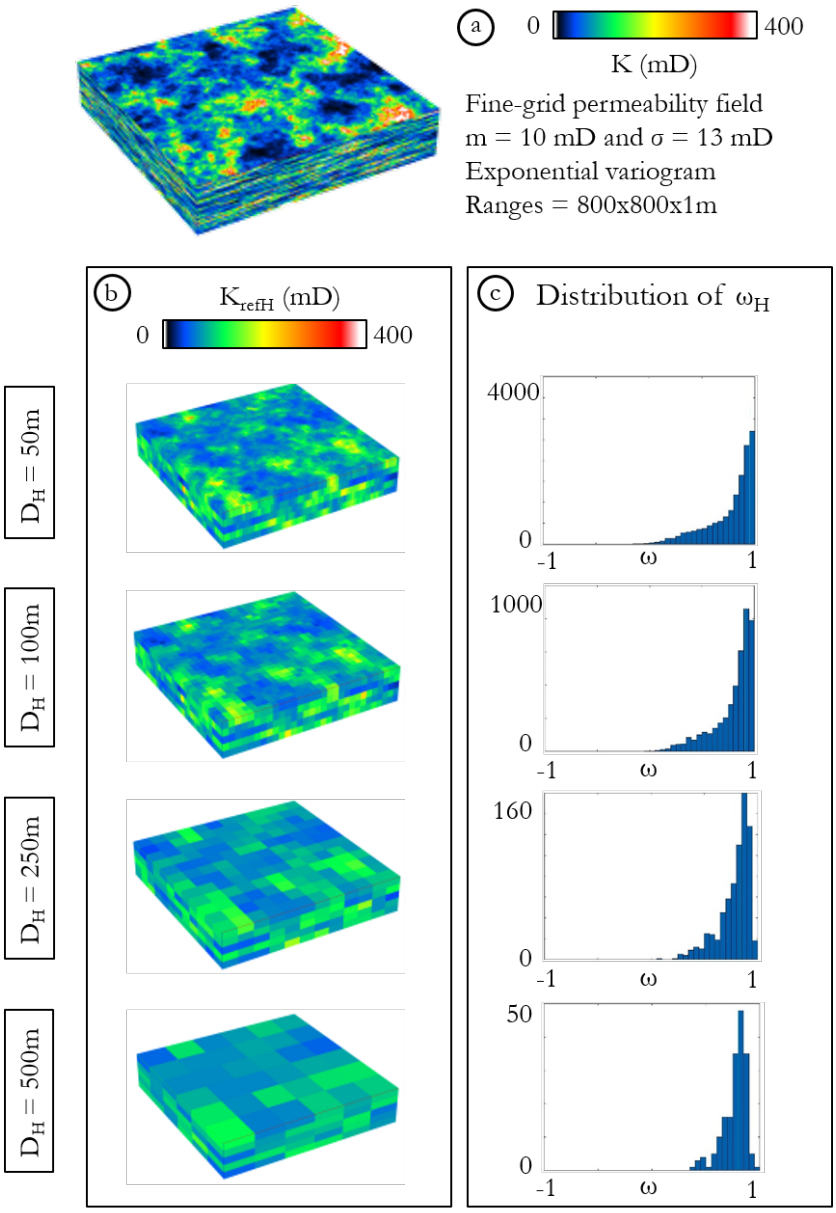

Figure 3.4: Influence of the horizontal cell size on ω_H variations. a) Permeability field simulated on the finegrid for the variogram ranges of 800x800x1m; b) Reference horizontal permeability K_{refH} obtained with a pressure solver upscaling; c) Distributions of ω_H obtained by fitting K_ω on K_{ref} for each upscaled block.

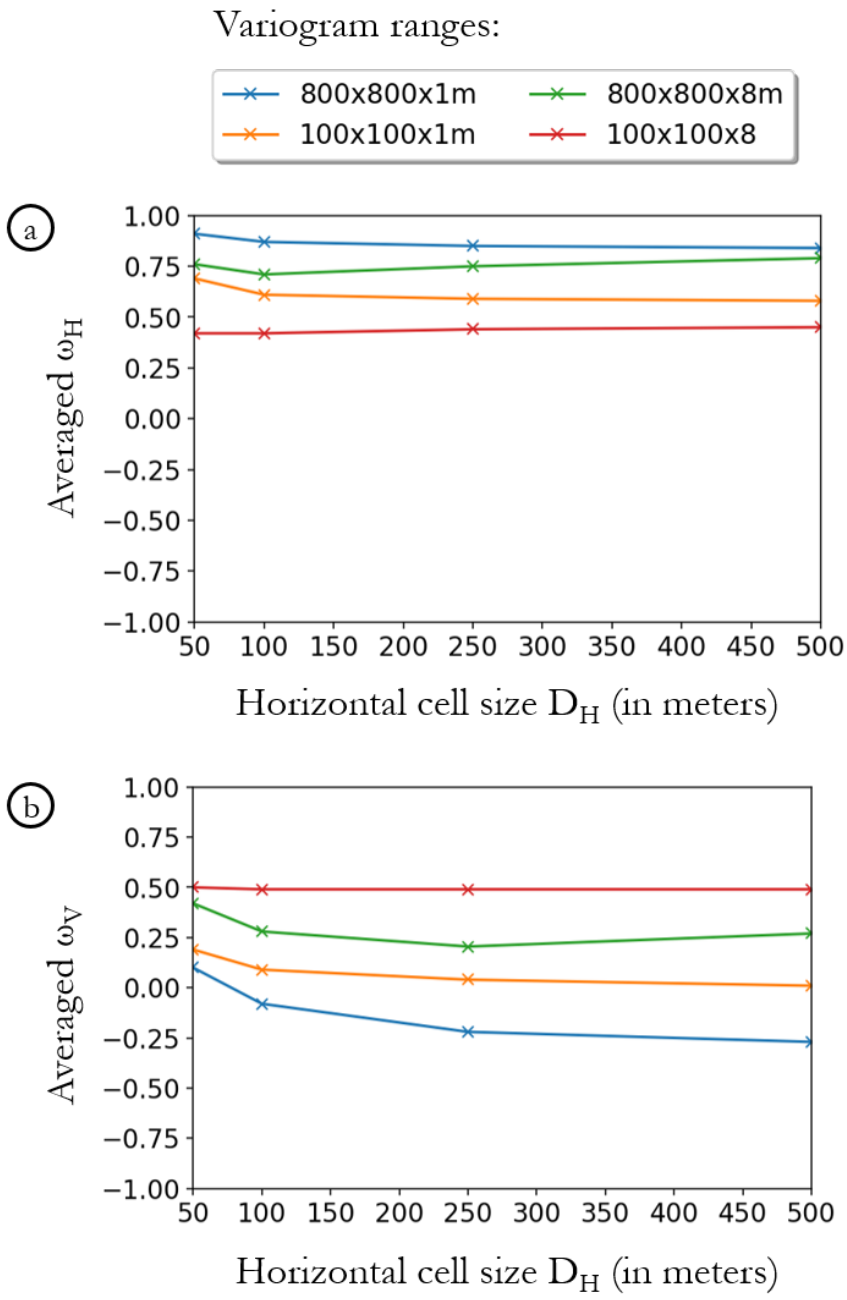

Figure 3.5: Variation of a) ω_H and b) ω_V depending on the horizontal cell size D_H and the variogram ranges.

populate the facies with permeability values. The same upscaling procedure and identification of ω is performed (Figure 3.6b). The statistical distributions of ω_H are shown in Figure 3.6c.

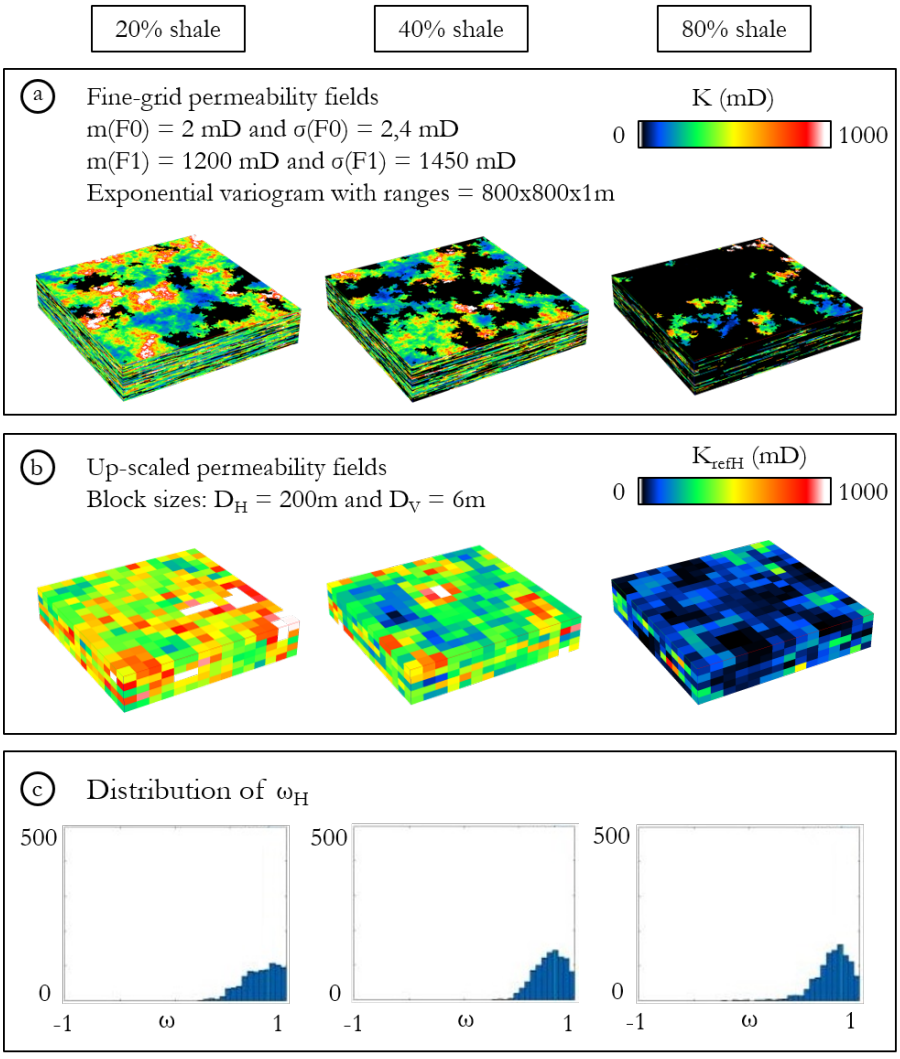

Figure 3.6: Influence of the prior proportion of shale on ω_H variations. a) Permeability field simulated on the fine grid for different shale proportions and the variogram ranges of 800x800x1m; b) Reference horizontal permeability K_{refH} obtained with a pressure solver upscaling; c) Distributions of ω_H obtained by fitting K_ω on K_{ref} for each upscaled block.

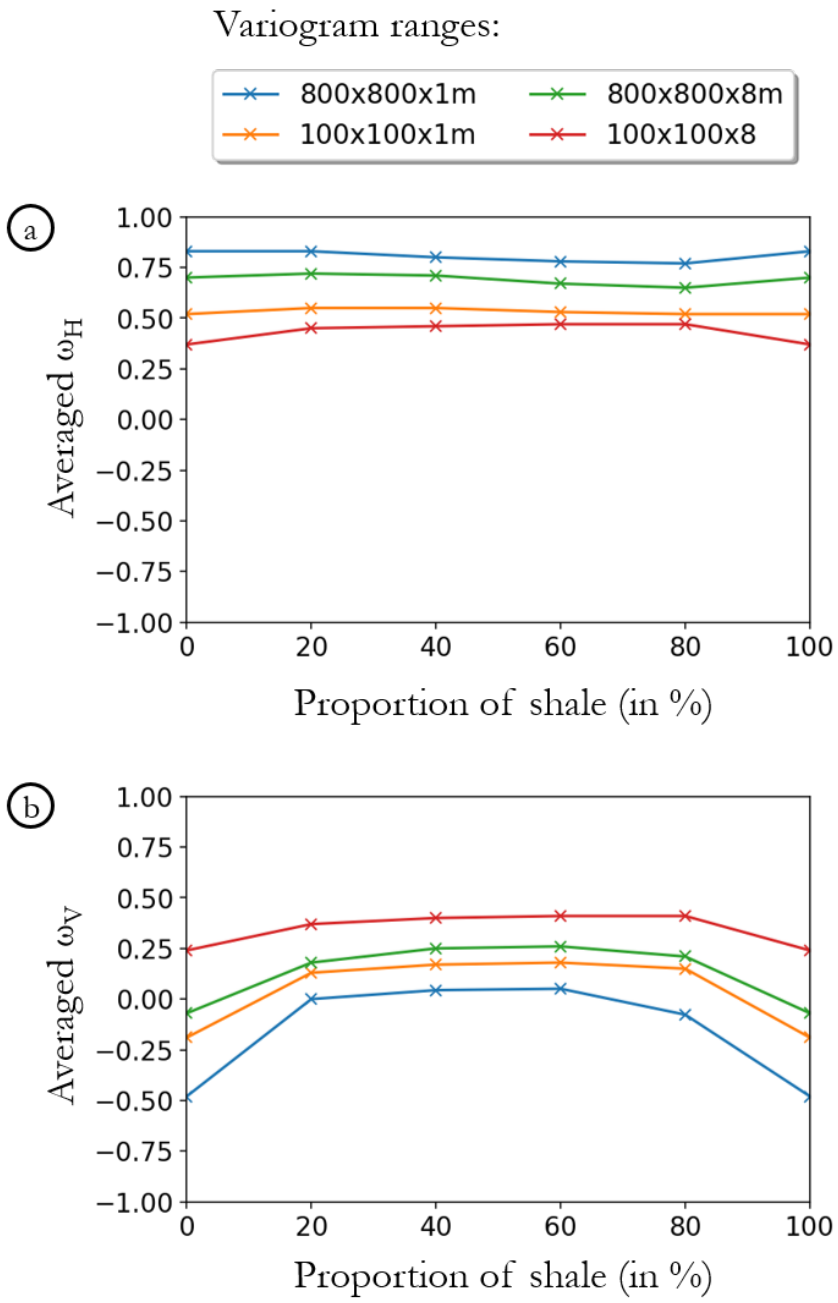

Figure 3.7: Variation of a) ω_H and b) ω_V depending on the prior proportion of shale inside the cells and the variogram ranges.

As for the cell size variations, ω_H is merely affected by proportion variations, on the contrary of ω_V (Fig. 3.7). A variation of 0.5 in ω_V values can be seen on the most laminated case. ω are mostly affected by small and high values of shale proportion: between 0 and 20 percent and 80 and 100 percent. This result appears consistent with percolation theories, that show there is a critical proportion, i.e. a threshold, for which the behavior in the media will change drastically. The value of ω is the same for the medium composed of 100% shale and 100% sand. From this value at 0% of shale, the ω increases, until the proportion threshold of 20% of shale is reached. There, the ω stays the same, until the proportion threshold of 20% of sand is reached and it starts decreasing again.

3.2.3 An approximation for ω

An approximation on omega's determination has been tested in order to see if the uncertainty on ω linked to facies organization inside the blocks (Massonnat, 2009) can be neglected.

Independently from the type of permeability distribution or any parameter related to the experiments, a value ω can be found for any block b of equivalent permeability K^b_{ref}, such as $K^b_{ref} - K^b_{\omega} = 0$, i.e. there is always a value ω such as the power averaging formula is equal to the equivalent permeability given by the upscaler. It means that for one block size there are as many ω possible as there are blocks in the upscaled grid, i.e. one size of block is characterized by a distribution of values of ω.

This would not be practical for our objective which is to find one single value of ω for each cell of the unstructured grid. The spatial distribution of ω is certainly not simple to infer and it would thus be complicated to simulate ω with uncertainties and respecting its spatial continuity.

To avoid this issue, the proposed idea is to assume that it is reasonable to use a unique ω for all the blocks having the same characteristics (sizes and proportions of facies). Before going further, this approximation is tested here by comparing permeability distributions obtained using:

- a **local** identification of one value of ω_b for each block independently such that
$$K^b_{ref} - K^b_{\omega_b} = 0, \tag{3.2}$$
resulting in a distribution of ω_b values;

- or a **global** optimization of ω that considers all blocks simultaneously:

$$\omega = \arg\min \left(\sum_{b=1}^{n} ||K_{ref}^{b} - K_{\omega}^{b}|| \right). \tag{3.3}$$

This comparison was performed on three different types of simulations on a fine grid:

- a simple multiGaussian field obtained by SGS (Fig. 3.8),
- a binary mixture of multiGaussian fields obtained by combining SIS facies simulations with SGS (Fig. 3.9),
- and a binary mixture of multiGaussian fields obtained by combining object-based channel simulations with SGS (Fig. 3.10).

These cases were repeated for different upscaling ratios, proportions of shale and proportion of channels, as well as different distributions of permeability. Changes brought by variogram modifications have also been investigated, for several cases: single facies and two facies with 25%, 50% and 75% of shale (simulated with SIS). For this, four variograms have been taken into account (Tab. 3.1).

Variogram name	**Small**	**Large**	**Inter**	**Dual**
Number of structures	1	1	1	2
Type of structures	Exponential	Exponential	Exponential	Exponential
Horizontal range (m)	100	800	250	100 and 800
Vertical range (m)	1	8	4	1 and 8

Table 3.1: Parameters of the four variograms taken into account in our experiments

Detailed results for some cases are shown in Figs. 3.8-3.10. The comparison between the mean and standard deviations of the local and global permeability distributions is provided in Table 3.2.

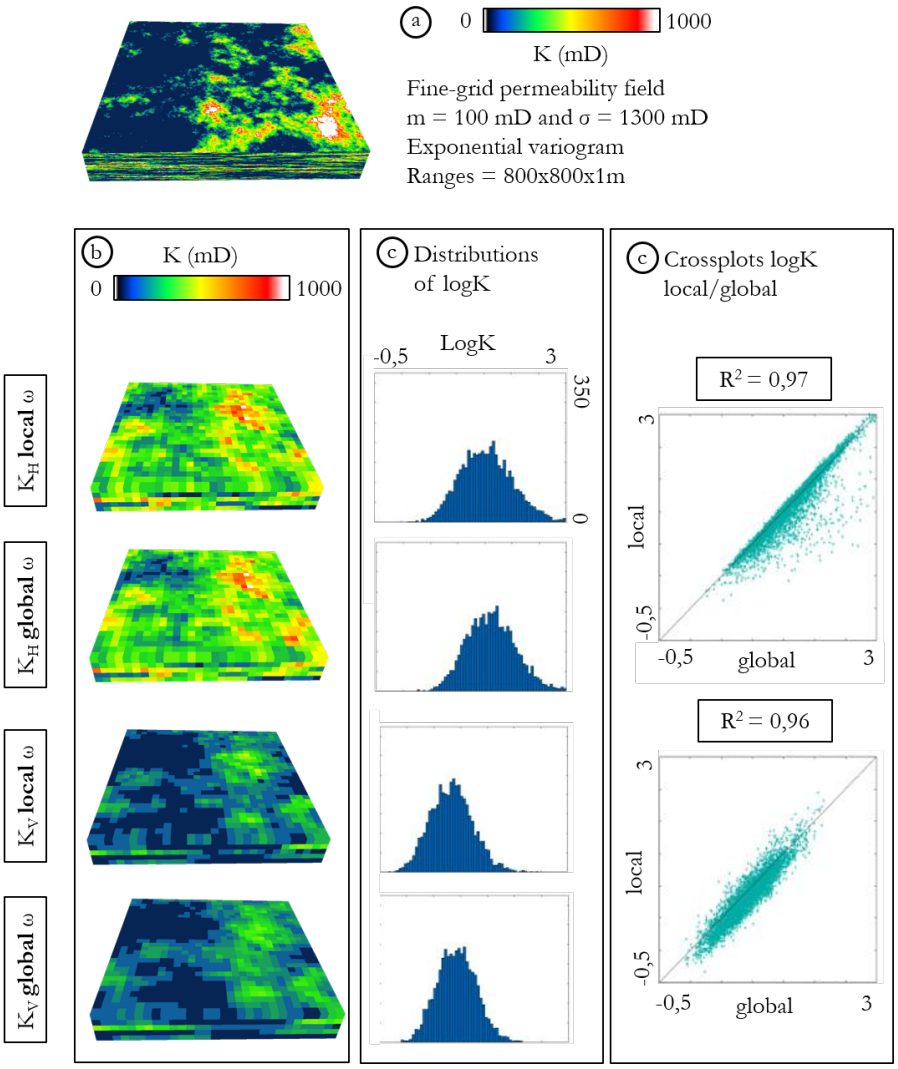

Figure 3.8: Test of the unique ω approximation for a homogeneous case a) permeability field on the fine grid b) local and global upscaled permeability fields (upscaling ratio = 10x10x6 cells) for horizontal (top) and vertical (bottom) directions c) local and global distributions of logK d) cross-plot for the comparison between local and global logK distributions, giving good correlation.

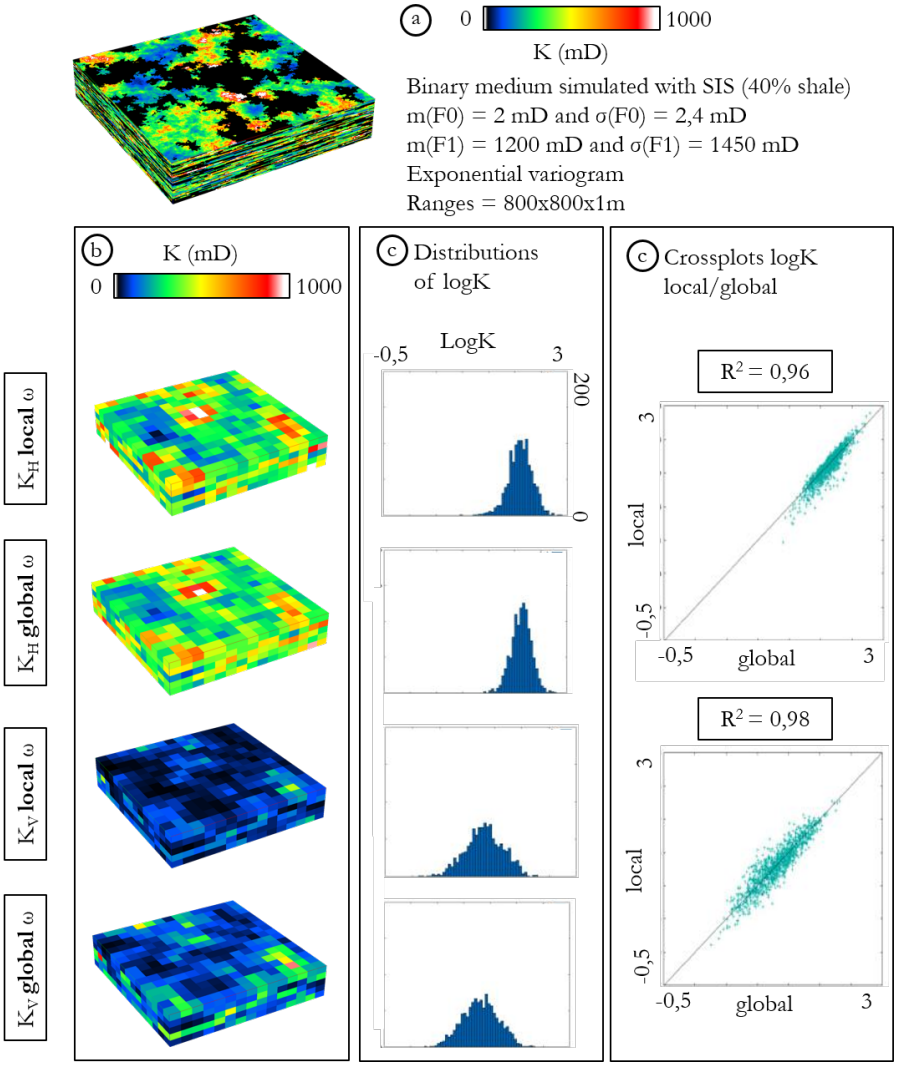

Figure 3.9: Test of the unique ω approximation for a case simulated with SIS (40% of shale) a) permeability field on the fine grid b) local and global upscaled permeability fields (upscaling ratio = 20x20x6 cells) for horizontal (top) and vertical (bottom) directions c) local and global distributions of logK d) cross-plot for the comparison between local and global logK distributions, giving good correlation.

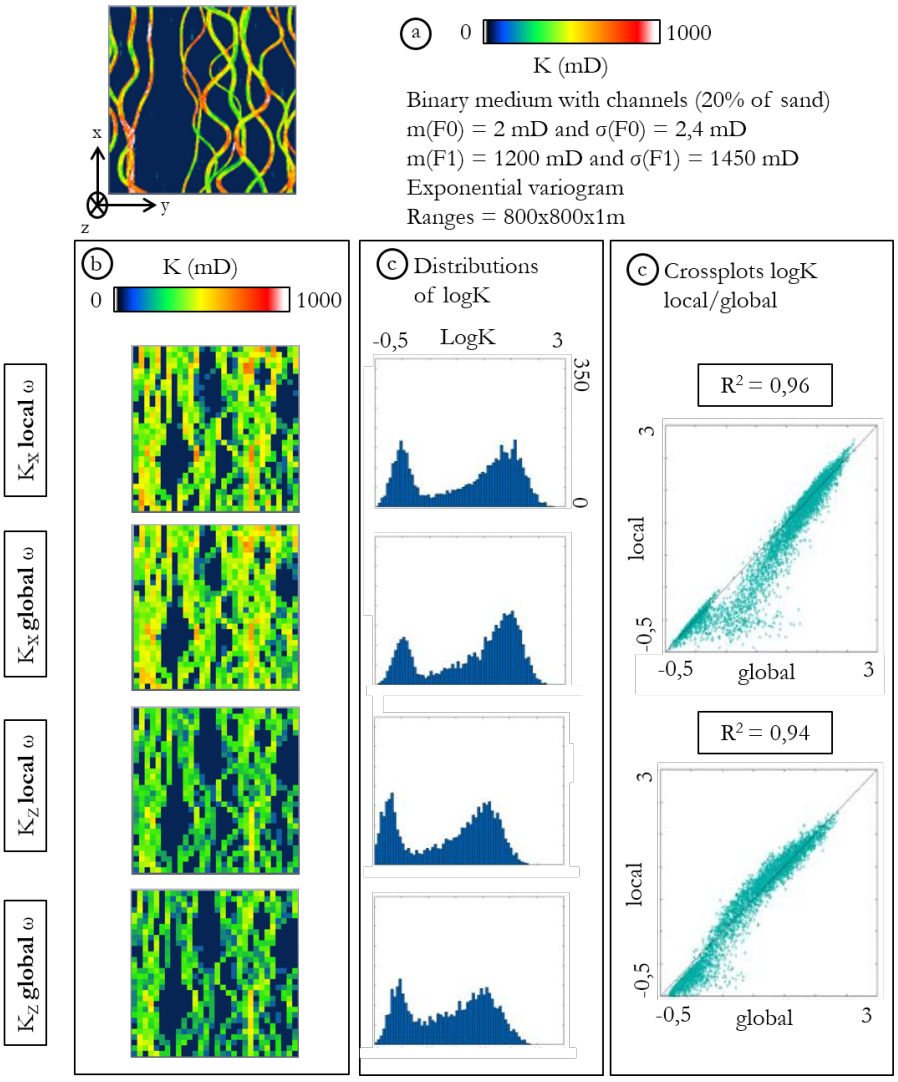

Figure 3.10: Test of the unique ω approximation for a case with channels simulated with an object-based method (20% of sand) a) permeability field on the fine grid b) local and global upscaled permeability fields (upscaling ratio = 20x20x6 cells) for X axis (top) and Z axis (bottom) directions c) local and global distributions of logK d) cross-plot for the comparison between local and global logK distributions, giving good correlation.

		Horizontal permeability						Vertical permeability					
		Global		Local		error		Global		Local		error	
		m (mD)	σ (mD)	m (mD)	σ (mD)	m (mD)	σ (mD)	m (mD)	σ (mD)	m (mD)	σ (mD)	m (mD)	σ (mD)
Single facies	Small	11,74	1,28	11,71	1,50	0,03	- 0,22	10,28	1,12	10,27	1,26	0,01	- 0,14
	Large	15,36	11,03	15,11	11,47	0,25	- 0,44	12,44	8,82	12,32	8,99	0,12	- 0,17
	Inter	13,17	5,64	12,96	6,0	0,21	- 0,36	11,41	4,87	11,28	5,09	0,13	- 0,22
	Dual	13,09	5,74	12,94	5,99	0,15	- 0,25	11,09	4,84	11,01	4,98	0,08	- 0,14
Two facies 50/50	Small	65,32	17,55	64,70	20,23	0,62	- 2,68	41,37	12,92	41,01	15,66	0,36	- 3,74
	Large	95,94	83,91	95,23	87,74	0,71	- 3,83	63,29	74,46	62,78	73,91	0,51	0,55
	Inter	74,05	44,49	73,50	47,62	0,55	- 3,13	54,31	39,30	53,78	39,98	0,53	- 0,68
	Dual	70,21	55,30	70,08	57,41	0,13	- 2,11	46,09	46,79	46,11	47,25	- 0,02	- 0,46
Two facies 75/25	Small	21,16	8,69	20,74	10,27	0,42	- 1,58	11,10	4,88	11,00	5,94	0,10	- 1,06
	Large	44,29	62,83	43,85	65,56	0,44	- 2,73	24,09	46,16	23,93	45,58	0,16	0,58
	Inter	34,98	33,04	33,84	34,79	1,14	- 1,75	22,17	24,70	22,08	25,56	0,09	- 0,86
	Dual	26,13	29,78	24,59	31,28	0,54	- 1,5	13,48	19,24	13,45	19,72	0,03	- 0,48
Two facies 25/75	Small	130,77	24,02	130,54	26,43	0,24	- 2,41	100,57	24,62	100,94	26,41	- 0,37	- 1,79
	Large	152,48	99,80	151,86	104,65	0,62	- 4,85	113,70	98,52	113,18	97,92	0,52	0,60
	Inter	144,34	60,30	143,95	65,29	0,39	- 4,99	122,02	61,11	121,13	63,63	0,89	- 2,52
	Dual	142,98	70,84	142,37	72,92	0,61	- 2,08	112,76	72,43	111,38	71,50	1,38	0,93

Table 3.2: Comparison between permeability distribution mean and standard deviation, for a permeability calculated with a global and a local ω.

The unique ω approximation is acceptable in most cases: 95% of the tested cases had a correlation coefficient between permeabilities obtained using local or global ω values greater than 0.98. The most problematic cases were the ones with object-based channels such as the one presented in Figure 3.10, with a strong contrast between shale and sand permeabilities and a strong anisotropy of the medium due to channels. As a result of these tests, and for the rest of this work, the uncertainty on ω determination for one type of cell is neglected. For one type of cells, sharing the same characteristics (size and proportions), a unique ω will be found by minimizing the global error to reference.

Chapter 4

A new method for direct simulation of permeability on unstructured grids

In this chapter, a new algorithm is proposed to directly simulate permeability on unstructured grids. This method was published in Mourlanette et al. (2020). First, it will be limited to uniform media, i.e. media without facies heterogeneities, but an extension of the method for binary media is presented in Chapter 6.

The algorithm is based on the transform of permeability into an additive property using power averaging formula (see Section 2.3.3):

$$K_\omega = \left(\frac{1}{n} \sum_{i=1}^{n} k_i^\omega \right)^{\frac{1}{\omega}} \tag{4.1}$$

with n the number of points or fine cells in a block, k_i the permeability at point i and ω the averaging exponent. The ω, varying between -1 and 1, has been studied in Chapter 3 and we have shown that ω is scale dependent, but also influenced by the proportion of facies inside the cells. For uniform media, facies proportion is not taken into account, therefore this chapter will only focus on scale dependent ω.

The general workflow of the proposed approach is illustrated in Fig. 4.1 (details are provided in the following sections). The first step is the computation of the size and aspect ratio of each cell of the unstructured grid (Fig. 4.1a).

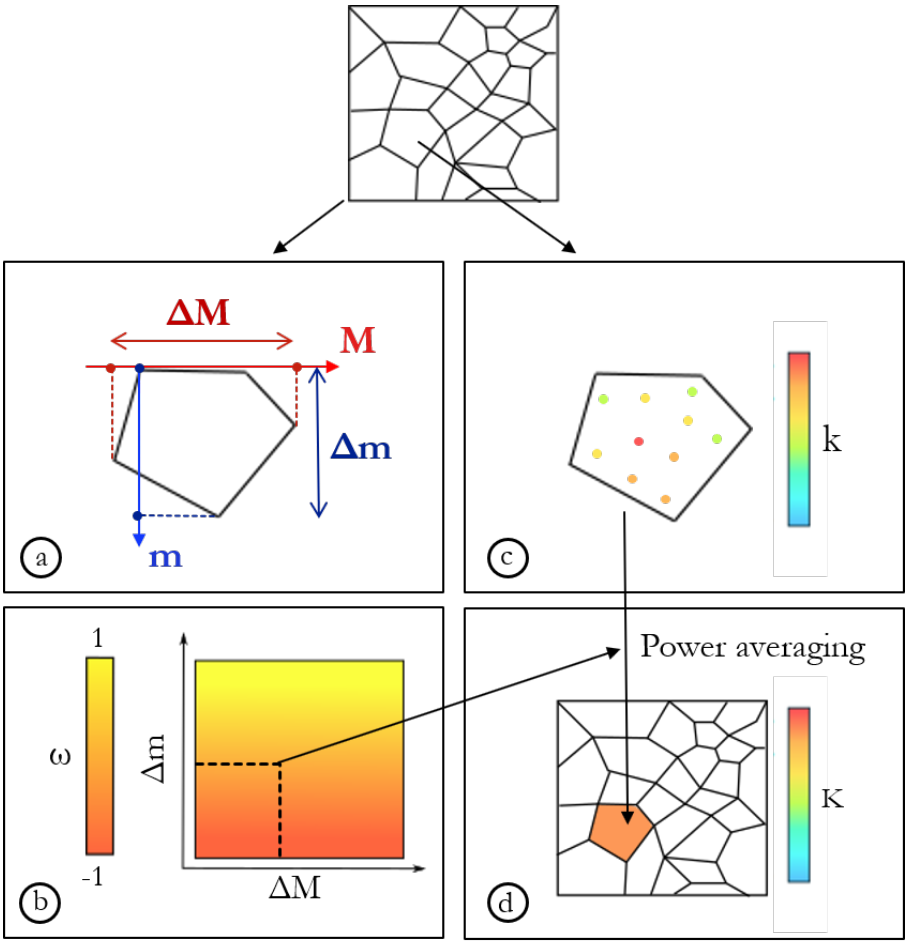

Figure 4.1: General workflow for direct simulation of permeability on unstructured grids. For each unstructured cell, a) we find equivalent dimensions. b) We use these dimensions to constrain a response surface of ω calibrated through upscaling experiments. Then, c) we fill the cells with several integration points and simulate permeability on them. Finally, d) we apply power averaging using the ω estimated in step b).

The second step consists in a series of numerical experiments. They allow to estimate, for any cell geometry, the exponent ω that would minimize the error between 1) the equivalent conductivity estimated using a power average with the ω exponent, and 2) the equivalent conductivity estimated numerically. Since it is not possible to run numerical experiments for all cell sizes, we select some representative cell dimensions

and construct a response surface (Fig. 4.1b). This is done once at the beginning of the procedure.

Then, for every realization, several points are placed inside each cell and the permeability is simulated on these points using the Spectral Turning Bands approach (Fig. 4.1c). The power averaging technique is then applied using the value of ω derived from the response surface to obtain the equivalent permeability of the cell (Fig. 4.1d).

The main strength of this workflow is that the averaging exponents ω are estimated once for a given problem constrained by a permeability distribution, a variogram and an unstructured grid. After that, several realizations of permeability fields can be obtained efficiently using Spectral Turning Bands.

In the following section, we will present how the values of ω are defined for any cell, but before discussing that aspect we must introduce how we define the geometry of the cells of the unstructured grids.

4.1 Characterizing the unstructured cells

A preliminary step is to estimate the geometries of the unstructured cells. Indeed, ω depends on the cell's sizes. Two separate sets of axes are defined (see Fig. 4.2). The XYZ space is characterized by the orientation of the unstructured grid, i.e. the orientation of the bounding box of the grid. The Mmt space is defined following M the principal anisotropy axis given by the variogram, m the minimal anisotropy axis perpendicular to M in the stratigraphic plane and t the vertical axis. In this work, grids are 2.5D, which brings $Z = t$. It is in this depositional space, Mmt, that unstructured cell sizes are defined.

To define the cell sizes, a horizontal aspect ratio H along the Mm axes is defined. It is computed for every cell: all vertices are projected along M and m (Fig. 4.3). Cell's lengths along axes, ΔM_u and Δm_u, are defined by the distance between the furthest projected vertices on the considered axis. The aspect ratio H is obtained by dividing the projected length along M by the one along m: $H = \Delta M_u / \Delta m_u$.

For each unstructured cell, an equivalent regular hexahedral cell is defined through a simple system of equations, so that the volume of the regular cell V_r is equal to the volume of the unstructured cell V_u and that both cells have the same aspect ratio H and thicknesses t_r and t_u,

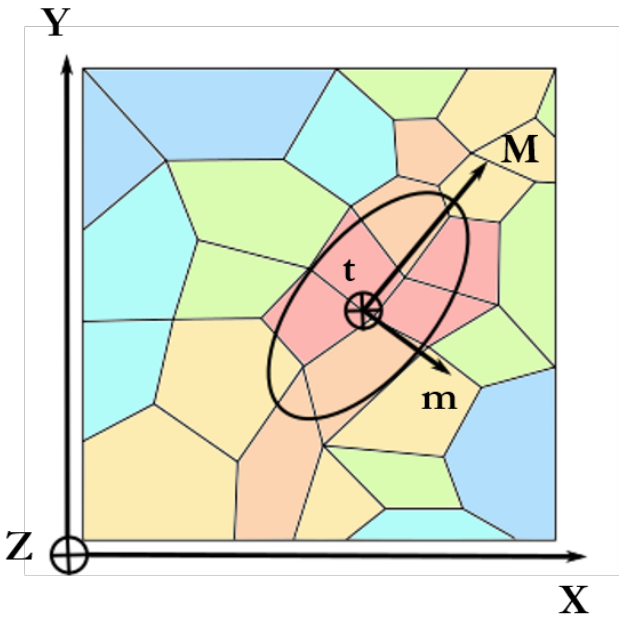

Figure 4.2: Nomenclature of the two sets of axes used in the method. XYZ axes are defined by the grid bounding box orientation. The Mmt axes follow the anisotropy axes of the variogram. The unstructured grid will be considered in Mmt space through projections of the cells on the axes.

respectively:

$$\begin{cases} V_r = \Delta M_r \times \Delta m_r \times \Delta t_r = V_u \\ H = \Delta M_u / \Delta m_u = \Delta M_r / \Delta m_r \\ \Delta t_u = \Delta t_r \end{cases} . \tag{4.2}$$

ΔM_u, Δm_u, Δt_u and V_u being known, the dimensions of the equivalent rectangular cell are obtained for every cell of the unstructured grid:

$$\begin{cases} \Delta M_r = \sqrt{\frac{H \times V_u}{\Delta t_u}} \\ \Delta m_r = \sqrt{\frac{V_u}{H \times \Delta t_u}} \\ \Delta t_r = \Delta t_u \end{cases} \tag{4.3}$$

For a non-extruded unstructured grid, the third equation of the system should be replaced by a vertical aspect ratio $V = mean(\Delta M, \Delta m)/\Delta t$.

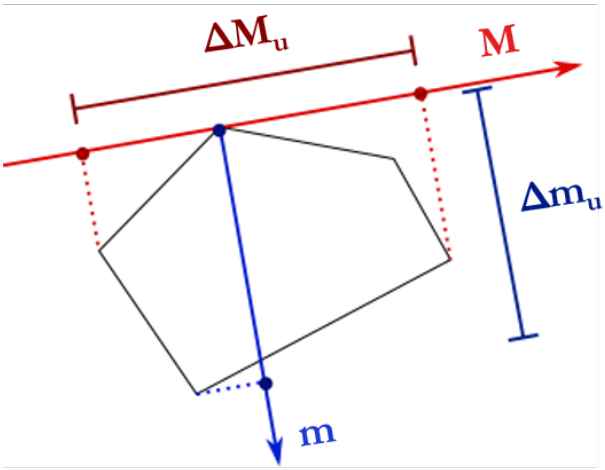

Figure 4.3: Definition of the horizontal aspect ratio H. The distance ΔM_u is obtained by projecting the cell's vertices on the M axis and taking the length between the two extremal points. The same process is applied for the m axis.

Describing the unstructured cells in Mmt space means that the permeability tensor will be considered in this space. For the flow simulators, however, permeability has to be given in XYZ space. An additional step at the end of the workflow has to be implemented to rotate the permeability matrix from Mmt space to XYZ. For simplicity, however, the remainder of this work considers that Mmt axes are aligned to XYZ axes, coherently with the chosen horizontally isotropic grids and variograms used for the simulations.

4.2 Generating surfaces of response of omega

In the method presented hereafter, ω is estimated for each cell using a response surface methodology. It allows accounting for the different parameters having an influence on ω, and determining a local ω characterizing each cell of the unstructured grid. Following Nœtinger and Haas (1996) and Massonnat (2009), experiments show that three main parameters influence ω: variogram ranges, proportions of facies, and cell geometry. In this chapter, the focus is put on cells geometry (size and aspect ratio) and we neglect for the moment the presence of multiple facies to keep the response surfaces simple and tractable.

4.2.1 Defining a space of parameters for the response surface

To obtain the response surface, the first step consists of choosing N points in the parameter space where the response has to be evaluated. The dimension D of the parameter space depends on the type of unstructured grid (Fig. 4.4a):

- $D = 2$ for a 2D unstructured grid: taking into account cell's sizes along M and m axes
- $D = 2$ for a 3D unstructured grid with constant cell's size on t axis: taking into account cell's sizes along M and m
- $D = 2$ for a 3D horizontally isotropic grid: taking into account the cell's sizes along t axis and the average of the cell's sizes along M and m axes
- $D = 3$ for a 3D unstructured grid: taking into account cell's sizes along M, m and t axes

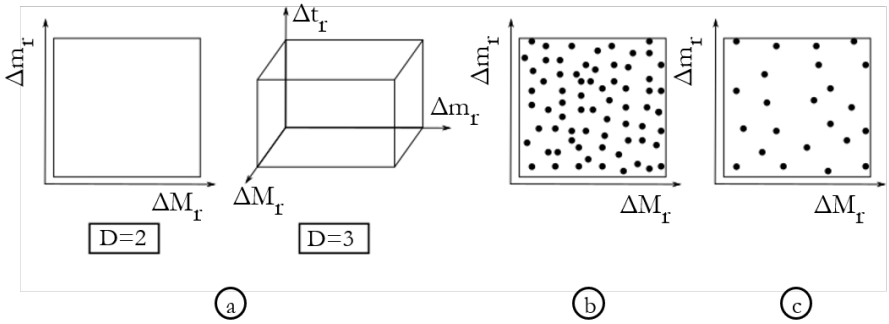

Figure 4.4: a) Example of parameter space for $D = 2$ and $D = 3$. b) Placing P random points to cover the entire space. c) Choosing N experiments uniformly placed in the space.

For each of the D dimensions, the minimum and maximum of the sizes of the equivalent rectangular cells (ΔM_r, Δm_r and Δt_r) is computed to limit the ranges of possible cell sizes. A set of P points is then randomly and uniformly placed in the parameter space. Each point corresponds to a D-dimensional vector of the form (ΔM_r^i,Δm_r^j,Δt_r^k). The number of points P should be large enough to cover the entire

space (Fig. 4.4b). Among those P points, N are chosen using the Wootton, Sergent, Phan-Tan-Luu (WSP) (Sergent, 1989; Sergent et al., 1997a,b) space-filling design technique: from a set of candidate points, well-distributed experiments are selected following an iterative process depending on an exclusion sphere (Santiago et al., 2012)(Fig. 4.4c). The chosen points are not necessarily uniformly spaced, but the algorithm allows the best coverage of the domain possible.

4.2.2 Performing the experiments

A value of ω is then estimated for each of the N points of the parameter space: for each point having D coordinates representing cell sizes, e.g., ΔM_r^{exp}, Δm_r^{exp} and Δt_r^{exp} if $D = 3$, we use a fine regular grid aligned on the Mmt axes to simulate several realizations of fine-scale permeability. These fine values are then upscaled with a pressure solver using upscaling ratio corresponding to the coordinates of the point treated, i.e. we create upscaled blocks of the size of the equivalent hexahedron of interest. It gives a distribution of reference upscaled permeability values, from which we find the ω corresponding to the power averaging distribution that best fits the reference distribution. The details of this calibration are given bellow.

The fine grid for the fine-scale simulations is defined once, using $\Delta M_r^{smallest}$, $\Delta m_r^{smallest}$ and $\Delta t_r^{smallest}$ (respectively $\Delta M_r^{biggest}$, $\Delta m_r^{biggest}$ and $\Delta t_r^{biggest}$) which are the dimensions of the equivalent rectangular cell corresponding to the smallest (respectively the biggest) unstructured cell in the grid (Fig. 4.5 top). The idea is to create a fine grid covering at least eight equivalent rectangular cells (2 along each axis): the bounding box of this structured grid must have dimensions G_M^s, G_m^s and G_t^s such that $G_M^s \geq 2\Delta M_r^{biggest}$, $G_m^s \geq 2\Delta m_r^{biggest}$ and $G_t^s \geq 2\Delta t_r^{biggest}$. The voxels of this grid have dimensions c_M^s, c_m^s and c_t^s such that $c_M^s \leq \Delta M_r^{smallest}$, $c_m^s \leq \Delta m_r^{smallest}$ and $c_t^s \leq \Delta t_r^{smallest}$ (Fig. 4.5 bottom).

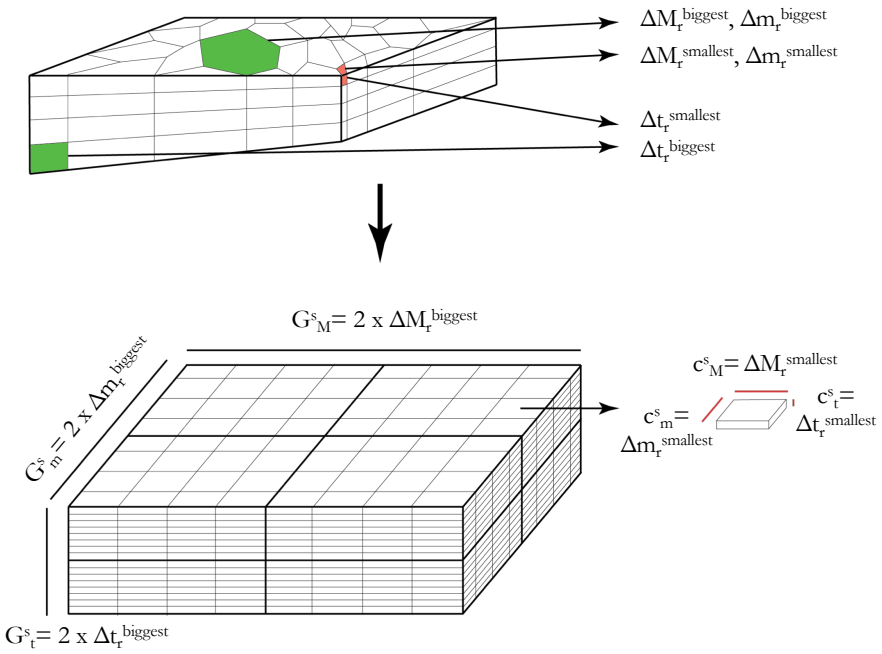

Figure 4.5: Definition of the structured grid on which we perform the experiments. We take into account $\Delta M_r^{smallest}$, $\Delta m_r^{smallest}$, $\Delta t_r^{smallest}$ and $\Delta M_r^{biggest}$, $\Delta m_r^{biggest}$, $\Delta t_r^{biggest}$, which are the dimensions of the smallest and biggest unstructured cells.

Then, each experiment is performed as follows:

- A fine-scale permeability k is simulated on the local grid using Spectral Turning Bands (Mantoglou and Wilson, 1982; Emery et al., 2016), with a distribution and variogram corresponding to the fine scale (Fig. 4.6a). This step is repeated R times with a different seed for random number generation. The permeability distribution can be of any type including lognormal and beta. This distribution may characterize the values of permeability or the values of log-permeability. In the latter case, the fine-scale permeability values are normalized using a power of 10. The rest of the experiment is then performed on this normalized property.

- Upscaling ratios U_M, U_m and U_t, are set using cell's sizes corresponding to the current experiment: $U_M = \Delta M_r^{exp}/c_M^s$, $U_m = \Delta m_r^{exp}/c_m^s$ and $U_t = \Delta t_r^{exp}/c_t^s$.

- R upscaled permeabilities, called reference permeabilities K_{refM}, K_{refm} and K_{reft}, are computed using a pressure solver upscaler (see Section 3.1) with U_M, U_m and U_t as upscaling ratios (Fig. 4.6b). It gives a distribution of K_{ref} values in each direction.

- The values of ω_M, ω_m and ω_t for this experiment are determined by minimizing the global error between K_{ref} and the power average K_ω, i.e. minimizing the sum of the error for the n upscaled blocks (Fig. 4.6c):

$$\sum_{block=1}^{n} \| \log\left(K_{ref}^{block}\right) - \log\left(K_{\omega}^{block}\right) \| \tag{4.4}$$

  In practice, determining ω is done using an optimization method that first tries to fit a parabola equation to the error function and find its minimum, and, if not successful, uses a golden search method. The error function can have various shapes, going from a parabola to a simple monotonous curve (Fig. 4.7).

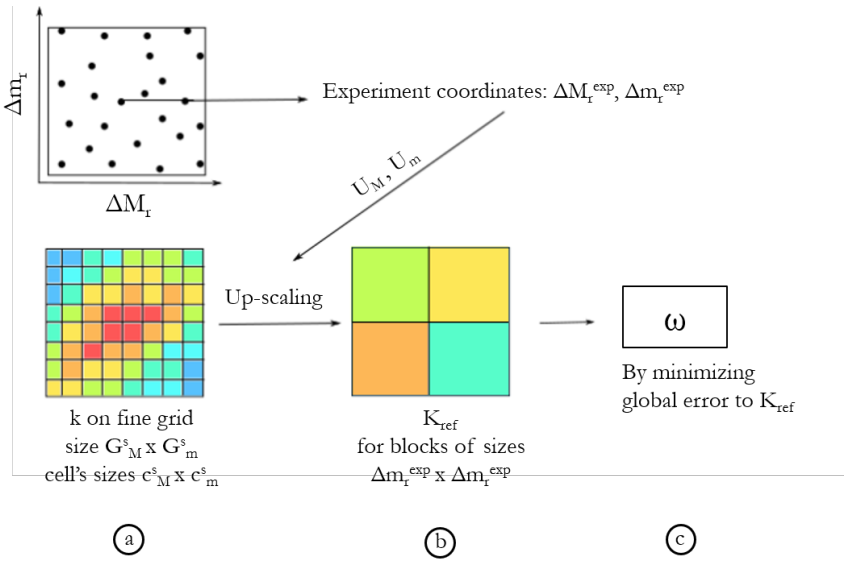

Figure 4.6: a) Simulation of permeability on the fine grid. This step is performed R times. b) Numerical upscaling using the experiment cell sizes to calculate upscaling ratio. This step is also performed R times. c) Optimizing the global error to the reference distribution to obtain an ω.

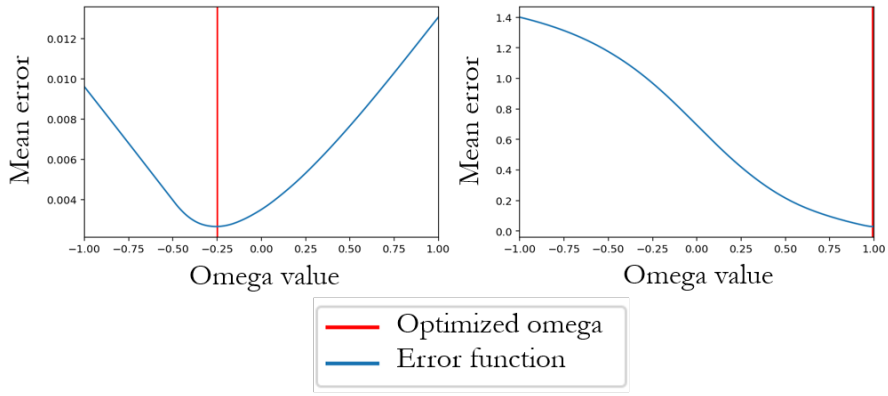

Figure 4.7: Examples of ω calculation: optimization of the error through a parabola fitting or golden number algorithm.

Typically, the number R of fine-scale permeability realizations must be large enough so that the reference distribution K_{ref} has a statistically sufficient number of values to identify a robust value for ω. In the case of the biggest possible equivalent hexahedron (of size $\Delta M_r^{biggest}$, $\Delta m_r^{biggest}$ and $\Delta t_r^{biggest}$), we obtain eight upscaled values for one realization: the fine grid has been defined such that eight biggest hexahedra can be overlaid on it. It means that in this case, ω will be fitted on $n = 8R$ values, which is the limit to take into account when choosing the number R. In parallel, in the case of a small equivalent hexahedron, we will obtain a large number of reference values for each realization, because the fine grid is not adapted to the local problem. This large number will also be multiplied by R, which gives too many unnecessary values to fit an ω and brings an additional computational cost. To fix this problem, if the cell size for the treated experiment is smaller than $\Delta M_r^{biggest} \times \Delta m_r^{biggest} \times \Delta t_r^{biggest}$, only the region of the fine grid of size $2\Delta M_r^{exp}$, $2\Delta m_r^{exp}$ and $2\Delta t_r^{exp}$ is simulated and consequently upscaled. By doing so, K_{ref} distribution always has $n = 8R$ values to fit an ω.

4.2.3 Obtaining surfaces of response of ω

Once all numerical experiments have been performed, an interpolation between the points of the parameter space is done using kriging (Fig. 4.8a and 4.8b). The correlation function for kriging is assumed

stationary and written as follows:

$$R(x,y) = exp\left(-\sum_{j=1}^{D}\left(\frac{\mid x_j - y_j \mid}{\theta_j}\right)^p\right) \tag{4.5}$$

with $1 < p \leq 2$ and D the number of dimensions of the response surface. The hyper-parameters θ_j, characterizing kriging anisotropy, can be estimated using the maximum likelihood method. However, to avoid artifacts on surfaces of response in our work, all θ_j have been set to one in the normalized space. The resulting response surface allows determining the exponent ω for each cell of the unstructured grid (Fig. 4.8c).

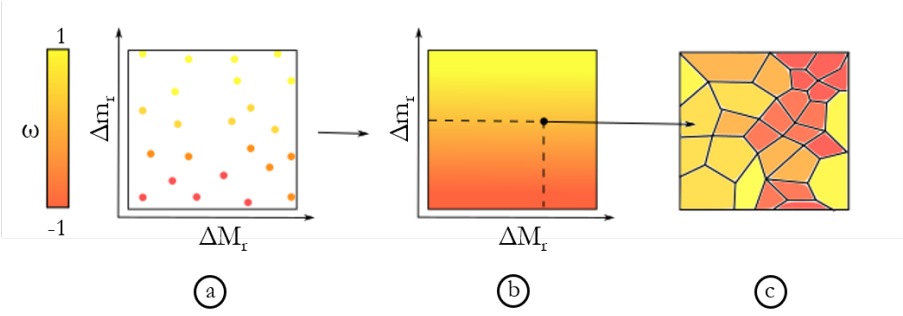

Figure 4.8: a) All experiment results, i.e. ω, are put in the parameter space. b) A simple kriging allows the generation of a surface of response of ω. c) By projecting cell sizes on the response surface, one ω is found for every cell of the unstructured grid.

As explained previously, in each experiment the upscaling is done in two or three directions resulting in different K_{ref} (M, m or t). Then, two or three values for ω are obtained per experiment, one for each direction D. In the end, not one but two or three response surfaces of ω are interpolated and the same amount of omega properties are painted on the unstructured grid.

4.3 Direct simulation of permeability on the unstructured grid

The next step is to simulate rapidly values on integration points using Spectral Turning Bands (STB) and average them using the estimated ω. The integration points are obtained with a fast generation of

quasi-random Sobol' sequences using the method of Antonov and Saleev (1979).

First, we simulate and store Spectral Turning Bands as detailed in Section 2.2.2, which allows the simulation of each unstructured cell independently from the others. For each cell, a number of random locations to select is calculated depending on the cell's volume (Fig. 4.9a). The fine permeability values at these locations are simulated as explained above (Fig. 4.9b). The global cell value is obtained by averaging the point values using the power law and the ω estimated for that cell (Fig. 4.9c). Once again, not one but two to three permeability values are obtained, one for each direction M, m and t.

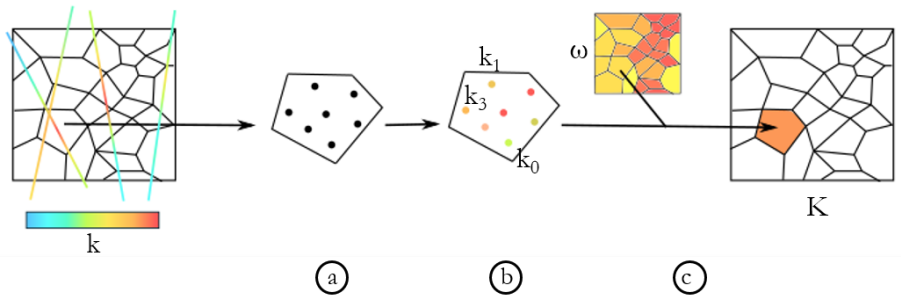

Figure 4.9: a) One by one, each unstructured cell is filled with points, the number of points depending of the volume of the cell; b) Using the Spectral Turning Bands, permeability is interpolated on these points; c) Using the ω of the target cell, the permeability of the cell is obtained using power averaging formula on the points (followed by a back transform from K^ω to K)

Chapter 5

Application of the approach to a synthetic case

The methodology has first been tested on simple cases with known analytical solutions (perfectly layered case, isotropic log-normal distribution, etc.). It provides coherent results that will be illustrated in the following section. We will then show the results of the application of the method to a synthetic but realistic example. We illustrate first the simulation of the permeability and then the impact on tracer simulations. A discussion on computation times is available at the end of this chapter.

5.1 Cases with known analytical solution

The upscaling of a perfectly stratified infinite media has a well-known solution inspired by the fundamental inequality (see section 2.3.2). In the case of layers perpendicular to the flow, the equivalent permeability will be the harmonic mean, whereas for parallel layers it will be the arithmetic mean. The aim of the first test is to verify if the program respects these limit cases. On a grid of 250x250x100 cells of 2x2x0.5 meters, three properties of permeability are created. They are composed of alternate low (0.1 mD) and high (10 mD) permeability layers (Fig. 5.1). One layer is two cells thick in M, m or t direction, depending on the property. We recall that in our work, Mmt axes are taken aligned to XYZ axes.

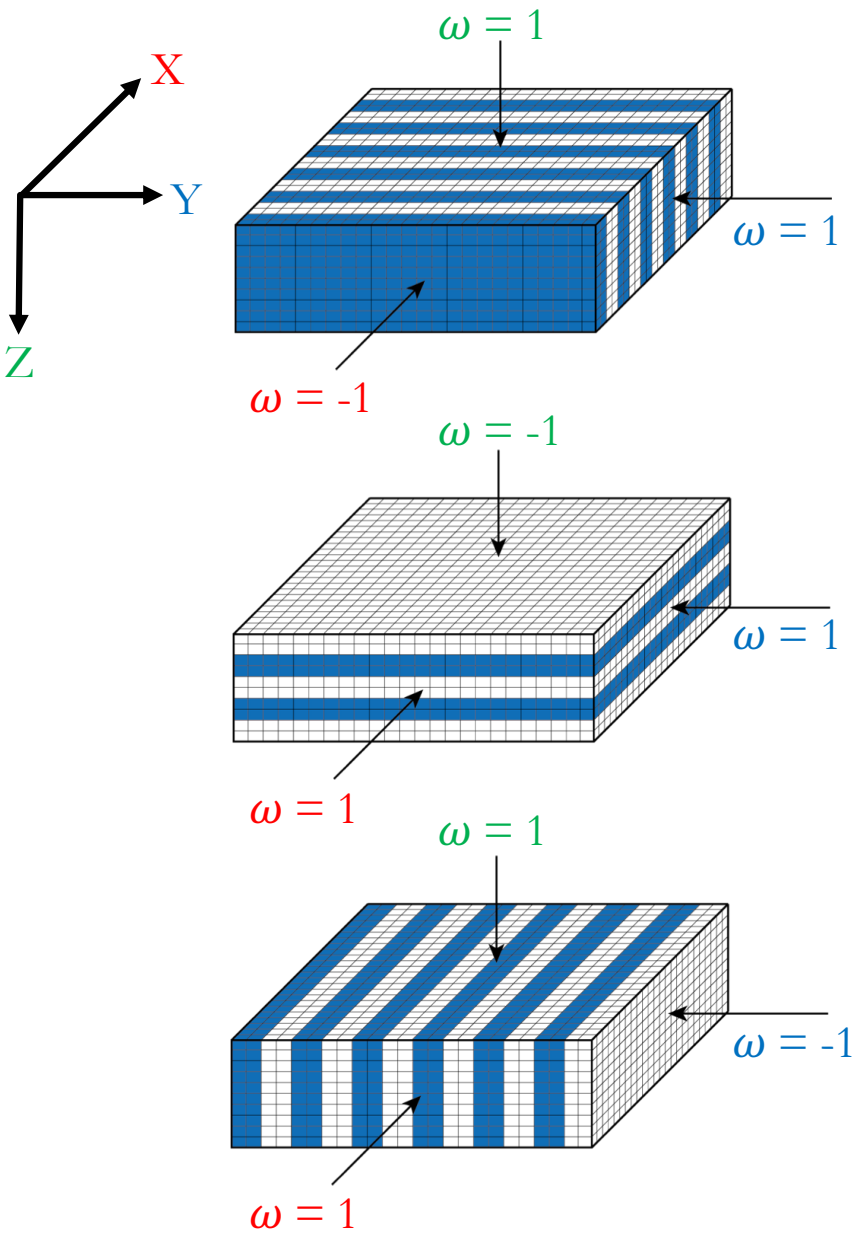

Figure 5.1: Graphic representation of the three tests performed for stratified media, the grid is presented with a scale 1/10 for the number of cells. The ω in red, green and blue represent the analytical exact solution.

On each of these properties, twenty experiments are performed to create three surfaces of response of omega: one in every direction of the space. These surfaces should be constant and either equal to one or minus one, except for really small cells of size inferior to a layer's size.

As expected, results show that all surfaces of response are following the analytical solution, for confined boundary conditions of the numerical upscaler. For open boundary conditions, the fluxes go through the sides of the model resulting in omega not equal to minus one in the direction perpendicular to the layers. It highlights the necessity of choosing the correct upscaler and its relevant parameters.

Another case is tested using a permeability field with vertical pillars of high and low values (Fig. 5.2a).

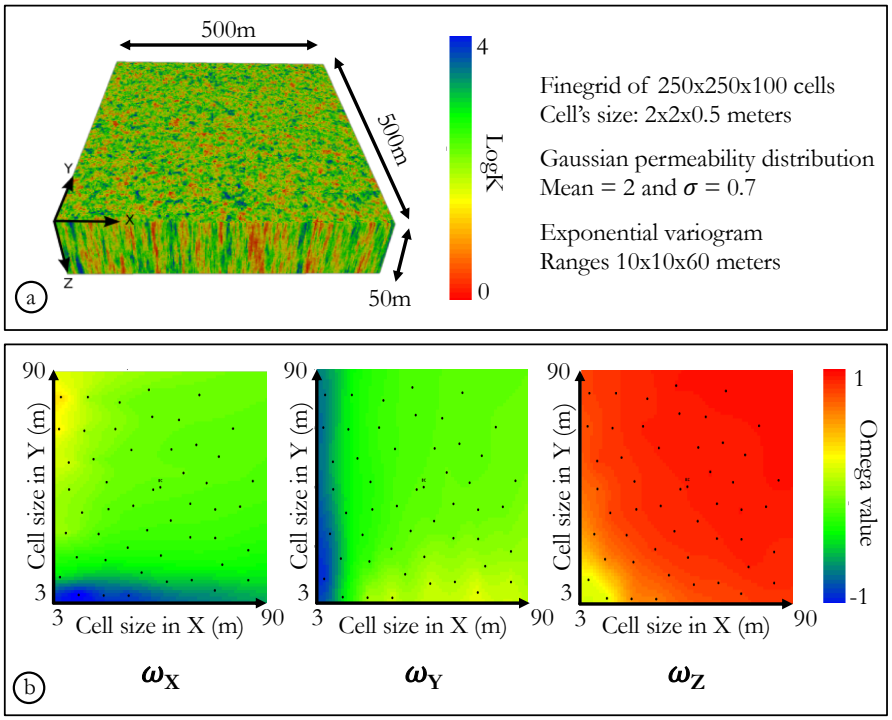

Figure 5.2: a) Permeability field on the grid. It shows vertical pillars of high and low permeability. b) Surfaces of response for ω_X, ω_Y and ω_Z.

To generate the property, the same grid of 250x250x100 cells of 2x2x0.5 meters is used. We peform a SGS with a Gaussian distribu-

tion of mean 2 and standard deviation 0.7. The variogram is isotropic and very small in X and Y axes (10 meters) and large in Z direction (60 meters).

Fifty experiments are performed, resulting in three surfaces of response (Fig. 5.2b). For understanding purposes, the surfaces of response are presented in 2D, taking into account varying cell sizes (i.e. upscaling ratios in the experiments) in X and Y directions and a constant cell size in the Z axis. Along X and Y axes, equivalent permeability has to be equal to the geometrical mean, which corresponds to an omega tending toward zero. Along the Z axis, equivalent permeability must be equal to the arithmetic mean, corresponding to an omega of one. As seen on Figure 5.2, except for limit cases of cell shapes on the sides of the response surfaces, where it is normal to have different values considering the sizes of the cells, the analytical solutions are respected.

5.2 Synthetic case

In this section, we will illustrate the method with a synthetic but realistic example (Fig. 5.3). We consider a confined aquifer of 2km by 2km with negligible ambient flow. The external boundaries are assumed to be impermeable. The thickness of the aquifer is varying linearly from 40 meters in the eastern side to 4 meters in the western side. Ten wells are positioned across the aquifer. Three of them are injecting water and seven are pumping (Fig. 5.9). A tracer is injected in one of the injectors and recovered in the pumping wells. This setup was designed to test the proposed geostatistical simulation technique on a realistic unstructured grid and to compare the results of the tracer simulation with a fine scale simulation (standard approach).

In the following sections, we describe first the simulation of the permeability and then the tracer simulations.

5.2.1 Permeability simulation

The 3D unstructured grid for this case is composed of 18,250 Voronoï cells with a volume between 25 m^3 and 50.10^3 m^3 (Fig. 5.3a). The grid is refined around all ten wells. The variogram for both porosity and permeability has two Gaussian structures of equal contribution with ranges of 25x25x2.5 meters and 250x250x25 meters for cell sizes varying between 3 and 90 meters horizontally and 0.8 to 8 meters vertically (Fig. 5.3b). The porosity has a beta distribution of mean 0.15 and

standard deviation 0.05 (Fig. 5.3c) and the permeability distribution is lognormal with a mean of 100 mD and a standard deviation of 300 mD (Fig. 5.3d). The boundary conditions for the upscaler in the experiments are of permeameter-type, i.e. no-flow conditions on the sides.

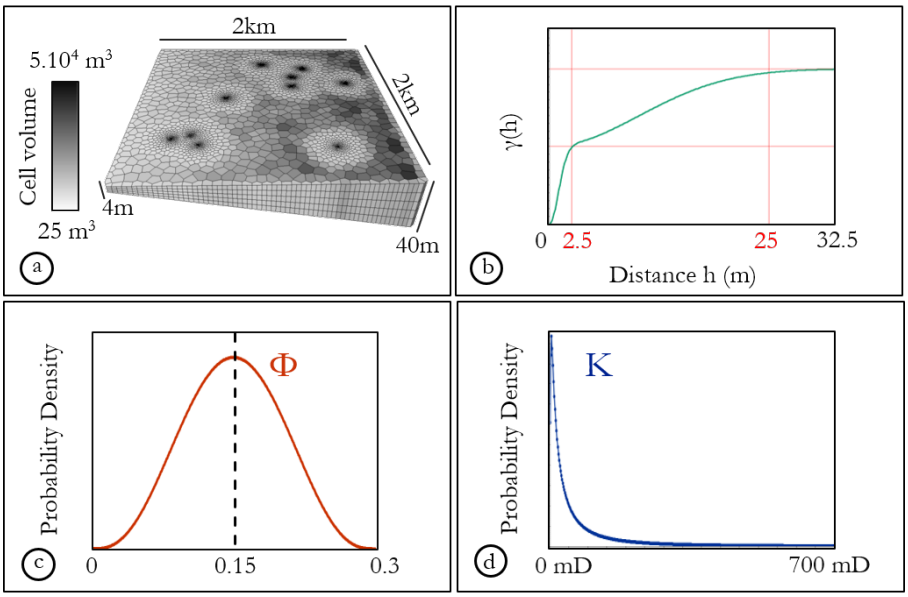

Figure 5.3: a) grid for the synthetic case with cell volumes varying with a factor 2.10^3. b) double structure vertical variogram used for the simulation of both petrophysical variables. c) beta distribution of porosity, with m=0.15 and σ=0.05. d) lognormal distribution of permeability, with m=100mD and σ=300mD.

It is important to note that, in practice, the variogram used for simulating petrophysical variables, while describing exactly the same structures, varies between the surface of response process and the actual simulation on the unstructured grid. Indeed, the surface of response computation relies on a structured Cartesian grid defined in the geological space by XYZ coordinates, while the simulation on the unstructured grid is performed in the parametric space with UVT coordinates (for more details on UVT-transform, see Mallet (2004)). The variogram used for surfaces of response will then have a vertical range corresponding to meters while the one used for unstructured grids simulation will have a vertical range corresponding to a normalized time. For this reason, the double structure variogram for simulation on the unstructured grid

is defined with vertical ranges of 0.114 and 1.14. It is the result of the following calculation: the vertical ranges in XYZ space are 2.5[m] and 25[m] for an average thickness of the grid of 22 meters. By normalizing between 0 and 1 for T axis, we obtain $2.5/22 = 0.114$[-] and $25/22 = 1.14$[-].

Due to the horizontal isotropy of the aspect ratio of the unstructured cells, the Mmt axes presented in section 4.1 are taken aligned to XYZ axes. For the same reason, X axis and Y axis being equivalent, only two response surfaces are presented hereafter: one for the horizontal exponent $\omega_H = \omega_X = \omega_Y$ and one for the vertical exponent ω_V (Fig. 5.4). The two axes of the response surfaces represent the horizontal cell sizes ΔXY (taken as the mean of the cell sizes in X and Y), and the vertical cell sizes ΔZ. A smooth variation of ω is observed, from 0 to 1 for ω_H and from -1 to 1 for ω_V.

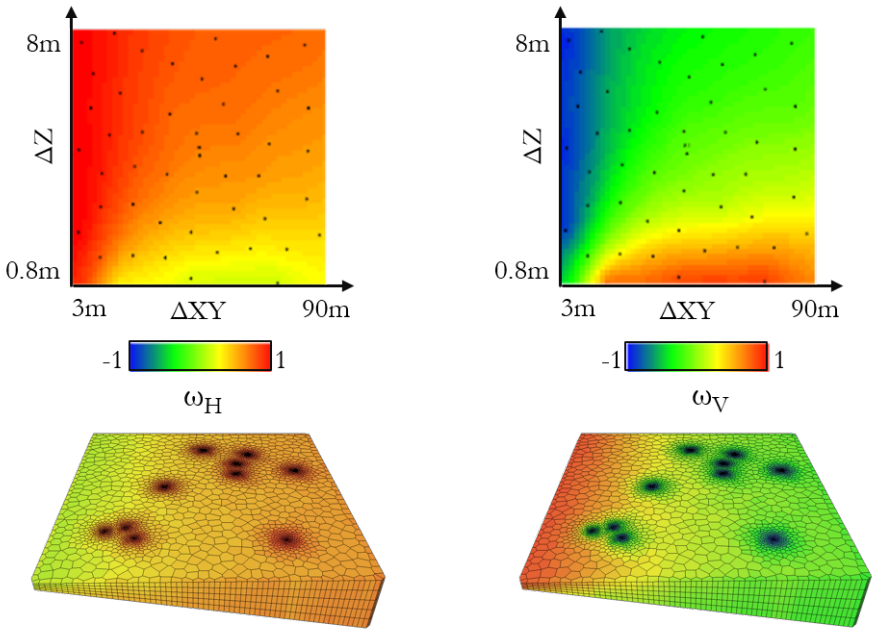

Figure 5.4: Surfaces of response of horizontal and vertical omega and the corresponding properties on the unstructured grid.

The log of permeability is assumed to be correlated to point-support porosity with a correlation coefficient of 0.8, which is possible using Spectral Turning Bands. Porosity on the unstructured grid is obtained using the arithmetic mean (Fig. 5.5) and the two permeabilities (H and

V) are simulated using the power averaging formula and ω properties generated previously (Fig. 5.6a).

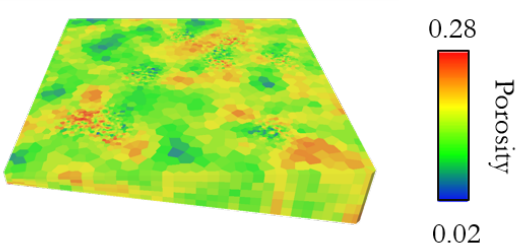

Figure 5.5: Porosity field on the synthetic example. Permeability will be correlated to this field with a factor 0.8.

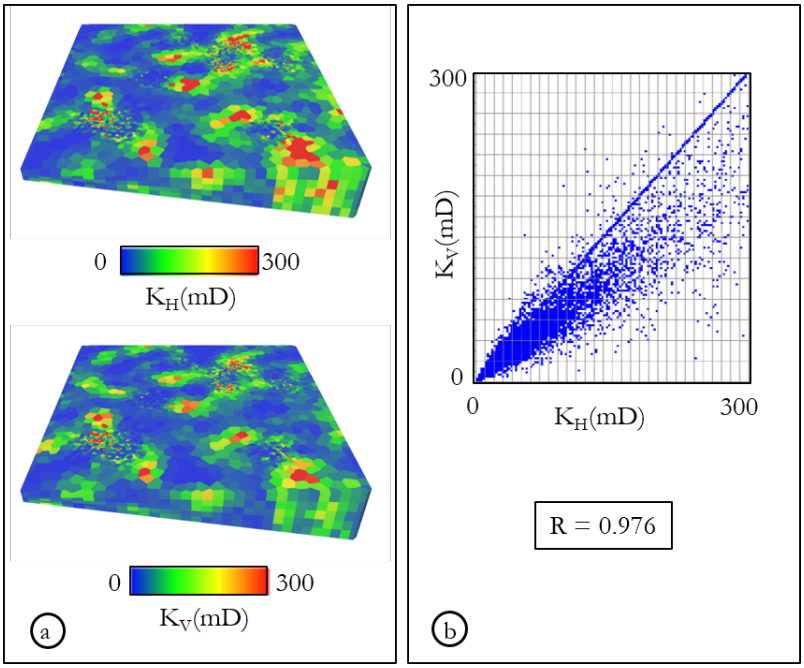

Figure 5.6: a) Vertical and horizontal permeability fields on the toy example. b) Cross-plot K_H vs. K_V, K_V being globally inferior to K_H.

Although both K_H and K_V properties look similar, the cross-plot on Figure 5.6b shows that K_V is globally inferior to K_H. Some cells, identified as large along XY axes and really small along Z axis, present

a $K_V > K_H$. Although a bit counter-intuitive for geologists, this inequality is also the one given by the pressure solver upscaler for this kind of cells and is inherent to both the cell shape and size and the boundary conditions chosen, here confined conditions (Fig. 5.7).

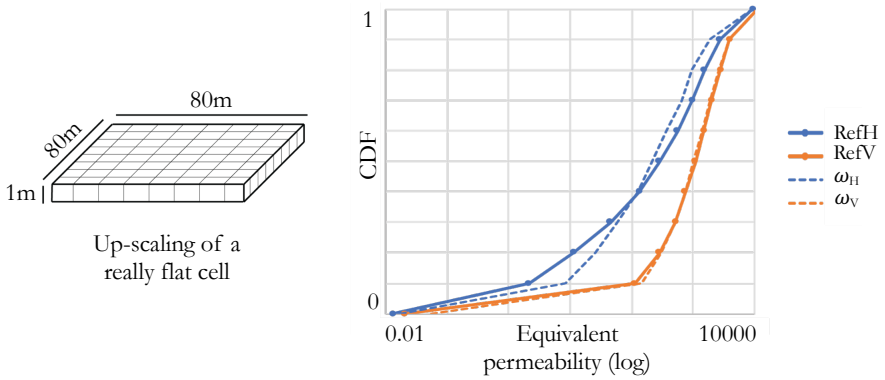

Figure 5.7: Results of the upscaling of a really flat cell: upscaling by pressure solver (reference) in full line and upscaling by power averaging with our ω in dash line. For both upscaling techniques, the CDF of K_V is above the one of K_H.

5.2.2 Tracer tests

Tracer simulations are performed accounting only for advection and neglecting diffusion and physical dispersion. The tracer response computed using the unstructured grid presented above is compared to the response computed using a fine structured grid having the same areal extension. The aim is to test if the permeability field obtained with the proposed method gives a coherent tracer response. The fine grid has 600x600x80 cells of horizontal size 3.3x3.3 meters and vertical size from 0.05m to 0.5m. Using STB, it is possible to obtain the same random field on the points placed in the structured and unstructured cells. For the structured one, a single point is taken per cell, while the number of points in each unstructured cells depends on its volume. Then, for unstructured cells, the cell average value is obtained using either arithmetic average (for porosity) or the power averaging (for permeability). The structured grid being very fine, it preserves all the details of the random field, it is considered as our reference. On the unstructured grid, the details are only seen around the wells, where the grid is re-

fined. Twenty realizations of porosity and correlated permeability are generated on both grids, one example is displayed on Fig. 5.8.

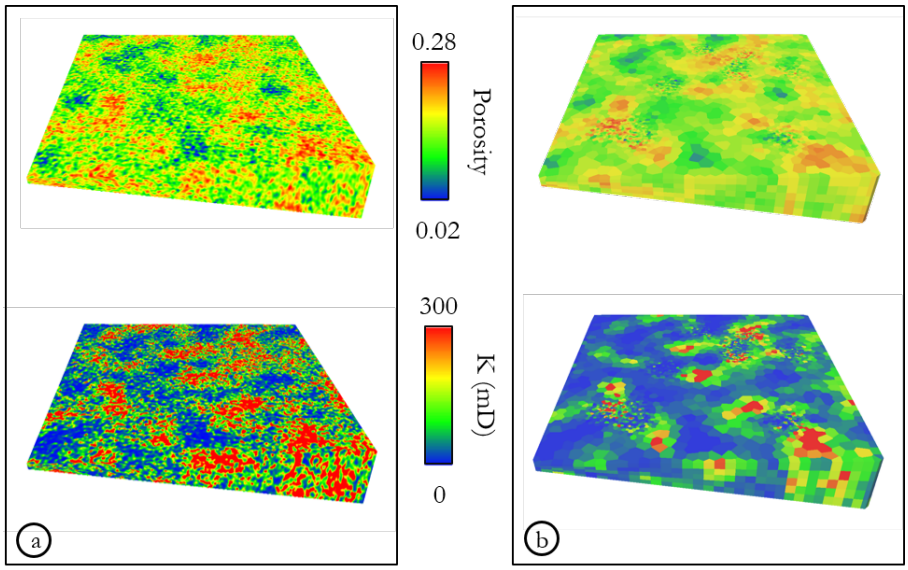

Figure 5.8: a) Simulation of porosity and permeability on the fine structured grid. b) Simulation of porosity and permeability on the coarser unstructured grid. Details are maintained in the most refined zones.

For each realization, a passive tracer is injected in a water saturated reservoir having one well injecting the tracer, two wells injecting water and seven production wells (Fig. 5.9).

The water production rate per well is 120 m^3/day and the water (and tracer) injection rate per well is 280 m^3/day. We observe the concentration of tracer at the producers for the twenty realizations (Fig. 5.10).

For individual realizations, some local deviations are observed between the tracer curves of the fine structured reservoir (Fig. 5.10a) and the ones of the unstructured grid (Fig. 5.10b). However, in terms of uncertainty assessment, the set of tracer curves shows a very consistent behavior for both grids. The curves for structured reservoir are slightly more scattered, which is coherent with the better precision offered by this grid. The Q10, Q50 and Q90 quantile curves (Fig. 5.10c) are almost identical, with some minor differences on Q10. A 3D visualization of the tracer's concentration evolution shows similar results on structured and unstructured grids (Fig. 5.11). This similarity is further demonstrated by the visualization of the mean of the twenty realizations of the tracer's

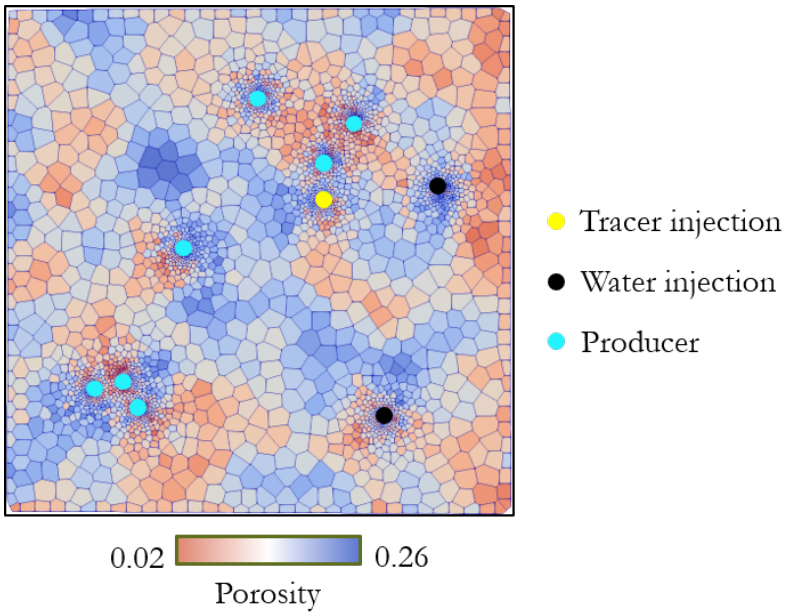

Figure 5.9: Placement of the wells in the unstructured reservoir (painted with a random property of porosity upscaled arithmetically from points simulated with STB). There are seven producing wells, one injecting tracer and two injecting water. The placement of wells is identical on the fine structured reservoir.

concentration evolution at time thirteen years, where concentration tendencies are well respected (Fig. 5.12).

As expected for a coarser grid, these results show that the unstructured grid does not preserve the details of the propagation visible on the structured grid, horizontally and vertically. This highlights the importance of the choice of unstructured grid: the errors are localized in areas between wells where the unstructured grid seems too coarse. Overall, this comparison demonstrates the consistency of the proposed method as compared to the results obtained with a structured grid. However, the computational times are very different. The tracer test simulations on the structured grid takes 112 minutes in average, while they only take 4 minutes on the unstructured grid.

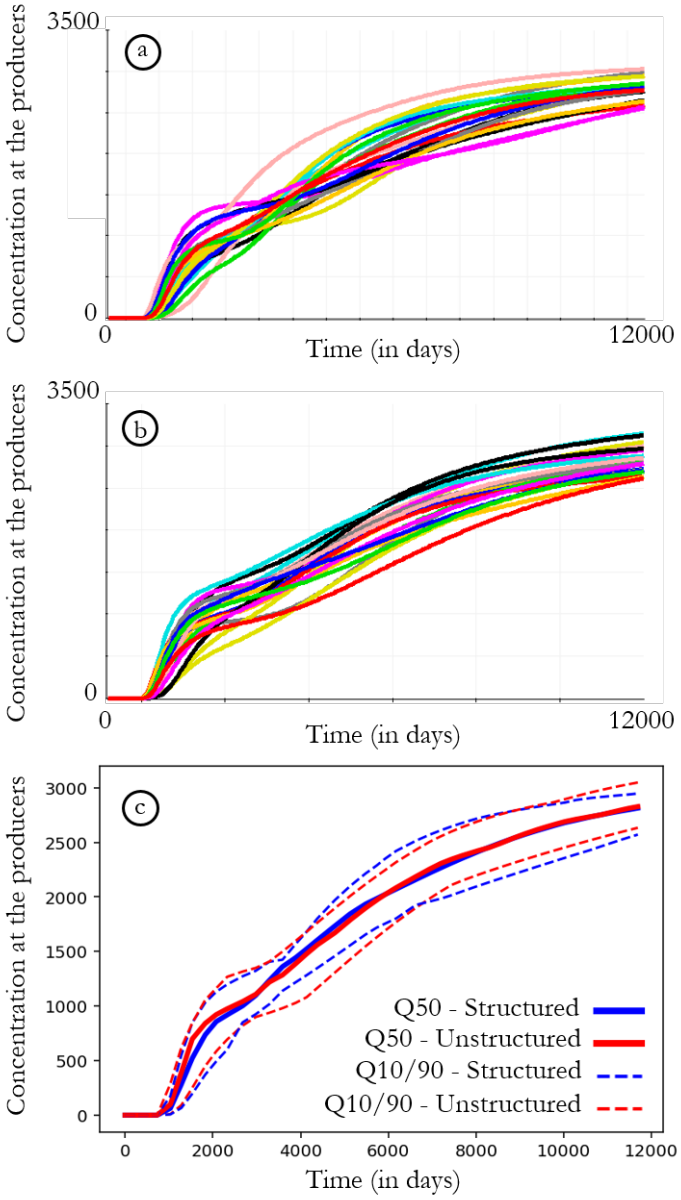

Figure 5.10: Concentration of tracer at all producers for twenty realizations on a) the fine structured reservoir and b) the unstructured reservoir. c) Quantiles of the twenty curves for structured (in blue) and unstructured (in red) reservoirs.

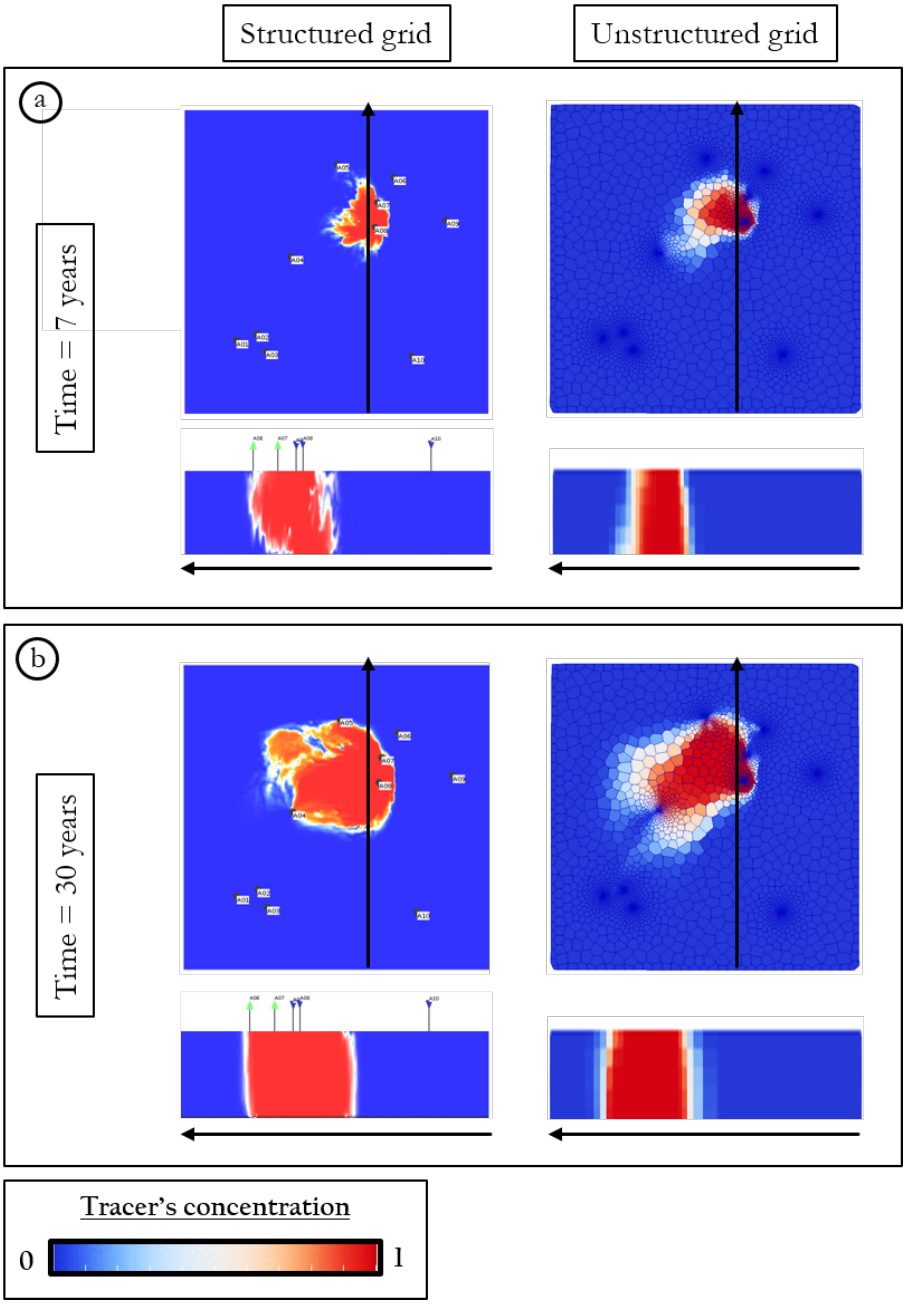

Figure 5.11: Visualization of the concentration of tracer in the structured and unstructured reservoirs for one realization at a) seven years of simulation and b) thirty years of simulation.

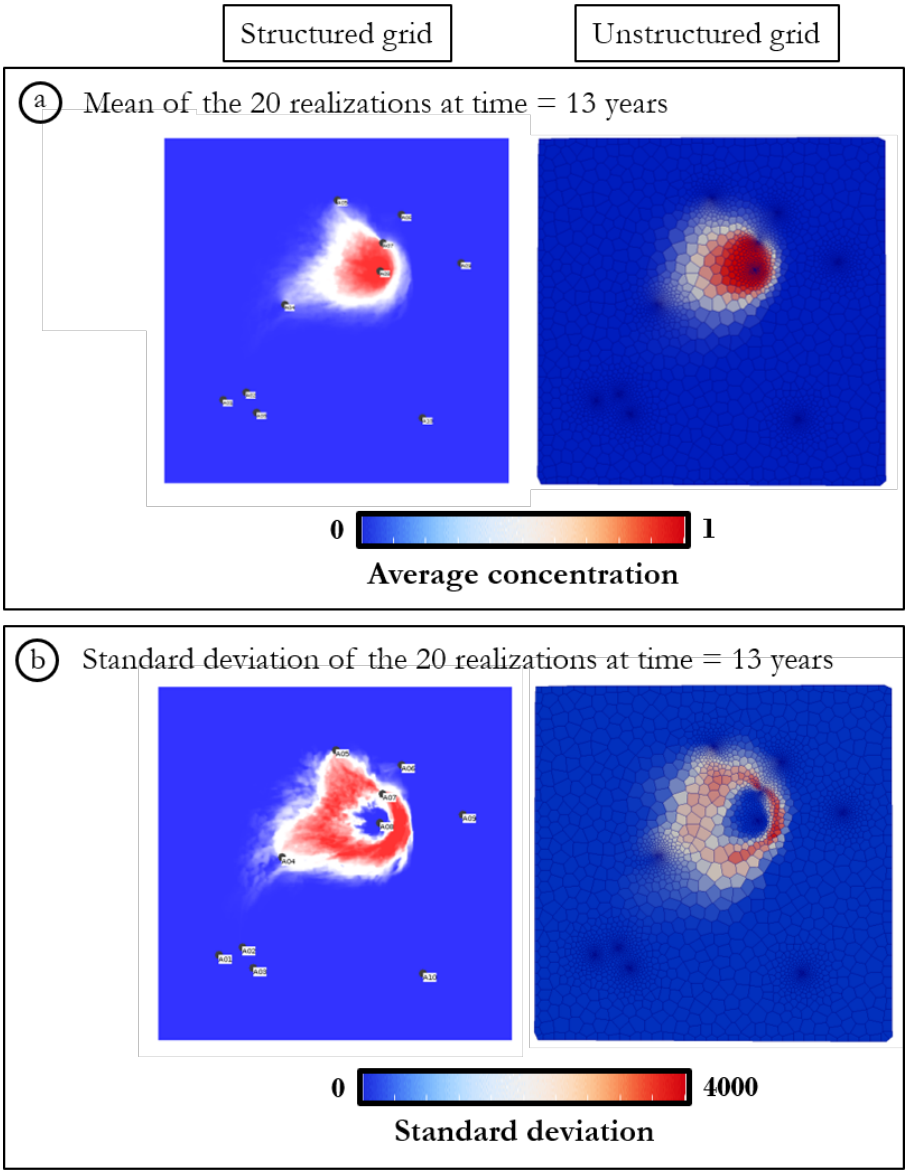

Figure 5.12: Visualization of a) the mean and b) the standard deviation of the twenty realizations of tracer's concentration evolution at time thirteen years in the structured and unstructured reservoirs.

5.2.3 Computation times

The use of an unstructured grid while accounting for the support effect, typically requires the use of geostatistical simulations on a fine structured grid, and numerical upscaling of the permeability (e.g. Aavatsmark et al., 1998; Prévost et al., 2005). For every realization, one needs to redo the upscaling. The methodology presented in this paper is different since it allows direct simulation of the permeability on the unstructured grid, but it shows improved efficiency for multi-realizations.

In particular, the computation time for the proposed method is not proportional to the number of cells in the unstructured grid. Indeed, the response surface computation is generally the most computationally demanding step, so the main factor influencing the time is the range of cell sizes covered. A grid presenting a larger range of cell sizes will require a broader response surface and therefore more experiments. In addition, the fine structured grid used to perform the experiments is defined from the minimum and maximum cell sizes. A higher difference between the two will require a larger fine grid, and hence longer upscaling times.

To evaluate the computation time, different tests have been made. The procedure has been applied on two grids with different characteristics: a small example with 18'250 cells varying from 3 to 90 meters horizontally and from 0.8 to 8 meters vertically, and a larger example with 2'031'995 cells varying from 6 to 2653 meters horizontally and from 3 to 60 meters vertically.

In the following, T_0 represents the time required to generate the response surfaces, $T_3 = T_1 + T_2$ represents the time required to simulate permeability values on points using STB (T_1) and perform either power averaging for unstructured grids or pressure solver upscaling for structured grids (T_2). The total simulation time T is:

$$T = T_0 + N\ T_3 \tag{5.1}$$

with N the number of realizations.

For a response surface with fifty experiments, using twenty Intel cores on a Linux machine, the computation times for our Java implementation are provided in Table 5.1. This table shows that the time required to perform one realization on the large grid is only doubled compared to the time required for the small grid, while the number of cells has been multiplied by a factor 100, showing the efficiency of the method for large grids.

	Small grid	Large grid
nb cells	18'250	2'031'995
T_0	22.4 min	35.4 min
T_3	11.3 s	7.5 min
Total (N=1)	22.4 min	43.0 min
Total (N=10)	24.3 min	111.1 min

Table 5.1: Computation times for two unstructured grids of different sizes. T_0 is the time to generate the response surfaces and ω properties on the grids, T_3 is the time to simulate permeability on points using STB and perform power averaging.

The computation time is also compared with the classical method (fine grid simulation followed by a pressure solver upscaling on a regular grid). The experiment is conducted as follows. The fine grid is the one presented in section 5.2.2, with 600x600x80 cells, the coarse grid has 60x60x5 cells (the upscaling ratios are 10x10x16). This coarse grid has 18'000 regular cells, which is close to the 18'250 cells of the unstructured grid.

For one realization, the proposed method takes three minutes more than the classical one (Table 5.2). However, as soon as one needs to perform at least two realizations, the proposed methodology is faster. Moreover, since the response surfaces are saved, it is almost immediate to simulate permeability fields when parameters have not changed, i.e. when the distribution, variogram and grid remain the same.

	Proposed method	Classical method
T_0	22.4 min	0
T_1	x	4.6 min
T_2	x	15.1 min
$T_3 = T_1 + T_2$	11.3s	19.8 min
Total (N=1)	22.4 min	19.8 min
Total (N=2)	22.8 min	39.5 min
Total (N=10)	24.3 min	198 min

Table 5.2: Computation times for the classical method (fine grid simulation and pressure solver upscaling) and the proposed method. T_0 = time to generate the response surfaces, T_1 is the time for STB simulation on points and T_2 is the time for either power averaging on the unstructured grid or pressure solver upscaling for the structured grid.

5.2.4 Synthetic case with unconfined conditions

The same test was performed, replacing the confined boundary conditions of the numerical upscaler by unconfined conditions, i.e. linearly-varying head conditions. By opening the boundaries, the fluid can flow around the heterogeneities. The equivalent permeabilities are larger and the response surfaces are very different (Fig. 5.13). For the horizontal permeabilities, ω_H becomes equal, or almost, to one (corresponding to the arithmetic mean) for the entire parameter space. For the vertical direction, the response surface presents similar variations to the one with confined conditions, although it globally shows higher values of ω_V with unconfined conditions.

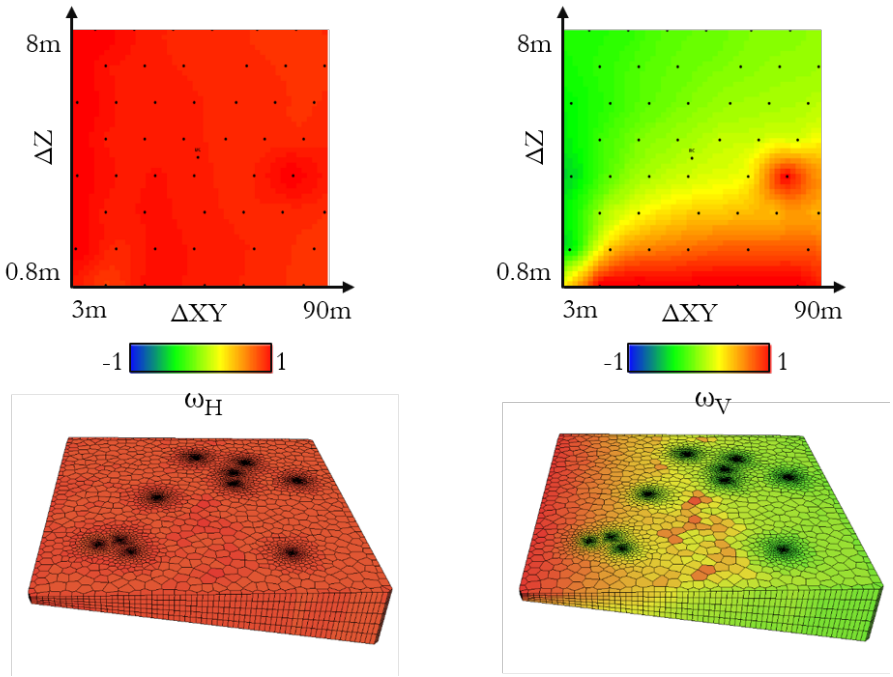

Figure 5.13: (Top) Surfaces of response for ω_H and ω_V computed with unconfined boundary conditions. (Bottom) associated ω properties mapped on the unstructured grid.

The porosity field has not changed as compared to the confined case. Permeability is simulated accounting for a linear correlation coefficient of 0.8 with porosity. As observed on Figure 5.14a, the permeability fields present the same structures as with the confined boundary conditions,

but with higher values. On the crossplots (Fig. 5.14b), the values for unconfined conditions are superior to the ones for confined conditions, with a maximum difference of 400mD. On the contrary of the results for confined conditions (Section 5.2.1), the values of K_H are always superior or equal to the ones of K_V.

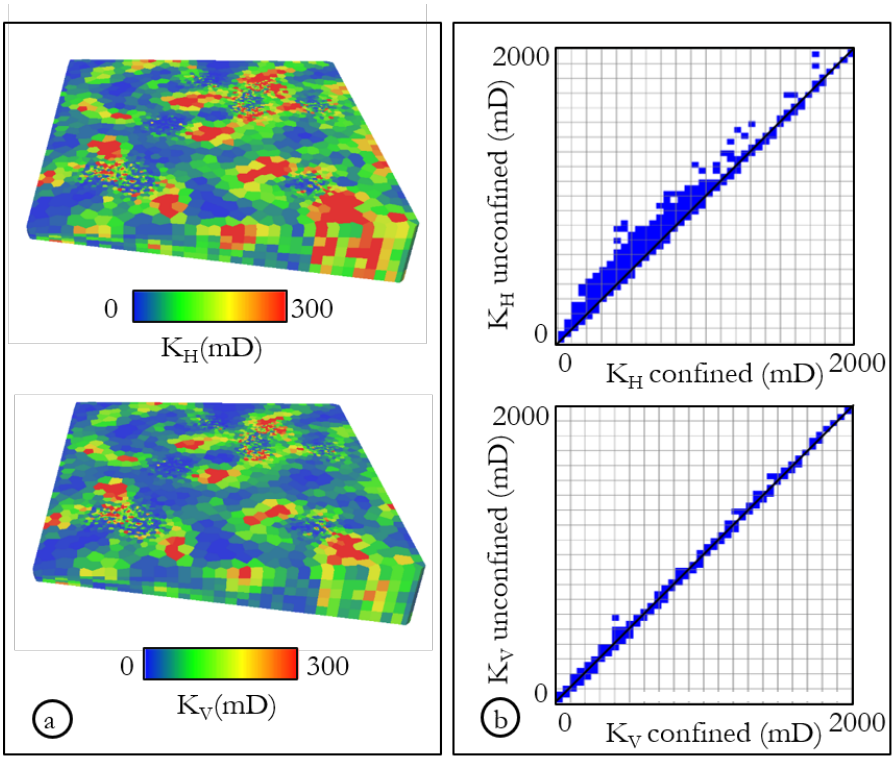

Figure 5.14: a) permeability, horizontal and vertical, simulated with unconfined conditions for the surface of response generation. b) Crossplot to compare previous results with confined conditions to the ones for unconfined boundary conditions.

These results demonstrate the dependence of numerical upscaling to boundary conditions. Although the methodology is applicable for confined and unconfined conditions, it is important to choose carefully which one to use, without forgetting that there are other conditions possible such as periodic conditions or extended local upscaling methods. Indeed, we have just seen that it affects the final permeability fields, especially for horizontal permeability. Confined, or permeameter, boundary conditions correspond to the flow conditions applied when

measuring permeability on samples in the laboratory. In the oil and gas industry, however, linearly-varying head, or unconfined, conditions are considered more realistic even if they may overestimate the permeabilities. The tool that we developed can be applied with both types of boundary conditions, and could be easily extended to other numerical upscaler. A more extensive study should be conducted to determine which boundary conditions provides more reliable results in general at the scale of the reservoir, but this aspect was considered to fall out of the scope of this PhD due to time limitations. In the rest of the work, surfaces of response will be computed usually with confined conditions, because they present more variations which gives more material to study. The real case study will be performed with unconfined conditions, in order to be as realistic as possible.

Chapter 6

Extension of the method for binary media

One main factor influencing the variations of ω, apart from the cell sizes as studied in the previous chapters, is the proportion of different facies or lithologies inside each cell. It has to be considered not only in terms of proportions, but also in terms of variograms, which controls the organization of the facies in the cells. In this chapter, an extension of the method for binary media is presented. This is a first step toward a multi-facies approach. Note that the medium considered in this chapter is not simply a binary medium with two lithologies and one constant mean permeability for each lithology as studied earlier for example by Desbarats (1992) and others, but a mixture of two lithologies displaying each some internal variability described using a Gaussian random field approach. The binary medium considered here is therefore a hierarchical mixture of two Gaussian random fields.

6.1 Target vs. simulated proportions

Taking into account proportions in the determination of ω requires to define precisely which proportions we are using. We distinguish the "target" and "simulated" proportions.

The target proportions are the proportions of each facies given as input in the geostatistical simulation of the facies. When using the Pluri-Gaussian Simulation or Truncated Gaussian Simulation techniques, the target proportions will be the ones given in the truncation diagram (Armstrong et al., 2011; Chilès and Delfiner, 2012). If the simulation is performed on an unstructured grid (Gross and Boucher, 2015; Biver

et al., 2019), the result will be a proportion for each facies in every cell of the grid. For each facies, the mean of these proportions on the whole grid should be equal to the target proportion. The proportions inside each cell, however, are different. We will call them the simulated proportions. Their variability and values are strongly dependent on the size of the cells. Indeed, the cells smaller than the facies variogram range will have proportion values varying from 0 to 1, while the largest cells will have simulated proportions close to the target proportions. Moreover, using the spectral turning bands technique, the cells containing only one integration point for the facies simulation will have simulated proportion values of either 0 or 1.

It is important to understand the influence that these different types of proportions have on the determination of ω. In Chapter 3, the influence of proportions has been tested with experiments, but we did not differentiate between target and a simulated proportions. A finer analysis of these influences has therefore been performed through numerical experiments. On a grid of 8x8x16 cells of 10x10x1 meters, we consider eight blocks of 40x40x8 meters (Fig. 6.1).

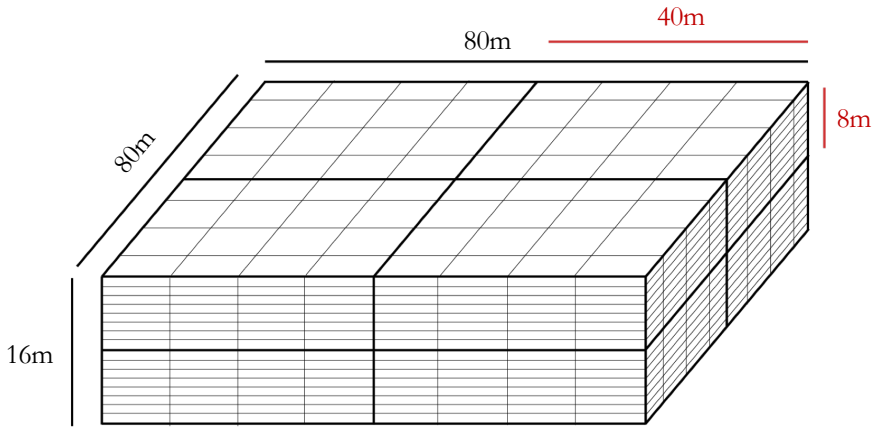

Figure 6.1: Grid used to perform the experiments on target and simulated proportions. The grid is divided in 8 blocks of 40x40x8 meters.

We simulate on this grid a thousand facies fields with target proportions noted *Ptarget*, the variogram having two Gaussian structures of equal contributions with ranges of 50x50x5 meters and 500x500x30 meters. Subsequently, we simulate a thousand permeability fields, consistent with the facies fields, using Spectral Turning Bands in structured

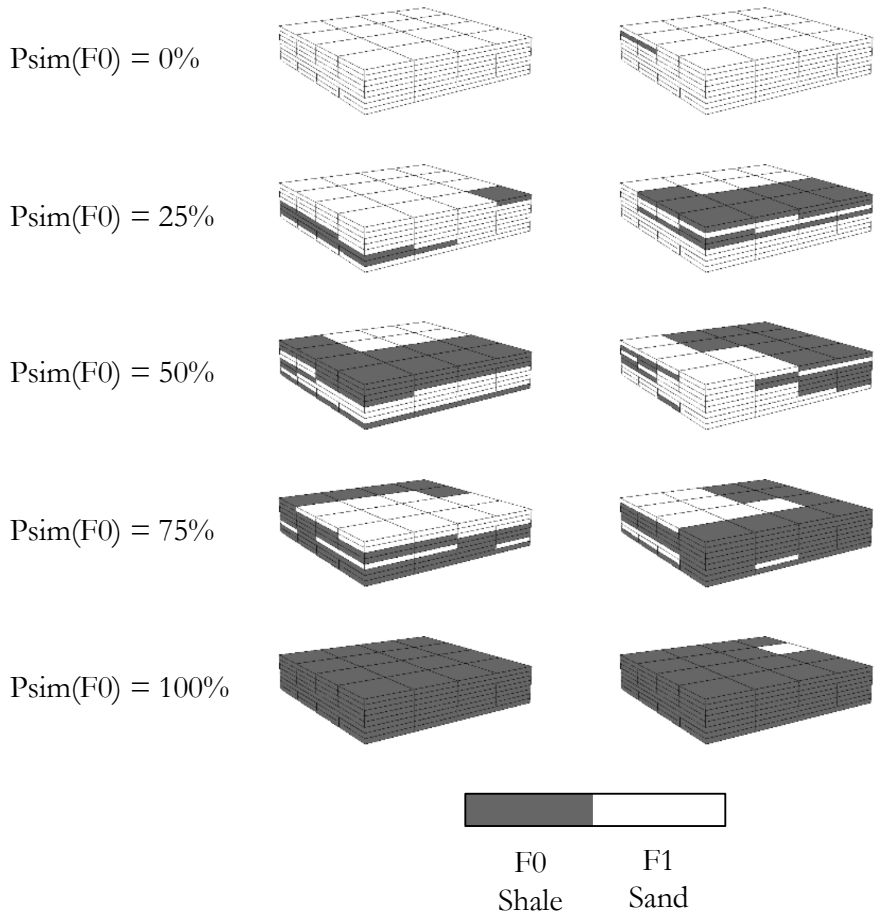

Figure 6.2: Two examples of blocks of 40x40x8 meters sorted by their simulated proportion of shale, with a target proportion of shales of 0.5. In reality, the majority of the blocks have a P_{sim} of 0.5.

mode, i.e. with one integration point per cell. Facies $F0$ is assimilated to shale and has a lognormal permeability distribution of mean 1.2 mD and standard deviation 0.45 mD. Facies $F1$ is composed of sand and has a lognormal permeability distribution of mean 120 mD and standard deviation 45 mD. The variogram for permeability has two Gaussian structures of equal contributions with ranges of 25x25x1 meters and 250x250x10 meters. These 1000 facies and permeability fields give 8000 simulated blocks of 40x40x8 meters. On one side, for each block, we calculate the simulated proportion $Psim$ of facies $F0$ and $F1$. On

the other side, the permeability inside each block is upscaled using a pressure solver, giving a K_{ref}. We sort the blocks and their associated K_{ref} in groups depending on their proportion of shale $Psim(F0)$, with a precision of 1%. An example of blocks sorted by their proportion of shale is given in Figure 6.2.

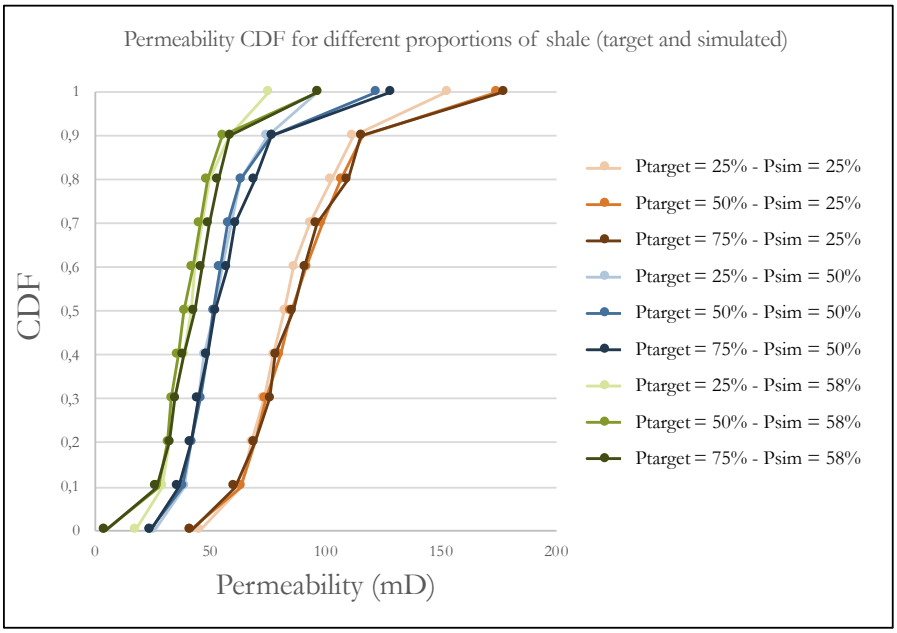

Figure 6.3: CDF of the K_{ref} distributions for different $Ptarget(F0)$ and $Psim(F0)$. The simulated proportions have an influence on the distribution of K_{ref}, while the target proportions have little or no influence.

Then, we select the groups that contain more than 100 blocks, each group having a distribution of K_{ref}. The experiment has been performed thrice for $Ptarget(F0)$ of 0.25, 0.5 and 0.75. We present on Figure 6.3 the CDF of the K_{ref} distributions for groups of $Psim(F0)$ of 0.25, 0.5 and 0.58. The target proportions have no influence on the distribution of permeability while simulated proportions do.

In this chapter, we only consider stationary facies simulations, which means that the target proportions will not vary over the grid. However, an extension of the method for non-stationary simulations will be presented at the end of this work (Chapter 9). We also recall that the following workflow is valid for binary media only.

6.2 Modification of the method

Only some minor modifications of the method are required to account for the facies proportions within the existing workflow. The general workflow including the additional steps are illustrated in Figure 6.4 and is explained rapidly in this section to introduce the approach.

The initial step of the workflow remains unchanged. This includes the computation of the size and aspect ratio of each cell of the unstructured grid (Fig. 6.4a).

In the second step, a metamodel of ω (extension of the response surface but in 3D) is estimated using numerical experiments. It takes into account cell geometry and simulated proportions of the facies inside each cell. To define the metamodel, we select a set of representative cell dimensions for which we perform the numerical experiments (since it is impossible to perform them for every cell geometry). Then, inside each experiment, a sorting step is added to create simulated proportions groups. This sorting step allows adding points along the proportion axis in the parameter space, resulting in a metamodel with more dimensions (Fig. 6.4b). This metamodel needs only to be created once at the beginning of the procedure.

Then, for every realization, several points are placed inside each cell of the unstructured grid. The facies are simulated on the points (Fig. 6.4c), and the permeability is simulated for each point with the Spectral Turning Bands approach using the statistics of the corresponding facies (Fig. 6.4d). The power averaging technique is then applied using the value of ω derived from the metamodel to obtain the equivalent permeability of the cell (Fig. 6.4e).

In the following subsections, we provide a detailed explanation of the new steps and briefly recall the steps of the method that have not changed, starting with the unstructured cells characterization.

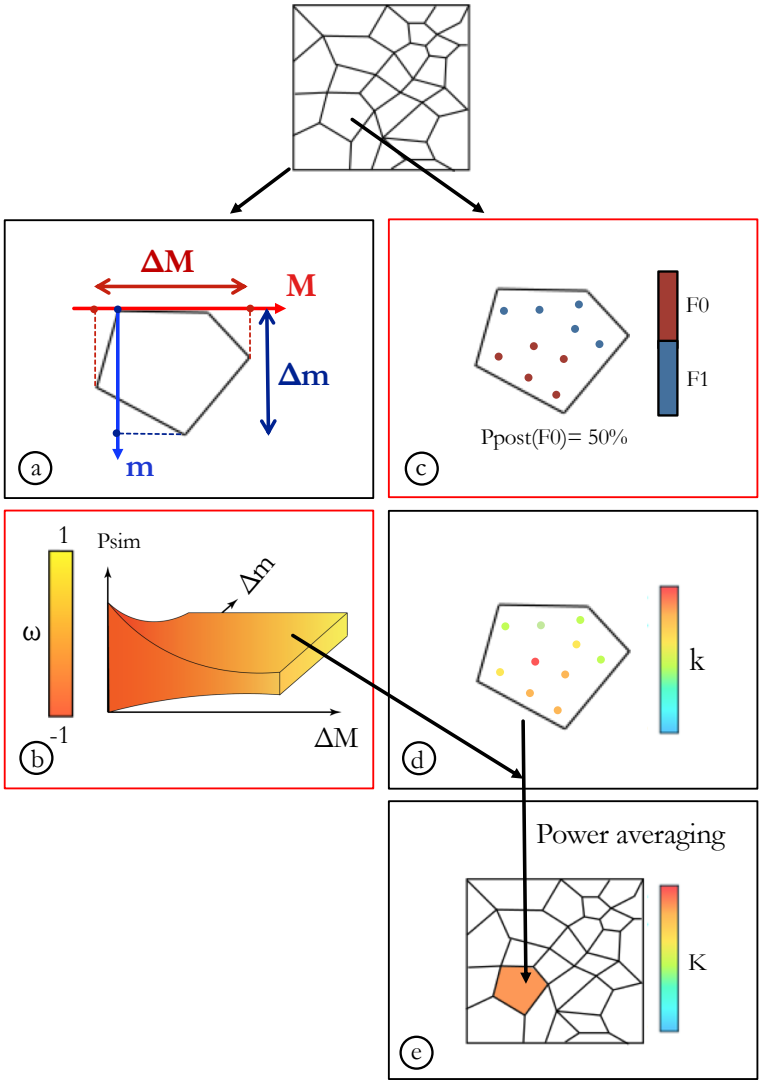

Figure 6.4: General workflow for the direct simulation of permeability on binary media (changed steps appear in red). For each unstructured cell, a) we find equivalent dimensions. b) We use these dimensions and simulated facies proportions to constrain a response metamodel of ω calibrated through upscaling experiments. Then, we fill the cells with several integration points and simulate c) facies on them and d) coherent permeability. Finally, e) we apply power averaging using the ω estimated in step b).

6.2.1 Characterizing the unstructured cells

This preliminary step has not changed and allows estimating the geometries of the unstructured cells (for detailed version, refer to section 4.1). We recall that we consider two separate sets of axes: the XYZ space is characterized by the orientation of the unstructured grid and the Mmt space is defined by the variogram anisotropy axes. It is in this depositional space, Mmt, that unstructured cell sizes are defined.

To define the cell sizes, vertices projections allow calculating a horizontal aspect ratio H along the Mm axes. For each unstructured cell, an equivalent regular hexahedral cell is defined through a simple system of equations, so that the volume of the regular cell V_r is equal to the volume of the unstructured cell V_u and that both cells have the same aspect ratio H and thicknesses.

6.2.2 Generating the metamodels

The main changes in the method occur during the generation of the response metamodel. However, the global workflow stays identical: using numerical experiments, ω is estimated in a finite number of points of the parameters space. A kriging is then applied to obtain ω for every cell geometry and proportions of facies.

Defining the parameter space

For the binary media, we consider two parameter spaces.

The initial parameters space is identical to the one used in the case without facies. It has axes regarding the cell sizes only. We recall that the dimension D of this parameter space depends on the type of unstructured grid, more details can be found in Section 4.2.1.

The second, or final, parameter space is the one used for estimating an ω for each unstructured cell. It has $D + 1$ dimensions: it has all the axes of the initial space, representing the cells geometry, and one additional axis for the simulated proportion of one facies. Indeed, in a binary media, as the proportions of facies sum to one, if a facies simulated proportion p_0 is known, the proportion of the other one is also known and is equal to $1 - p_0$. It is then unnecessary to have an axis for both proportions of facies.

For each of the D dimensions, the minimum and maximum of the sizes of the equivalent rectangular cells are computed to limit the ranges of possible cell sizes. For the proportion axis, the range is taken by

default between 0 and 1, because these values are always reached for the really small cells.

To obtain the metamodel, we choose N points in the initial parameter space following the procedure explained in Section 4.2.1 (Fig. 6.5a). The step to add points along the simulated proportion axis, allowing to define the metamodel in the final parameter space, is included in the experiments explained bellow (Fig. 6.5b).

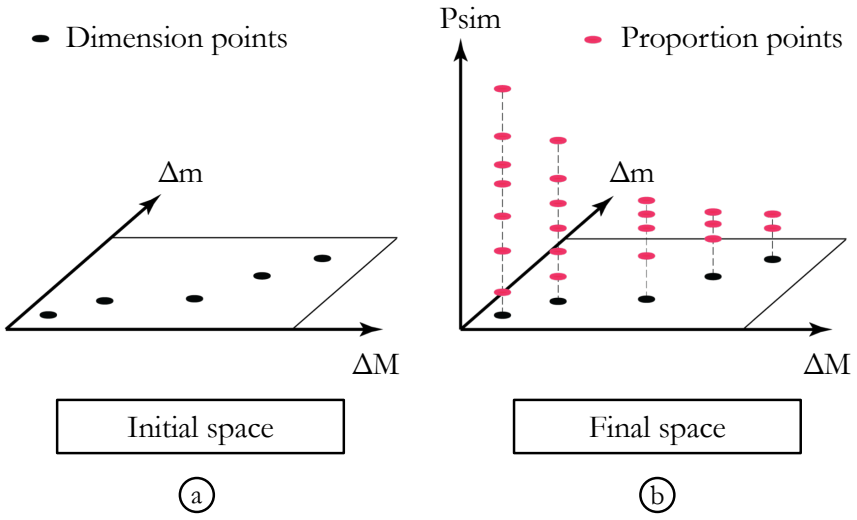

Figure 6.5: a) Initial parameter space taking into account only cell dimensions. b) Final parameter space with additional points along the simulated proportion axis.

Performing the experiments

The general process to perform the experiments is given in Figure 6.6. A value of ω has to be estimated for each cell size defined by the coordinates of the N points of the parameter space, but also for a set of different simulated proportions of facies: for each point having D coordinates representing cell sizes, e.g., ΔM_r^{exp}, Δm_r^{exp} and Δt_r^{exp} if $D = 3$, we use a fine regular grid aligned with the Mmt axes to simulate several realizations of facies maps and their associated fine-scale permeability. These fine values are then upscaled with the pressure solver using an upscaling ratio corresponding to the coordinates of the point treated, i.e. we create upscaled blocks of the size of the equivalent hexahedron of interest. These upscaled blocks are then sorted according to

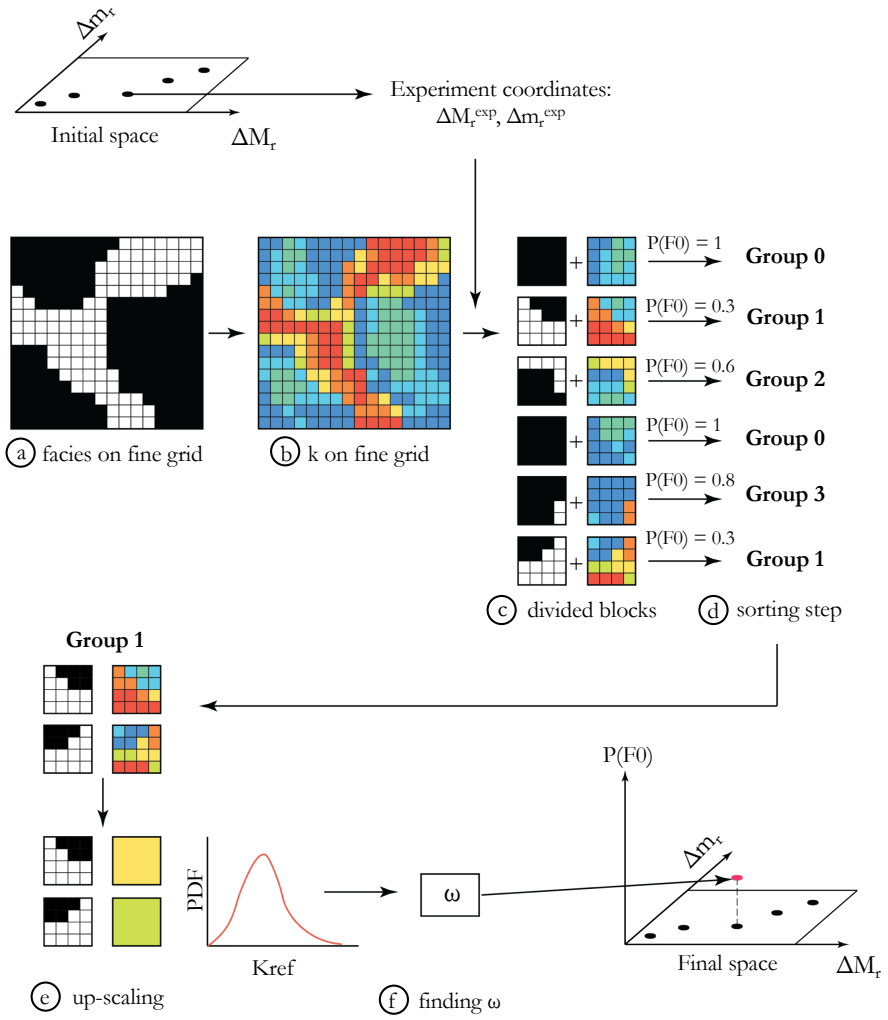

Figure 6.6: a) Simulation of facies on the fine grid. b) Simulation of a coherent fine grid permeability. c) Division in blocks of the size of the experiment coordinates. d) Sorting of the blocks by simulated proportion of facies F0 (in black). e) For the group 1, the fine grid permeability of blocks is upscaled using a pressure solver, it gives a distribution of reference permeability values. f) Finding the ω for this group by minimizing the global error between the reference and the power average. The ω for this group becomes a new point in the final space of parameters.

the simulated proportion of the chosen facies (between the two facies of the binary media), i.e. we create groups of blocks in which the simulated proportion of facies is similar within a chosen tolerance of 1%. The result is a distribution of reference upscaled permeability values for each group of blocks. We then determine the corresponding ω for which the power averaging distribution best fits the reference. This ω is the response for a point in the final parameter space. Its coordinates are the $D + 1$ dimensions representing the cell size and the simulated proportion.

Note that the fine grid for the fine-scale simulations is defined once, with the same procedure as in Section 4.2.2. The idea is to create a fine grid covering at least eight equivalent rectangular cells, 2 along each axis, no matter the size of the equivalent cell. An example of such a grid has been used in Section 6.1.

Then, each experiment is performed as follows:

- Using Spectral Turning Bands (Mantoglou and Wilson, 1982; Emery and Arroyo, 2017), a truncation diagram and a variogram, facies are simulated on the fine grid (Fig. 6.6a). This step is repeated R times with a different seed for random number generation.

- A fine-scale permeability k is simulated on the local grid for each of the R realizations of facies, with a distribution and variogram corresponding to each facies (Fig. 6.6b).

- On the fine grid, blocks are defined using cell's sizes corresponding to the current experiment (Fig. 6.6c).

- The blocks are sorted in groups according to the simulated proportion (Fig. 6.6d): we put together the blocks having the same simulated proportion (with a tolerance of 1%). Every group that contains more than a hundred blocks is kept, a hundred being the number of values considered statistically sufficient to calibrate an ω. Each of these groups will become a point in the final metamodel parameter space.

- For each retained group, the fine-scale permeability of each block is upscaled using a pressure solver, giving reference permeabilities K_M^{ref}, K_m^{ref} and K_t^{ref} (Fig. 6.6e). It gives a distribution of K^{ref} values in each direction and for each simulated proportion group.

- For each point of the final parameter space, i.e. for each group, the values of ω_M, ω_m and ω_t are determined by minimizing the global error between K^{ref} and the power average K^{eq}, i.e. minimizing the sum of the error for the n upscaled blocks (Fig. 6.6f):

$$\sum_{block=1}^{n} \| \log\left(K_{block}^{ref}\right) - \log\left(K_{block}^{eq}\right) \| \tag{6.1}$$

A discussion on the number R of fine-scale facies and permeability realizations is available in Section 4.2.2. We recall that it must be large enough so that the reference distribution K^{ref} has a statistically sufficient number of values to identify a robust value for ω.

The consistency of the unique ω approximation (see Section 3.2.3) in the case of binary media has been verified once again by comparing the CDF of permeability obtained with the pressure solver upscaler and with power averaging for different simulated proportions of shale. For a cell of size 25x25x2m, intermediate compared to the range of the variogram that is 25x25x2.5m, the CDF obtained are visible in Figure 6.7.

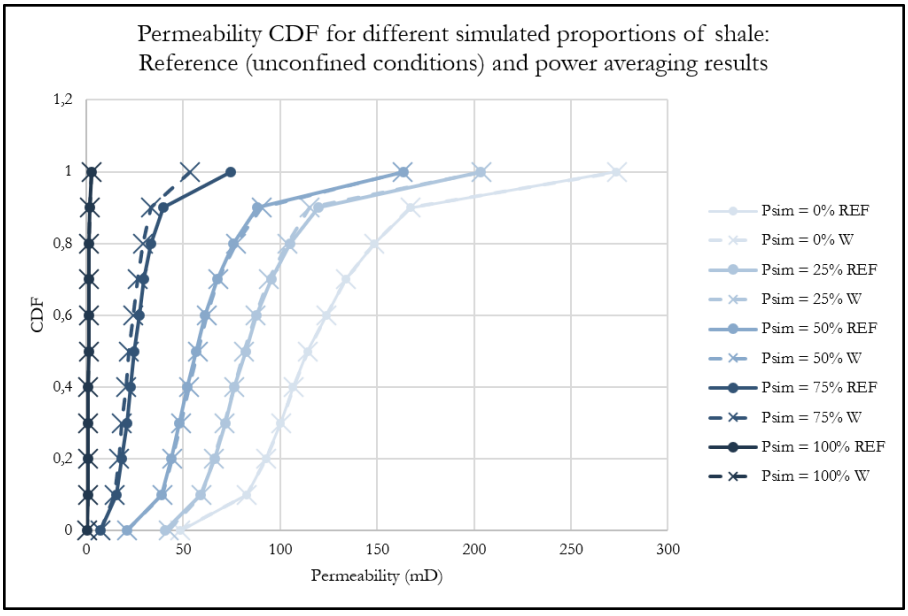

Figure 6.7: Comparison of the CDF of permeability obtained with the pressure solver upscaler (unconfined boundary conditions) and with power averaging for different simulated proportions of shale: $P_{sim} = 0, 0.25, 0.5, 0.75, 1$.

It shows that the power averaging reproduces well the reference distribution, even using the unique ω approximation on a problematic cell. It is important to note that the pressure solver boundary conditions were set to unconfined, but the case with confined conditions gives similar results, although less good for $Psim = 0.75$ (Figure 6.8).

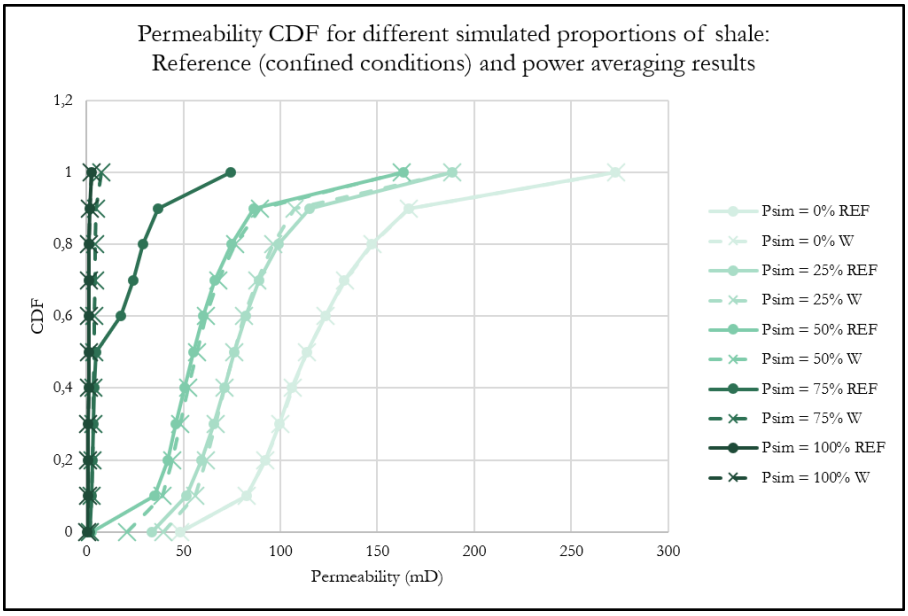

Figure 6.8: Comparison of the CDF of permeability obtained with the pressure solver upscaler (confined boundary conditions) and with power averaging for different simulated proportions of shale: $P_{sim} = 0, 0.25, 0.5, 0.75, 1$.

Kriging the metamodel

This step remains identical to the one described in Section 4.2.3: once all numerical experiments have been performed, an interpolation between the points of the parameter space is done using kriging (Fig. 6.9a), resulting in a metamodel for each direction M, m and t. As indicated above, the metamodels have one more input dimension for the facies proportion (Fig. 6.9b).

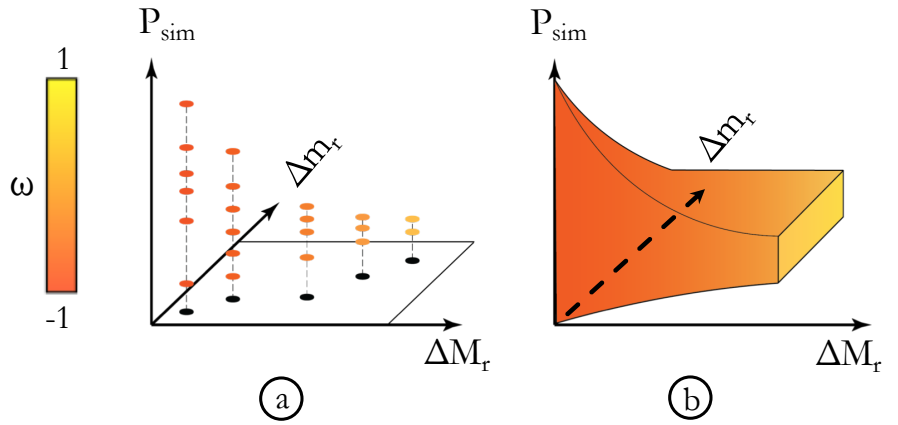

Figure 6.9: a) All experimental results are put in the parameters space. b) Kriging in 3D allows the generation of the metamodel of ω.

It is important to note that, for the binary media, only a part of the parameter space contains useful values for ω (Fig. 6.9b). Indeed, there are zones in the parameter space that cannot be explored. In very large cells, following support effect theory, the simulated proportion tends toward the target proportion. For example, if the target proportion is equal to 0.5, the simulated proportion will never reach 0 or 1 in the cells that are large compared to the correlation length of the facies. This implies that there are areas within the parameter space where it is useless to estimate ω.

6.2.3 Simulating the permeability values

This step is similar in principle to what was described earlier in Section 4.3. We simulate rapidly the values on the integration points using Spectral Turning Bands (STB) and average them using the estimated ω. However, due to the presence of the facies, the simulation has to be made in a precise order.

We start by generating the metamodel, following the steps given above (Fig. 6.10a). On the contrary of the methodology without facies, the ω properties on the grid are not computed yet. Indeed, to estimate the value of ω on the unstructured grid, we need to know first the simulated proportion in the cell.

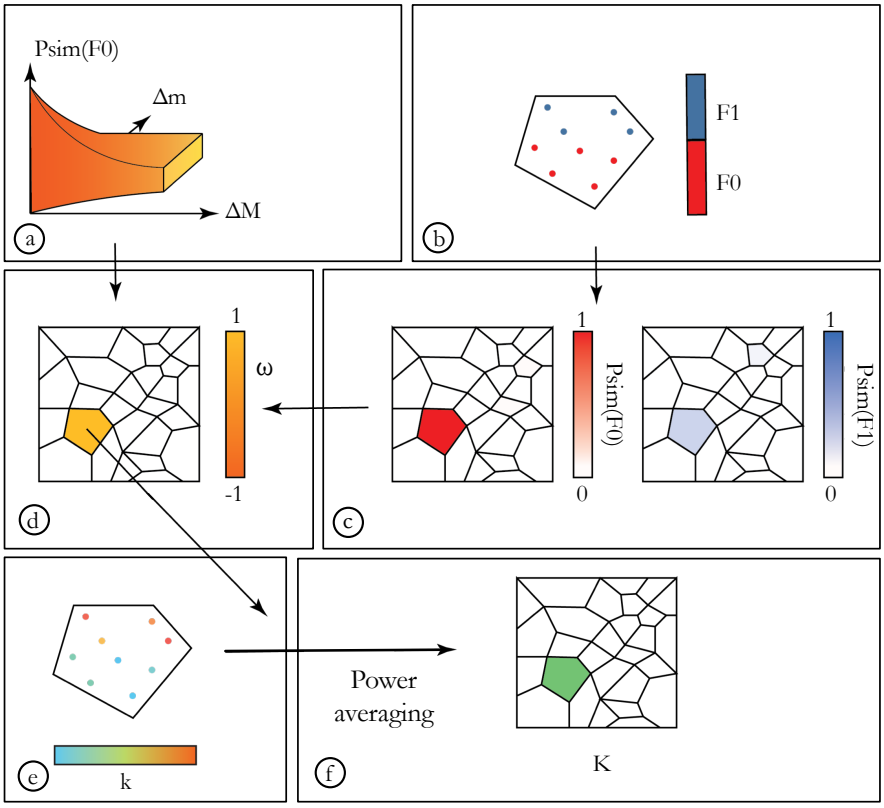

Figure 6.10: a) We generate the metamodel. b) One by one, each unstructured cell is filled with points, and facies are simulated on them. c) From these points, we calculate the proportion of facies inside the cell. d) With the metamodel and the newly calculated proportion, we compute an ω for the cell. e) Permeability is simulated on points using STB. f) We use power averaging, with the previously calculated ω, to obtain permeability on the unstructured cell.

One by one, each unstructured cell is filled with integration points using a fast generation of quasi-random Sobol' sequences with the method of Antonov and Saleev (1979). Facies are simulated on these points, with the same variogram and truncation diagram as the ones given for the generation of the metamodel (Fig. 6.10b).

These point simulated with facies allow the calculation of the simulated proportion of each facies inside the cell (Fig. 6.10c). From these proportions and the cell sizes, an ω is retrieved in the metamodel for the considered cell (Fig. 6.10d).

Then, for each point, permeability is simulated taking into account a variogram and a distribution corresponding to the facies that was simulated on this point (Fig. 6.10e). Finally, power averaging is performed using the ω found for the cell (Fig. 6.10f).

The process is applied to every cell, deleting the points of the previous cell and keeping only the cell value. At the end of the simulation, we obtain a property of simulated proportion for each facies, a map of dominant facies (the dominant facies in a cell being the one with the highest proportion), a property of ω, and a property of permeability. If the permeability is correlated to porosity, the simulation of porosity on points, depending on the facies, is performed between the simulation of facies and the simulation of permeability.

Chapter 7

Application of the approach to a synthetic case with two facies

After simulating permeability on a synthetic case, without facies, the methodology has been applied to the same synthetic case, but taking into account two facies. The results are coherent and will be illustrated in the following sections.

7.1 Simulations on the synthetic case

In this section, we illustrate the method with a synthetic but realistic example. The general model has not changed (Section 5.2.1): we consider a confined aquifer of 2km by 2km with negligible ambient flow. The external boundaries are assumed to be impermeable. The thickness of the aquifer is varying linearly from 40 meters in the eastern side to 4 meters in the western side. The 3D unstructured grid for this case is composed of 18,250 Voronoï cells with a volume between 25 m^3 and 50.10^3 m^3 (Fig. 7.1a). The grid is refined around ten wells.

In the following, we first describe the facies simulation, then the generation of ω and permeability simulation.

7.1.1 Facies simulation

The two facies considered for this synthetic case are a facies composed of shales, called F0, and a facies composed of sands, called F1.

The facies are obtained using a truncated Gaussian simulation technique (Armstrong et al., 2011). The parameters are the following. The variogram for the underlying latent Gaussian field has two Gaussian structures of equal contribution with ranges of 50x50x1.1 meters and 500x500x6.6 meters (Fig. 7.1b). For the same reasons as presented in Section 5.2.1, the vertical ranges for simulating on the unstructured grid, i.e. to simulate in UVT space, T being normalized, are 0.05[-] for the small structure and 0.3[-] for the big one. The target proportions and link between facies are represented using a simple truncation diagram visible on Figure 7.1c. For both facies, the target proportion is 0.5.

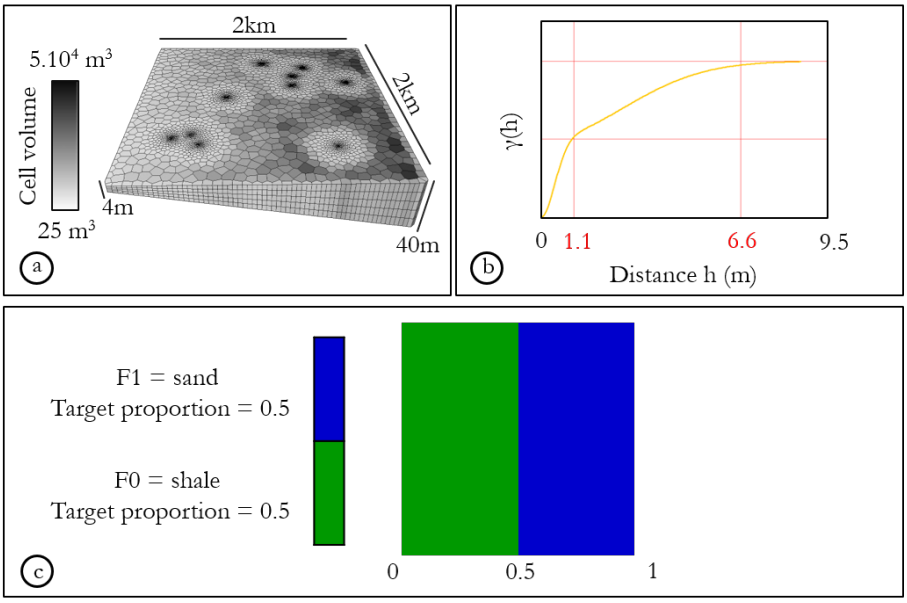

Figure 7.1: a) Grid for the synthetic case with cell volumes varying with a factor 2.10^3. b) Double structure vertical variogram used for the simulation of facies. c) Simple truncation diagram defining facies target proportions and the link between facies.

For each simulation, three properties are obtained on the unstructured grid using the spectral turning bands (STB) and the truncation diagram: a map of dominant facies (Fig. 7.2a), the simulated proportion of F0 (Fig. 7.2b) and the simulated proportion of F1 (Fig. 7.2c). The fine scale variability resulting from the small structure of the variogram is visible in the refined zones of the grid. Moreover, small cells, that

only have one integration point for STB simulation, have a simulated proportion of either 0 or 1.

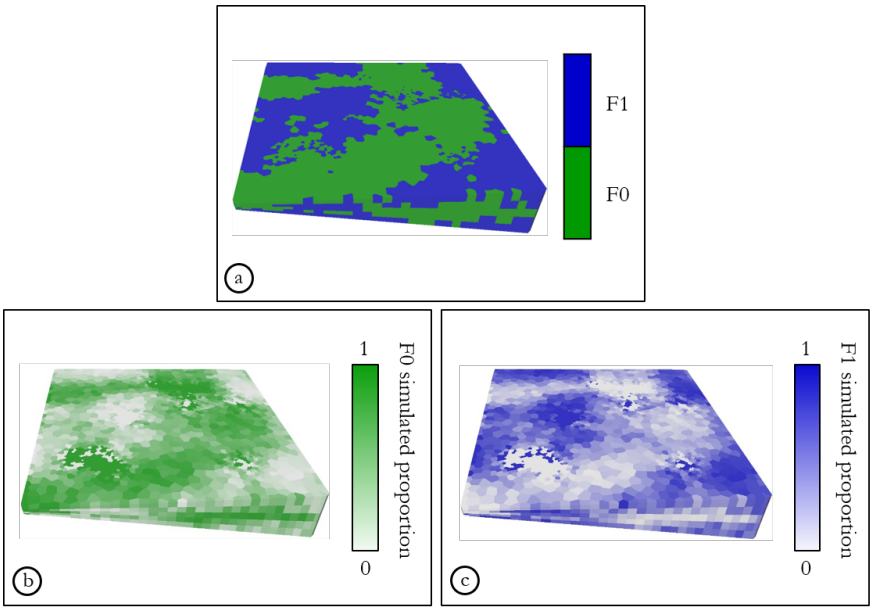

Figure 7.2: a) Map of dominant facies. b) simulated proportion of facies F0. c) simulated proportion of facies F1.

7.1.2 Permeability simulation

Within each facies, the variogram used for both porosity and permeability is the same. It has two Gaussian structures of equal contribution with ranges of 25x25x2.5 meters and 250x250x25 meters (vertical ranges of 0.114[-] and 1.14[-] for simulation in UVT space) (Fig. 7.3a). In facies F0, the porosity has a Beta distribution of max 0.1, mean 0.05 and standard deviation 0.02 (Fig. 7.3b) and the permeability distribution is lognormal with a mean of 1.2 mD and a standard deviation of 0.45 mD (Fig. 7.3c). In facies F1, the porosity has a Beta distribution of max 0.25, mean 0.2 and standard deviation 0.02 (Fig. 7.3d) and the permeability distribution is lognormal with a mean of 120 mD and a standard deviation of 46 mD (Fig. 7.3e). The boundary conditions for the upscaler in the experiments are of permeameter-type, i.e. no-flow conditions on the sides.

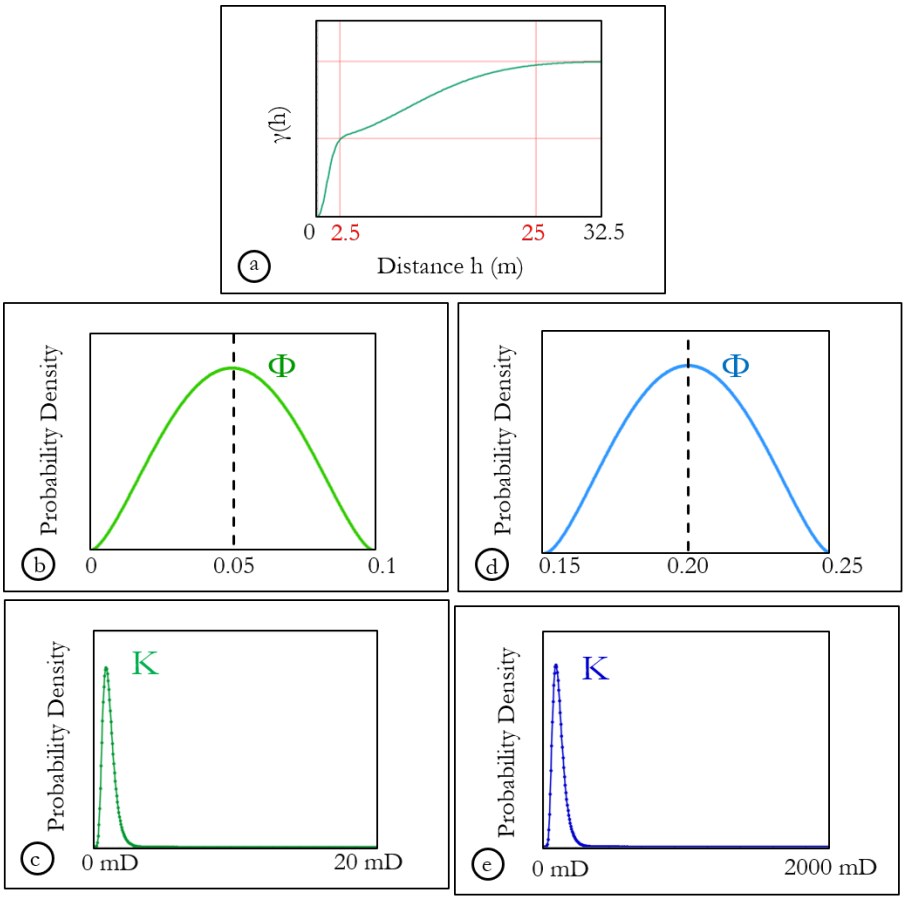

Figure 7.3: a) Vertical variogram for petrophysical variables. Distributions of b) porosity and c) permeability for facies F0. Distributions of d) porosity and e) permeability for facies F1.

X axis and Y axis being equivalent, only two response metamodels are presented hereafter: one for the horizontal exponent $\omega_H = \omega_X = \omega_Y$ and one for the vertical exponent ω_V. Each metamodel covers actually a cube, as presented on Figure 7.4 and 7.5. The three axes of the metamodels represent: the horizontal cell sizes ΔXY (taken as the mean of the cell sizes in X and Y), the vertical cell sizes ΔZ and the simulated proportion of facies F0 Psim(F0). In section 6.2.2, we noted that it is useless to estimate an ω in some places. Although these metamodels have the shape of a cube, there are zones that have been interpolated from no points. To illustrate this idea, the points from which the metamodels of response are interpolated are visible in Figure 7.6.

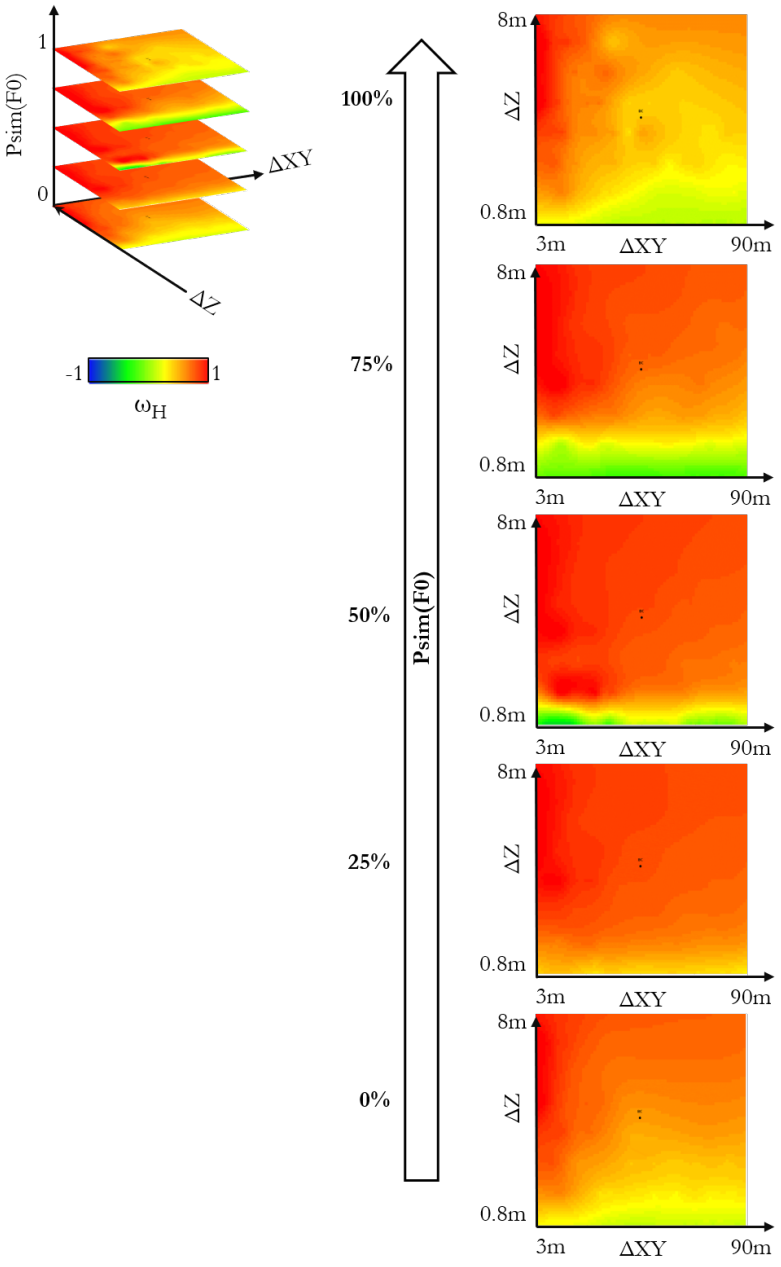

Figure 7.4: Metamodel of ω_H (top left), with surfaces for simulated proportions of facies F0: 0, 0.25, 0.5, 0.75 and 1.

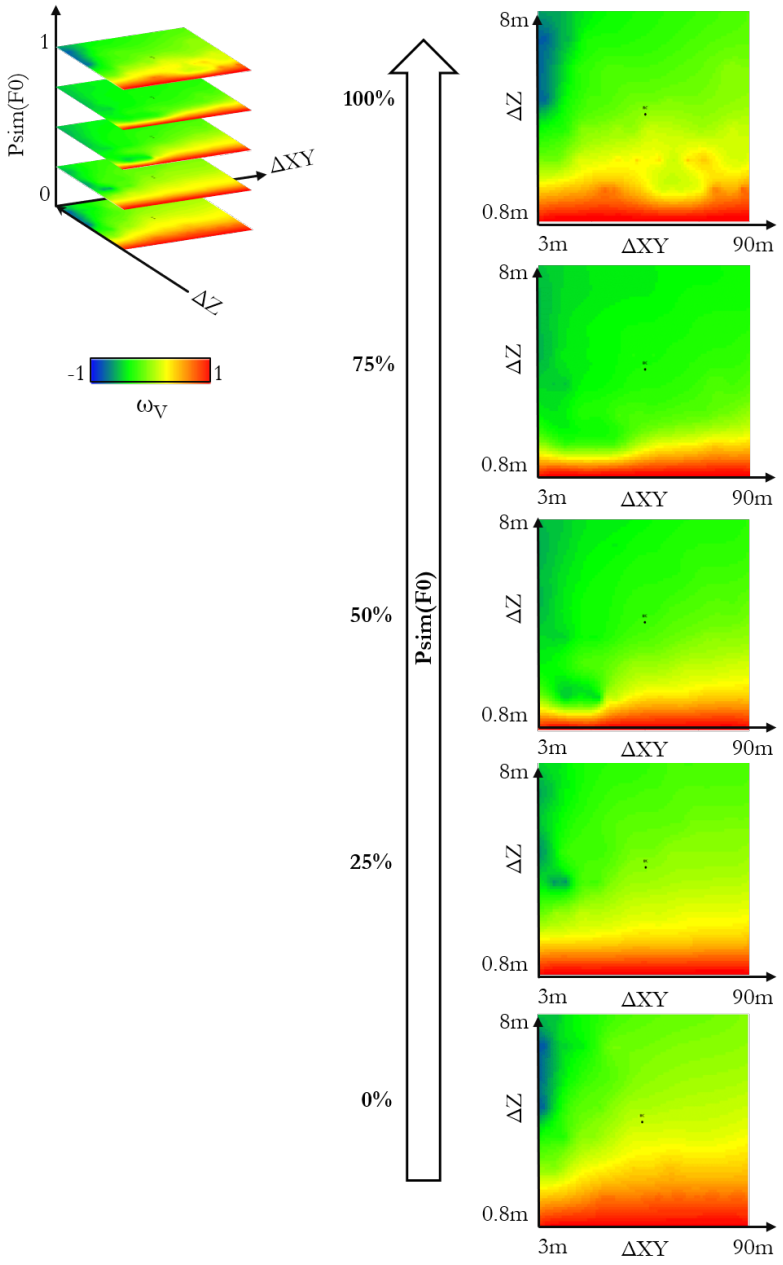

Figure 7.5: Metamodel of ω_V (top left), with surfaces for simulated proportions of facies F0: 0, 0.25, 0.5, 0.75 and 1.

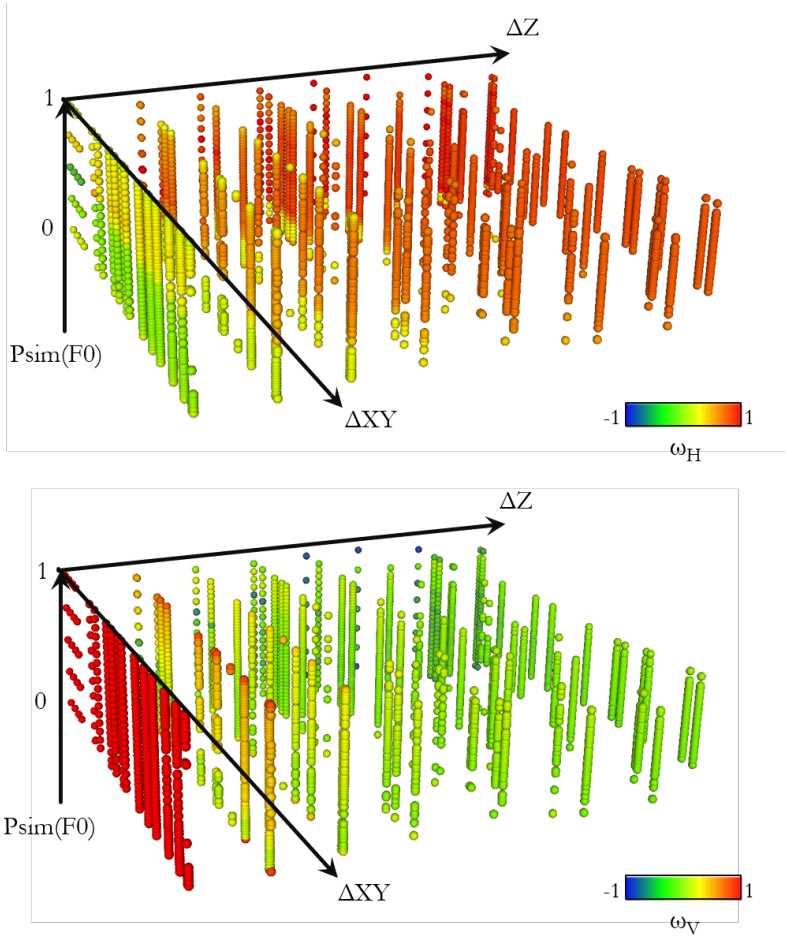

Figure 7.6: Points in the parameters space that allowed to generate the metamodels of response for ω_H (on top) and ω_V (at bottom). Columns of points are smaller on the right, which corresponds to large cells, and are vertically centered around the middle which is coherent with the target proportion 0.5.

A smooth variation of ω is observed, from -0.5 to 1 for ω_H and from -1 to 1 for ω_V. Surfaces of response, i.e. "slices" of the metamodels, for Psim(F0)=0% and 100% are equivalent which is coherent with the variations of ω depending on shale proportion presented in Section 3.2.2. The response surfaces for Psim(F0)=0% and 100% are less smooth compared to the single facies case. Indeed, there is no control on the number and the location of points that will be taken into account to compute

those surfaces, i.e., on the number of groups of blocks that will have a simulated proportion of 0 or 1. In the end, one ω is found for each cell of the unstructured grid (Fig. 7.7).

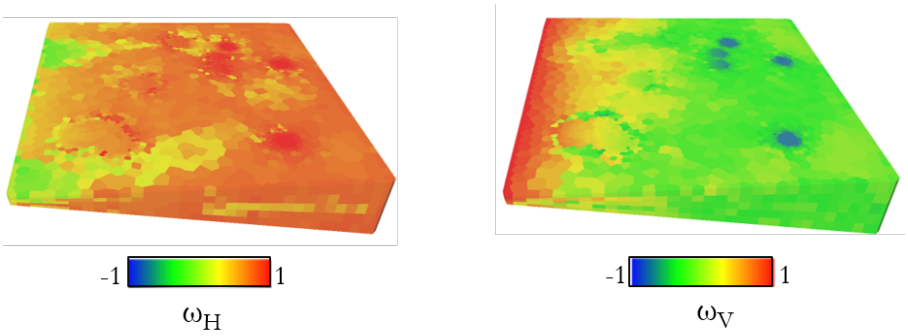

Figure 7.7: Properties of ω, horizontal and vertical, obtained on the grid from response metamodels.

The log of permeability is assumed to be correlated to point-support porosity with a correlation coefficient of 0.8, which is possible using Spectral Turning Bands. Porosity on the unstructured grid is obtained using the arithmetic mean (Fig. 7.8) and two permeability (H and V) are simulated using the power averaging formula and ω properties generated previously (Fig. 7.9a).

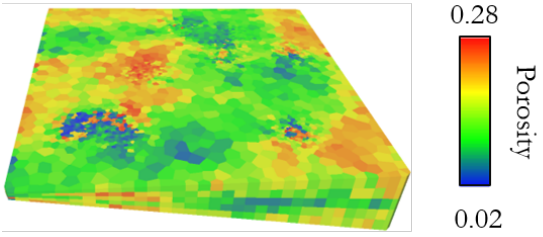

Figure 7.8: Porosity field on the toy example. Permeability will be correlated to this field with a factor 0.8.

K_H and K_V present more differences than on the case without facies, with K_V globally inferior to K_H. Figure 7.9b confirms that our permeability is guided by facies proportions, with two groups visible: one of low permeability for F0 and one of higher permeability for F1. The simulation using forty Intel cores took a total time of 139 minutes, with

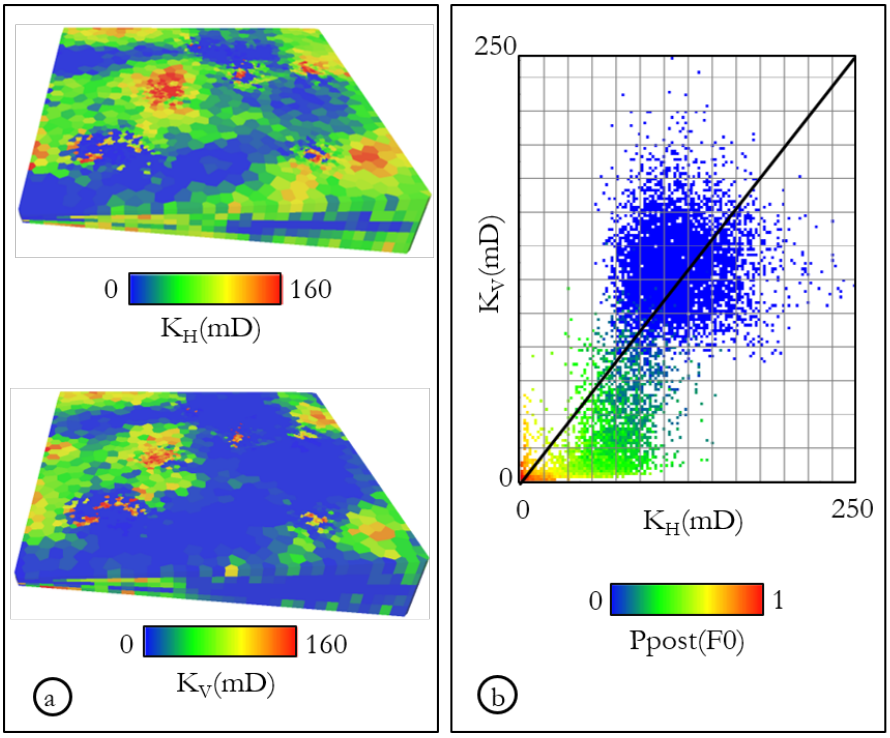

Figure 7.9: a) Vertical and horizontal permeability fields on the toy example. b) Cross-plot K_H vs. K_V, K_V being globally inferior to K_H.

138 minutes for the generation of the response metamodels and one minute for the simulation of permeability, porosity and permeability. The computation time is higher than the case without facies, because more experiments are necessary to cover the entire space of parameters. In addition, the number of realisations discussed in Section 4.2.2 is also higher, in order to have enough groups of facies with at least a hundred blocks to fit an ω.

7.1.3 Synthetic case with unconfined conditions

The same case, with the same parameters, is run with a change in the boundary conditions for the upscaler in the experiments. From permeameter-type conditions, i.e. no-flow conditions on the sides, we change to linearly-varying head conditions, also called unconfined conditions. As presented in Section 5.2.4, the response metamodels are highly different, especially for ω_H (Fig. 7.10). The ω_V metamodels are globally

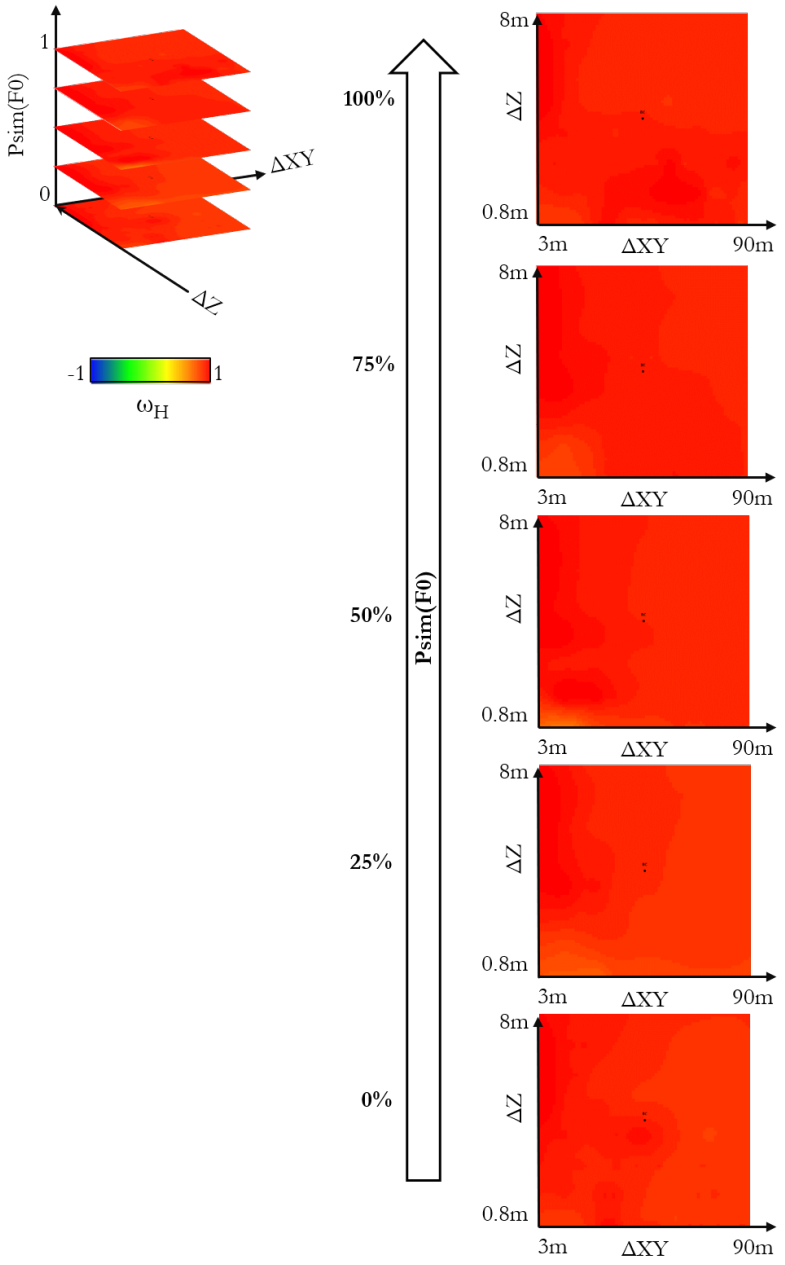

Figure 7.10: Metamodel of ω_H (top left), with surfaces for simulated proportions of facies F0: 0, 0.25, 0.5, 0.75 and 1, when the boundary conditions for the experiments are unconfined.

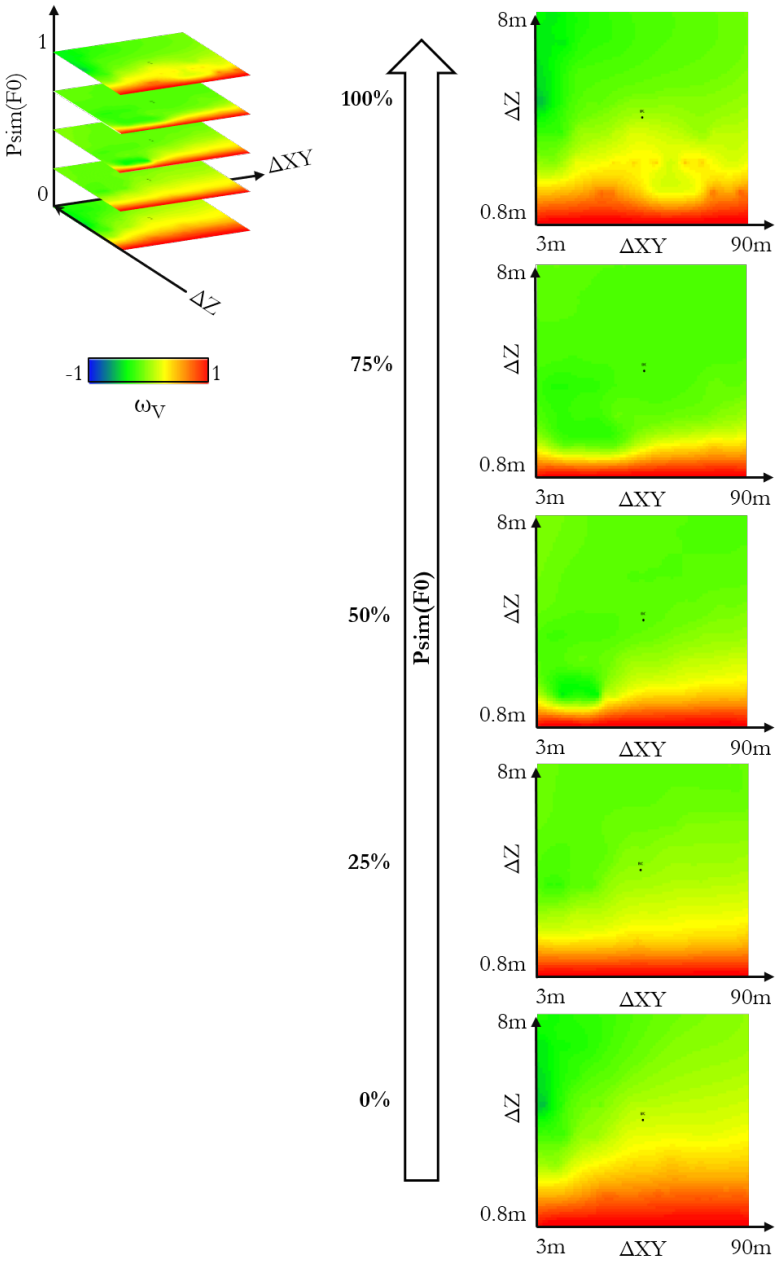

Figure 7.11: Metamodel of ω_V (top left), with surfaces for simulated proportions of facies F0: 0, 0.25, 0.5, 0.75 and 1, when the boundary conditions for the experiments are unconfined.

identical, although the values tend more towards the arithmetic mean than the harmonic one (Fig. 7.11).

The exponents ω are displayed on the grid in Figure 7.12. The porosity field has not changed from the previous case. Permeability is still correlated at point support to porosity, with a correlation coefficient of 0.8. Globally, the permeability properties are similar to the ones obtained for confined conditions (Fig. 7.13a). The values of horizontal permeability increase up to 50 mD compared to the previously simulated horizontal field (Fig. 7.13b top). It is consistent with the new aspect of the horizontal metamodel, that shows a globally higher ω_H. Vertical permeability remains quite close from the confined one, the ω_V metamodel having slightly changed (Fig. 7.13b bottom).

Once again, these results highlight the necessity of carefully choosing an upscaler, and the parameters associated. A change in the boundary conditions can lead to different metamodels of response.

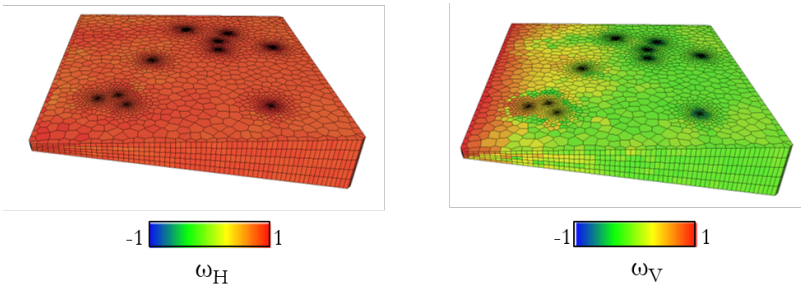

Figure 7.12: Properties of ω, horizontal and vertical, obtained on the grid from response metamodels with unconfined conditions.

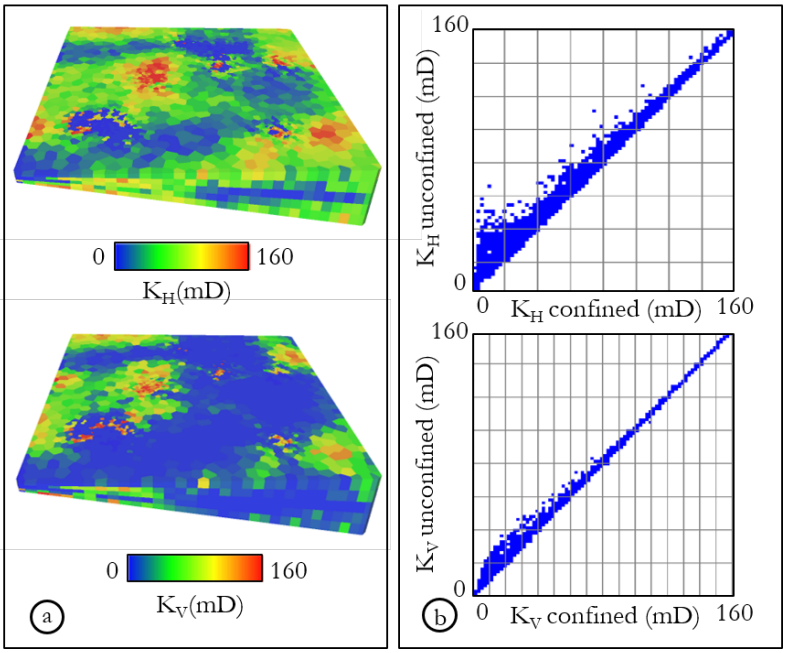

Figure 7.13: a) Vertical and horizontal permeability fields on the toy example, for unconfined conditions. b) Cross-plots for K_H confined vs. unconfined and K_V confined vs. unconfined.

Chapter 8

A real case study

The consistency of the method has been studied in Chapters 5 and 7. This chapter is dedicated to the applicability of the method to a real case study that we will call Field X. First, we will describe the field geology and economical interest. Then, we will apply the proposed method, starting with a simple simulation without taking facies into account, and following with a more complex permeability simulation with two facies.

8.1 Geological context for Field X

The field of interest is located in the Athabasca oil sands area, in Northern Alberta, Canada (Fig. 8.1). It is the largest oil sands area in the world, as the ensemble of oil sands deposits composed of Athabasca, Cold Lake and Peace River oil sands, represent 40% of the world's resources of bitumen (Hein et al., 2001; Hein, 2017).

Athabasca area is part of the Western Canada sedimentary basin, on its updip margin against the Canadian shield. Most of the bitumen resources of the area are contained in the sediments of the Lower Cretaceous McMurray formation. This formation unconformably overlies older sediments of upper and middle Devonian, the schematic succession of the formations of interest is represented on Figure 8.2. The nomenclature for the McMurray formation has evolved through time. Primarily, the McMurray formation was divided in three units: Lower, Middle and Upper. Later, studies at a wider, regional, scale have shown that Middle and Upper McMurray can be considered as one single unit. In the oil and gas industry, however, the studies are conducted at a smaller scale, which is the field scale, and as a consequence the Middle

and Upper remain separated (Hein and Cotterill, 2006). An extensive description of the McMurray-Wabiskaw formations is available in Hein et al. (2006), and a brief summary is made hereafter:

Lower McMurray unit: it is composed of channels formed in fluvial, early transgressive conditions. The sediments contain a majority of medium-grained sands, in massive layers, with the rare presence of beds of carbonaceous mudstone. This unit contains mostly water, or is poorly saturated with bitumen.

Middle McMurray unit: it is a succession of fluvial, estuarine, point bar and abandonment fill deposits. Typically, it is composed of massive, fine to medium-grained sands at the base, topped with inclined beds of sands grading up into units of laminated light grey mudstone and sands. Common mudstone clast breccias are interbedded within the sands and mudstone units. Middle McMurray is usually well saturated with bitumen.

Upper McMurray unit: it is a succession of tidal channel, tidal flat, brackish bay and transgressive back-barrier deposits. The formation is composed of very fine-grained sands, organized in thin horizontal beds, capped by coarsening-upward units of mudstone. The sands are usually saturated with bitumen. The whole Middle/Upper McMurray is the result from deposition and reworking during early and middle transgressive phases.

Wabiskaw member: this member of the Clearwater formation is a succession of three units: The Wabiskaw D Incised Valley Fill deposits (DVF), the Wabiskaw D Shale deposits and the Wabiskaw C deposits. DVF and marine shales were deposited during maximum flooding of the McMurray-Wabiskaw transgression. The Wabiskaw C is the result of initial regressive phases. DVF deposits are a mixed sand-and-shale succession in the majority of cases. Typically, they contain 20 to 40% of shale component. Wabiskaw D unit is composed of shale to sandy-shale deposits, with an immature litharenite sand component and a dark fissile shale component. Wabiskaw C deposits contain more than 50% of glauconitic sandstones, interbedded with a light green-grey sandy mudstone. The Wabiskaw member is saturated with bitumen in some areas.

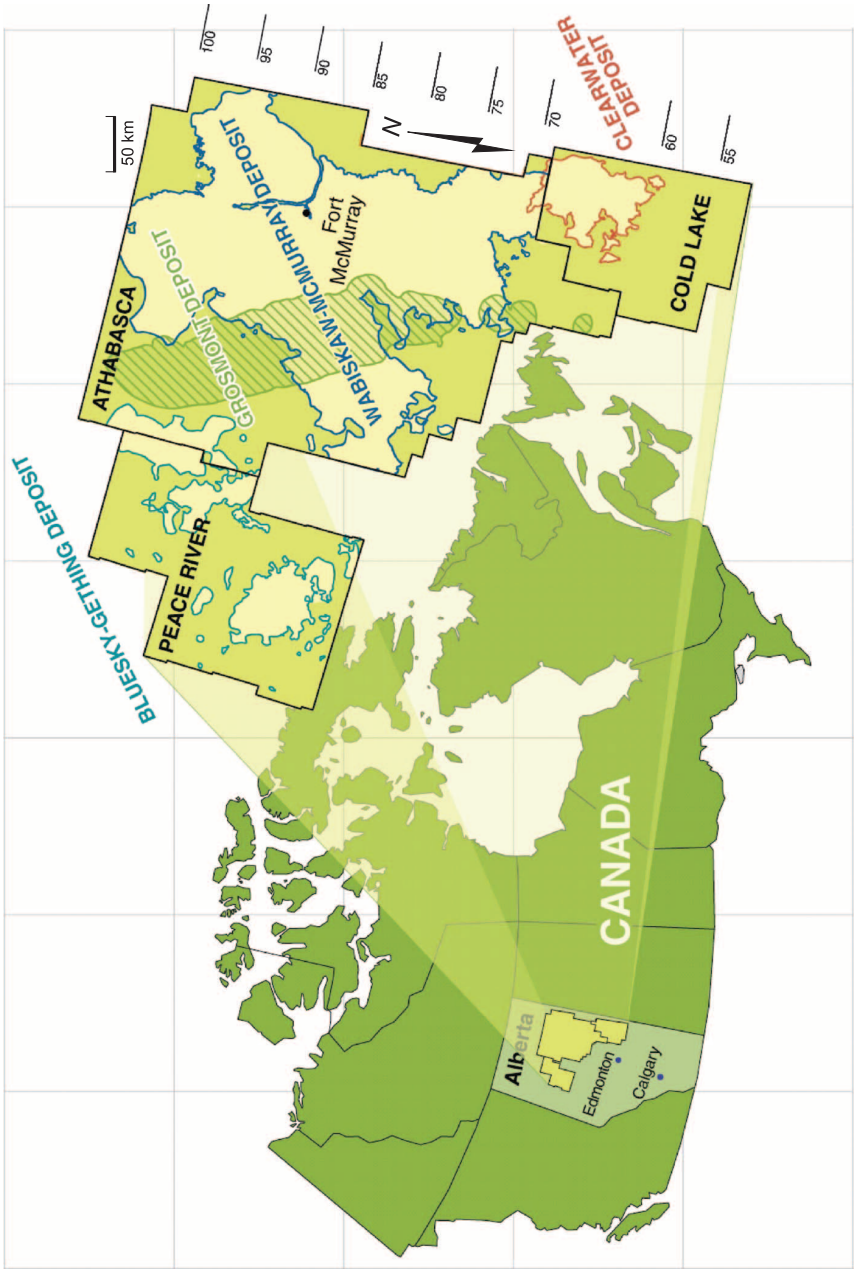

Figure 8.1: Localisation of the Athabasca oil sands area of northern Alberta. The two largest deposits are represented with a blue outline and a gray hatched pattern. Figure taken from Hein et al. (2013).

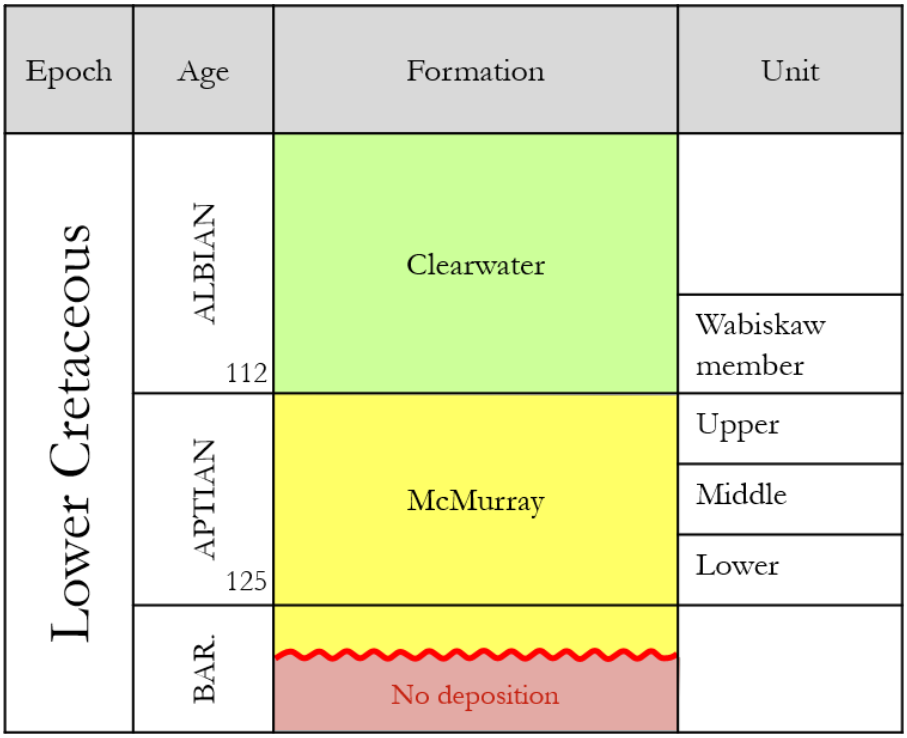

Figure 8.2: Schematic succession of the formations of interest in the Athabasca area, northern Alberta, Canada.

8.2 Grid definition and analysis of the available data

The unstructured grid has been defined by merging four layers corresponding to geological units of Lower, Middle, Upper McMurray and Wabiskaw member (Fig. 8.3). It has 2.10^6 prisms with a triangular basis, with sizes varying from 1 m to 2653 m horizontally and from 0.003m to 67 m vertically (Fig. 8.4). The volume of the cells vary from 6.10^{-7} m^3 to 2.10^7 m^3. The grid has been defined in the UVT space, with T coordinate varying between 0 and 1.

The data analysis was performed taking into account only the McMurray units, because of a lack of data in the Wabiskaw member layer. A total of 125,000 data points are considered. They allow defining facies proportions for the entire McMurray formation, and more precisely for Lower, Middle and Upper McMurray. Five facies are taken into ac-

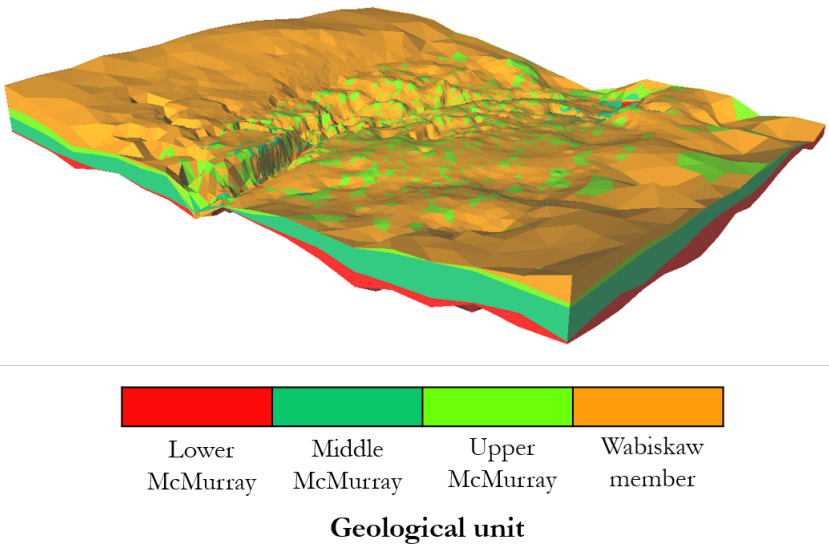

Figure 8.3: The grid is defined by four layers: Lower, Middle and Upper McMurray, and Wabiskaw member of the Clearwater formation.

count: shale, laminated shale, laminated sand, channel sand and breccia. They are named F0, F1, F2, F3 and F4, in the same order. The calculated proportions are available in Table 8.1 and presented on the charts in Figure 8.5. The global proportions of facies in the whole grid are 23% of shale, 21% of laminated shale, 21% of laminated sand, 33% of channel sand and 2% of breccia. To define a variogram for facies simulation, an analytical variogram is fitted on the experimental variograms (Fig. 8.6). It has two structures: one small exponential structure with ranges 300x300x5m and a contribution of 75%; and one large Gaussian structure with ranges 4000x4000x35m and a contribution of 25%.

The fitted analytical variogram for porosity has two structures: one small exponential structure with ranges 300x300x7m and a contribution of 80%; and one large Gaussian structure with ranges 1500x1500x35m and a contribution of 20% (Fig. 8.7). It will be used both for porosity and permeability. The experimental distribution of porosity values inside each facies is approximated with a beta fit visible in Figure 8.8. Generally, porosity in shales and laminated shales is lower than porosity in sands.

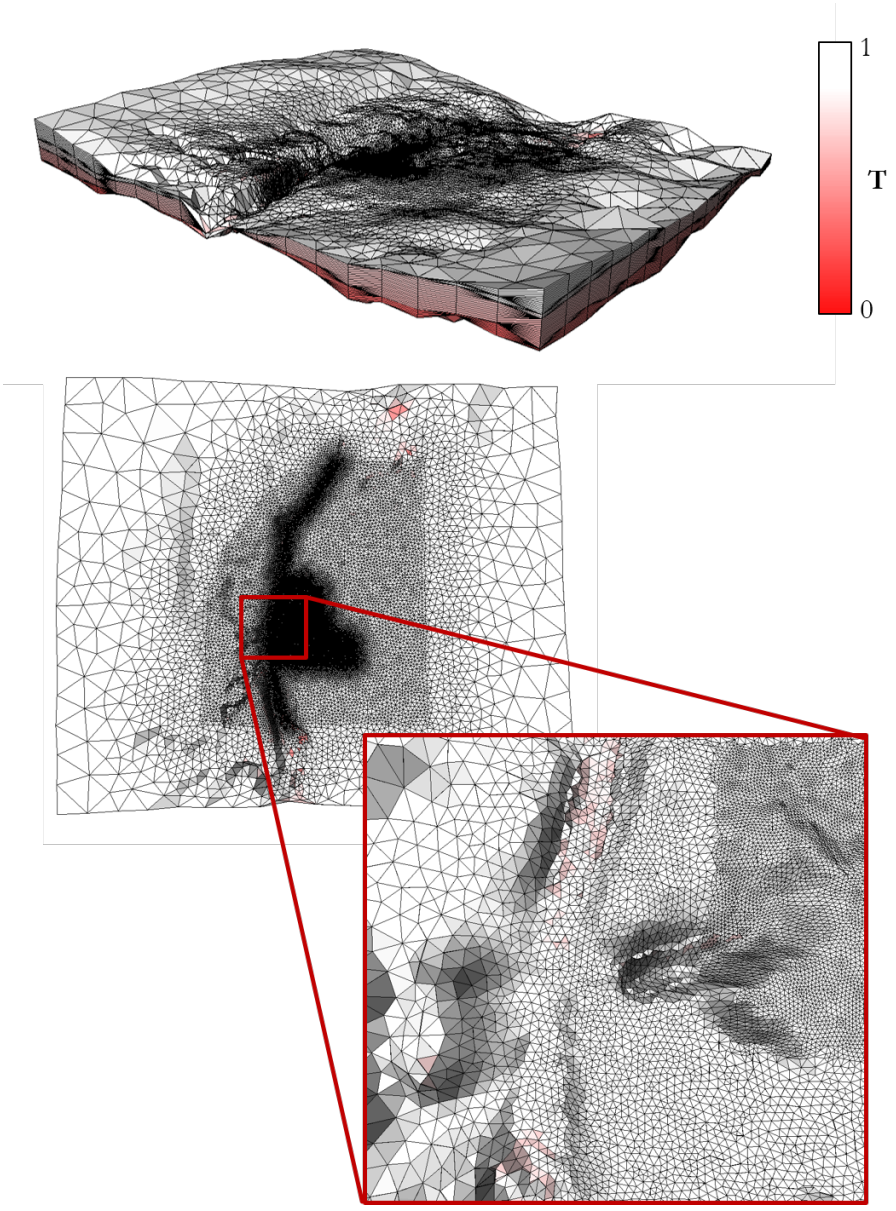

Figure 8.4: The grid is composed of prisms with a triangular basis, with volumes varying from 6.10^{-7} m^3 to 2.10^7 m^3.

The experimental distribution of $\log K$ values inside each facies, except F4 for which no data was available, is approximated using a Gaussian function. The statistics of the distributions are described in Fig-

ure 8.9. The global correlation between porosity and $\log K$ is 0.5, but the correlation inside each facies is closer to 0.8 (Fig. 8.10).

	Shale	Laminated shale	Laminated sand	Channel sand	Breccia
Global	0.23	0.21	0.21	0.33	0.02
Upper	0.15	0.41	0.44	0.00	0.00
Middle	0.19	0.26	0.22	0.29	0.04
Lower	0.33	0.05	0.10	0.51	0.01

Table 8.1: Proportions of facies for the global McMurray formation, and the Lower, Middle and Upper McMurray units.

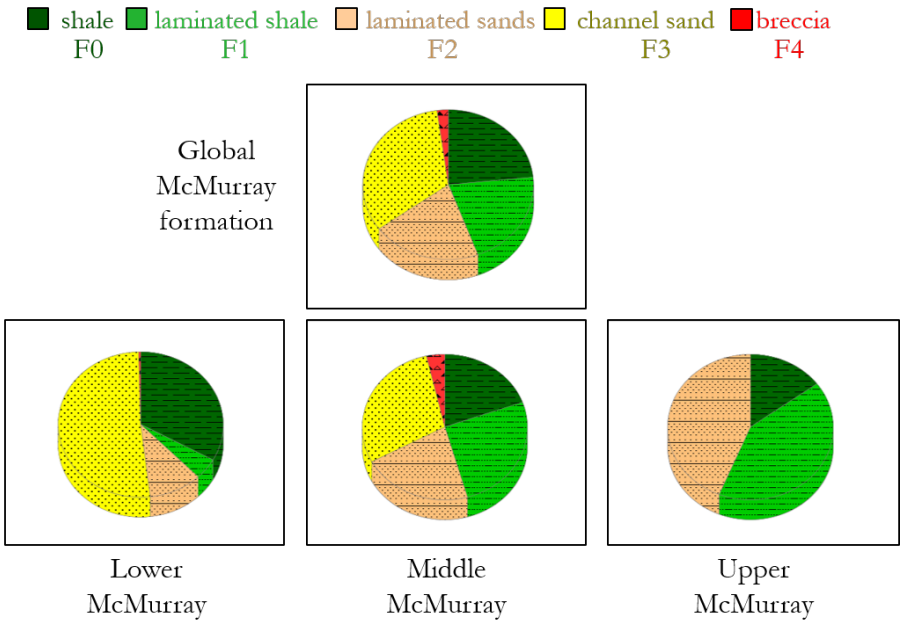

Figure 8.5: Pie charts of the proportions of facies inside the McMurray formation and Lower, Middle and Upper units.

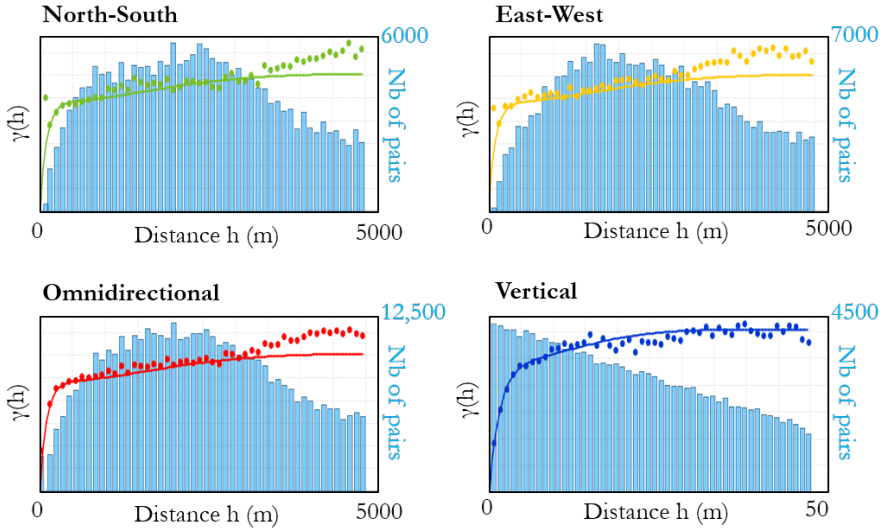

Figure 8.6: Fitting of the analytical variogram on the experimental variograms of the indicator of facies F1, using four different directions.

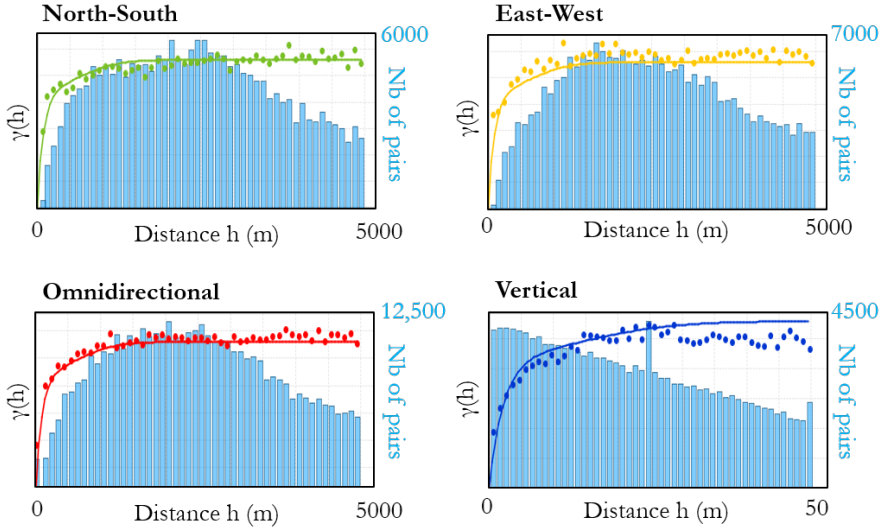

Figure 8.7: Fitting of the analytical variogram on the experimental variograms of porosity data, using four different directions.

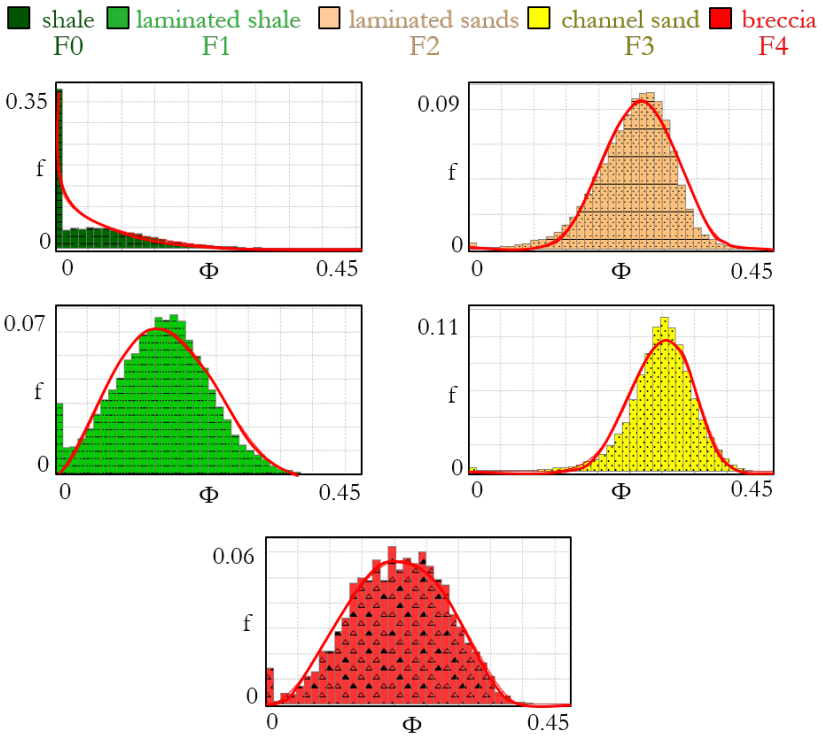

	F0	F1	F2	F3	F4
mean	0.064	0.163	0.253	0.297	0.206
standard dev	0.072	0.073	0.060	0.055	0.075
min	0.00	0.00	0.00	0.00	0.00
max	0.30	0.40	0.425	0.45	0.40

Figure 8.8: Experimental distribution of porosity inside each facies, with the associated beta fitting curve. Statistics of the beta distributions are available in the table.

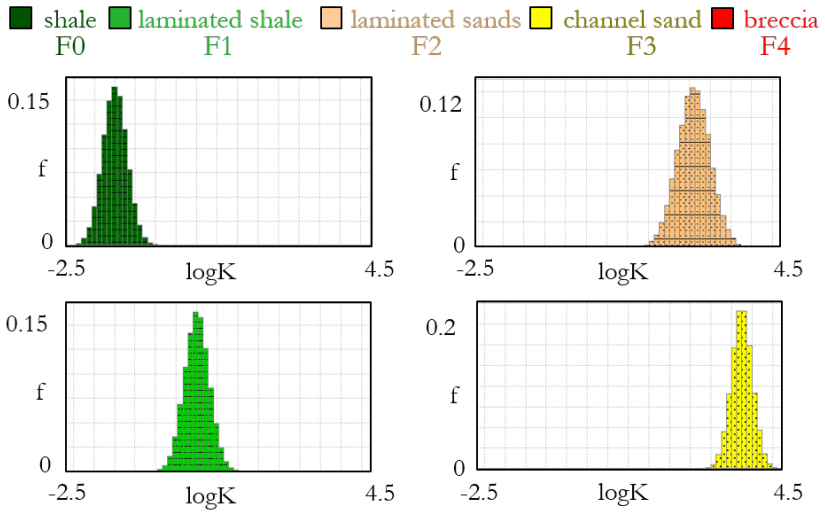

	F0	F1	F2	F3	F4
mean	-1.4	0.6	2.6	3.75	?
standard dev	0.3	0.3	0.4	0.25	?

Figure 8.9: Experimental distribution of the log of permeability inside each facies, with the associated Gaussian fitting curve.

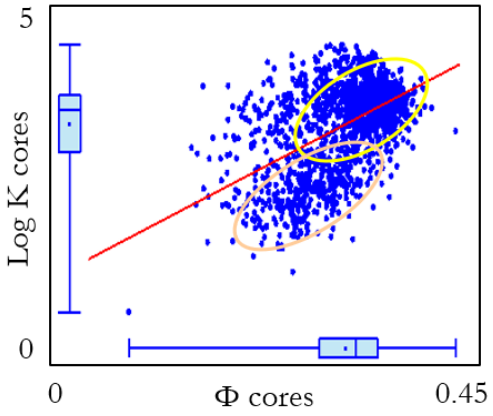

Figure 8.10: Correlation between porosity and $\log K$. The global correlation coefficient is 0.5, while the correlation coefficient by facies is closer to 0.8 (F2 and F3 data are circled on the graph).

8.3 Simulating permeability without facies

In order to simulate permeability without taking facies into account, global distributions of porosity and permeability are defined (Fig. 8.11). They correspond to a combination of the distributions for F0, F1, F2, F3 and F4 when available. The porosity has a beta distribution of mean 0.204, standard deviation 0.11, minimum 0 and maximum 0.45. The log of permeability $\log K$ has a multi-Gaussian distribution with a mean of 1.6 and a standard deviation of 2.1. For the computation of the metamodel, it is possible to simulate both K and $\log K$, in this case, we simply specified to the program that the permeability data are of type log.

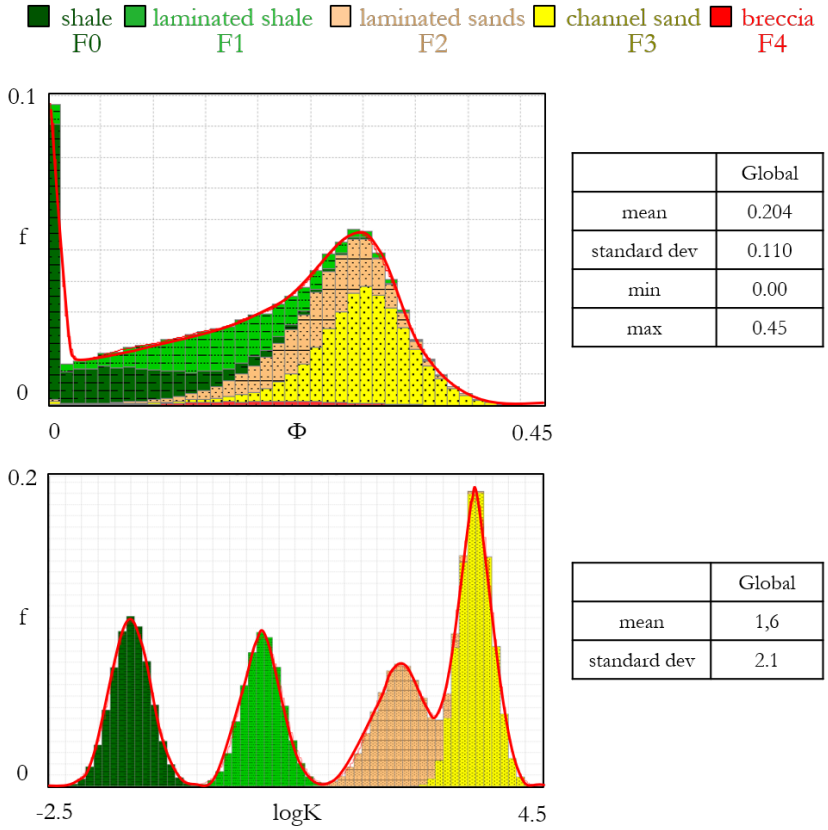

	Global
mean	0.204
standard dev	0.110
min	0.00
max	0.45

	Global
mean	1,6
standard dev	2.1

Figure 8.11: Global distributions of porosity (top) and permeability (bottom), defined by combining all facies distributions and used for simulating permeability without taking facies into account.

Most of the experiments in this work have been performed with confined conditions for the upscaler, because the variations of ω were more interesting to study. However, in the oil and gas industry, linearly-varying head conditions, i.e. unconfined conditions, are considered more realistic. As a consequence, in this chapter, the simulations are performed using unconfined conditions.

The resulting metamodels are shown in Figure 8.12. In terms of horizontal cell sizes, they range only from 20 meters to 1800 meters, whereas the cell's horizontal sizes vary from 1m to 2653m. It is due to a sorting step, added for computational reasons: in order to accelerate the process on this grid, we considered that a cell with a size bellow 20 meters would contain only one integration point, as in practice such a block would contain only one field data. If a cell contains a single point, the determination of ω is useless, hence the absence of experiments below 20m in the metamodels. The upper bound is also inferior to the maximum horizontal cell size. Indeed, large cells represent areas of minimal importance, and the surfaces of response zones concerning large cells present smooth variations. All cells which horizontal size falls outside of the tightened bounds will have the ω corresponding to the closest existing size in the surface.

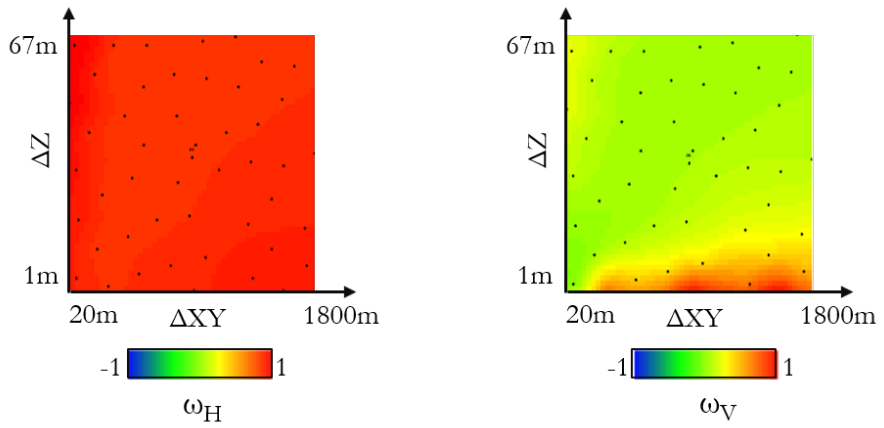

Figure 8.12: Metamodels of horizontal and vertical ω, for Field X simulation without facies.

The properties of ω_H and ω_V generated from the metamodels above are displayed in Figure 8.13.

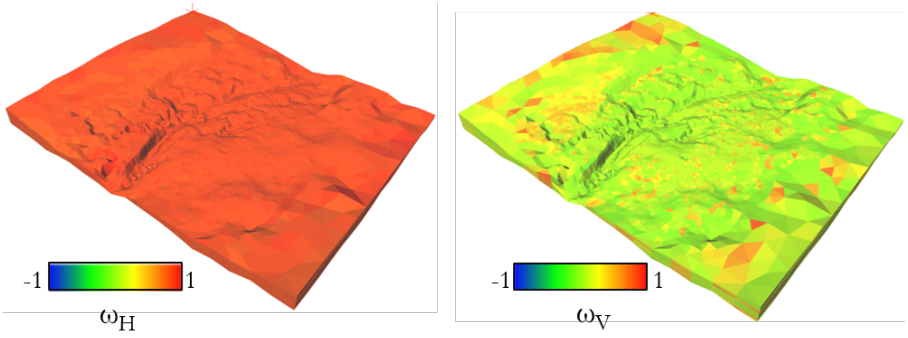

Figure 8.13: Properties of ω_H and ω_V generated from the metamodels presented in Figure 8.12.

Porosity is simulated on the grid, followed by permeability that is correlated to porosity with a linear correlation coefficient of 0.8 (Fig. 8.14). On the close-up images, it is visible that the structures of porosity, for instance the blue structures, are well reproduced on permeability properties, with green structures corresponding to the blue ones of porosity. Horizontal permeability is globally superior to vertical permeability, which is logical considering the aspect of the surfaces of response. Indeed, the ω_H is almost always superior to the ω_V.

In terms of computation time, the creation of the metamodels took 35.4 minutes, and the simulation using Spectral Turning Bands took 7.5 minutes. In total, 43 minutes were necessary to obtain both vertical and horizontal permeabilities on the unstructured grid. It is only the double of the time needed for the simulation on the toy example, while the number of cells of the grid have been multiplied by more than a hundred. In addition, multi-realizations of permeability would only need $7 \times n$ additional minutes, n being the number of realizations performed.

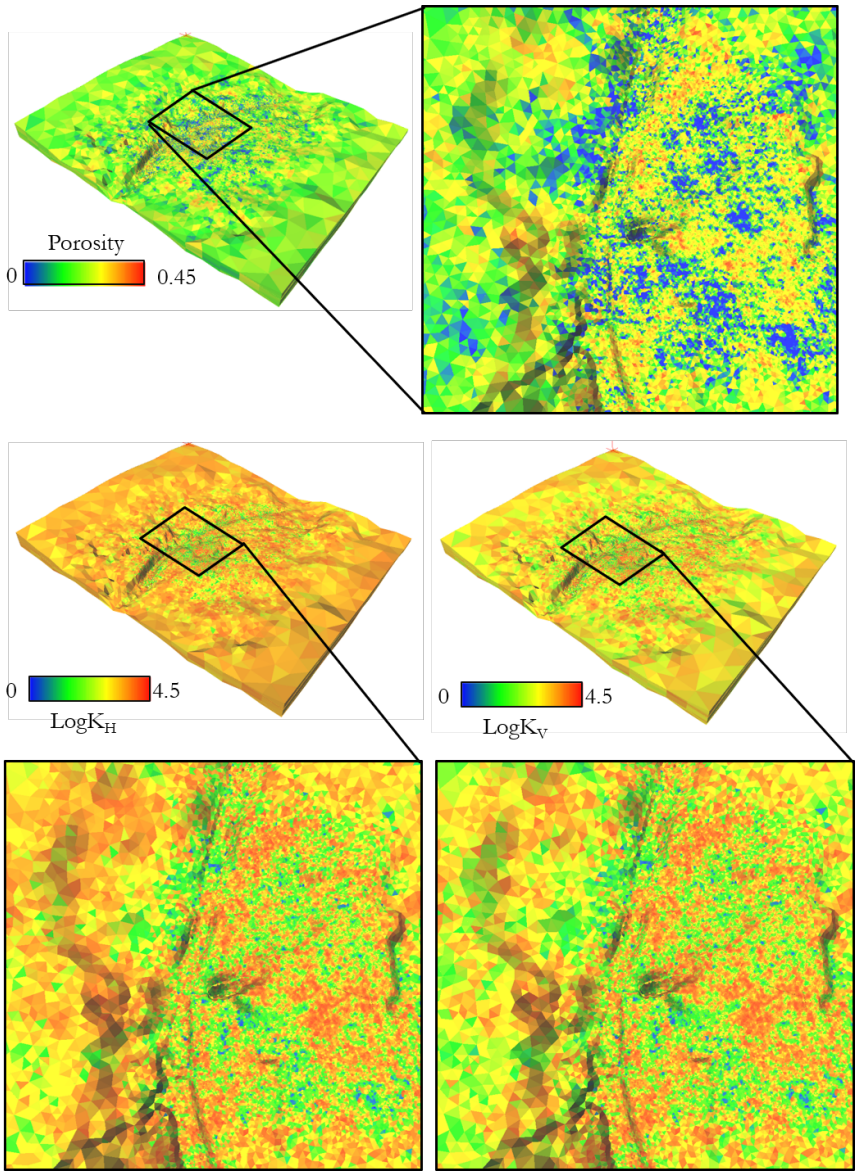

Figure 8.14: Porosity and permeability simulated on the unstructured grid. A close-up image on the refined zone is available for each property. The correlation between porosity and permeability is well visible with structures of identical shape.

8.4 Simulating permeability with two facies

As presented in Section 8.2, the real case study is composed of five different facies. In order to run our code, that is for now limited to two facies, we created two groups of facies: shales (F0), composed of shale and laminated shale, and sands (F1), composed of laminated sands and channel sands. The breccia facies representing only 2% of the model, we decided to neglect it. The histograms of both shales and both sands have been combined. Two distribution models are fitted on the histograms for porosity (Fig. 8.15) and two for permeability (Fig. 8.16). Surfaces of response are generated taking into account log K. The variograms for the facies, the porosity and the permeability are those presented in Section 8.2.

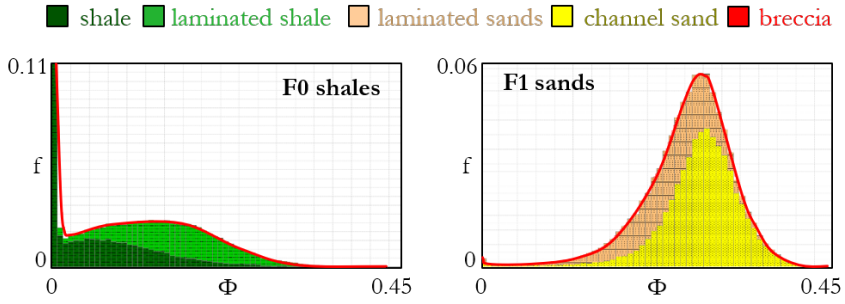

	F0 shales	F1 sands
mean Φ	0.110	0.280
sigma Φ	0.088	0.060
min Φ	0.00	0.00
max Φ	0.43	0.45

Figure 8.15: Combined distributions of porosity for shales (left) and sands (right) with statistics in the bottom table.

On the map of dominant facies (Fig. 8.17 top), the two structures of the variogram are well visible. The small structures can be seen in the detailed area, where the grid is refined. The simulated proportions of facies are taken into account for the generation of the metamodels, as explained in Section 6.2.3 (Fig. 8.17 bottom).

X axis and Y axis being equivalent, only two metamodels are presented hereafter: one for the horizontal exponent $\omega_H = \omega_X = \omega_Y$ and one for the vertical exponent ω_V. Once again, each metamodel is a cube presented on Figure 8.18 and 8.19. The three axes represent: the

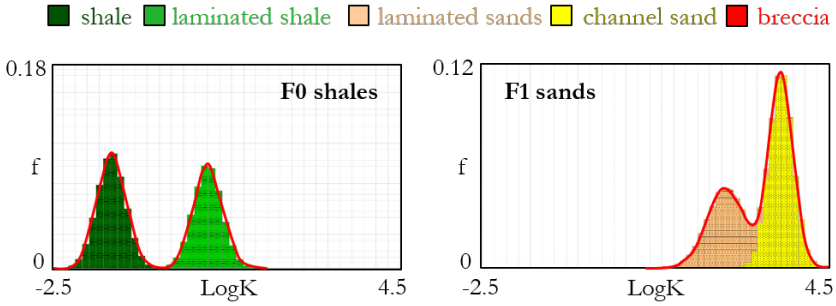

	F0 shales	F1 sands
mean logK	-0.55	3.4
sigma logK	1.0	0.6

Figure 8.16: Combined distributions of logK for shales (left) and sands (right) with statistics in the bottom table.

horizontal cell sizes ΔXY (taken as the mean of the cell sizes in X and Y), the vertical cell sizes ΔZ and the simulated proportion of facies F0 Psim(F0). The values of ω_H are almost always equal to one due to the unconfined boundary conditions. The metamodels for Psim(F0)=0% and 100% are equivalent which is coherent with the variations of ω depending on shale proportion presented in Section 3.2.2. They are not strictly equivalent, because the number of points used for kriging at Psim(F0)=0% and 100% is not necessarily equal.

From the metamodels, one ω is found for each cell of the unstructured grid (Fig. 8.20b). From these ω and from the porosity property (Fig. 8.20c), we obtain the properties of Log K_H and Log K_V ont the Field X (Fig. 8.20d). The vertical permeability is inferior to the horizontal permeability, except for really small cells where it is equal. This is due to the single point used for Spectral Turning Bands in the small cells making the upscaling independent from ω. The internal variability inside each facies is well visible on the close-up images in Figure 8.21. One can easily distinguish the two facies on the permeability properties, and the correlation to porosity.

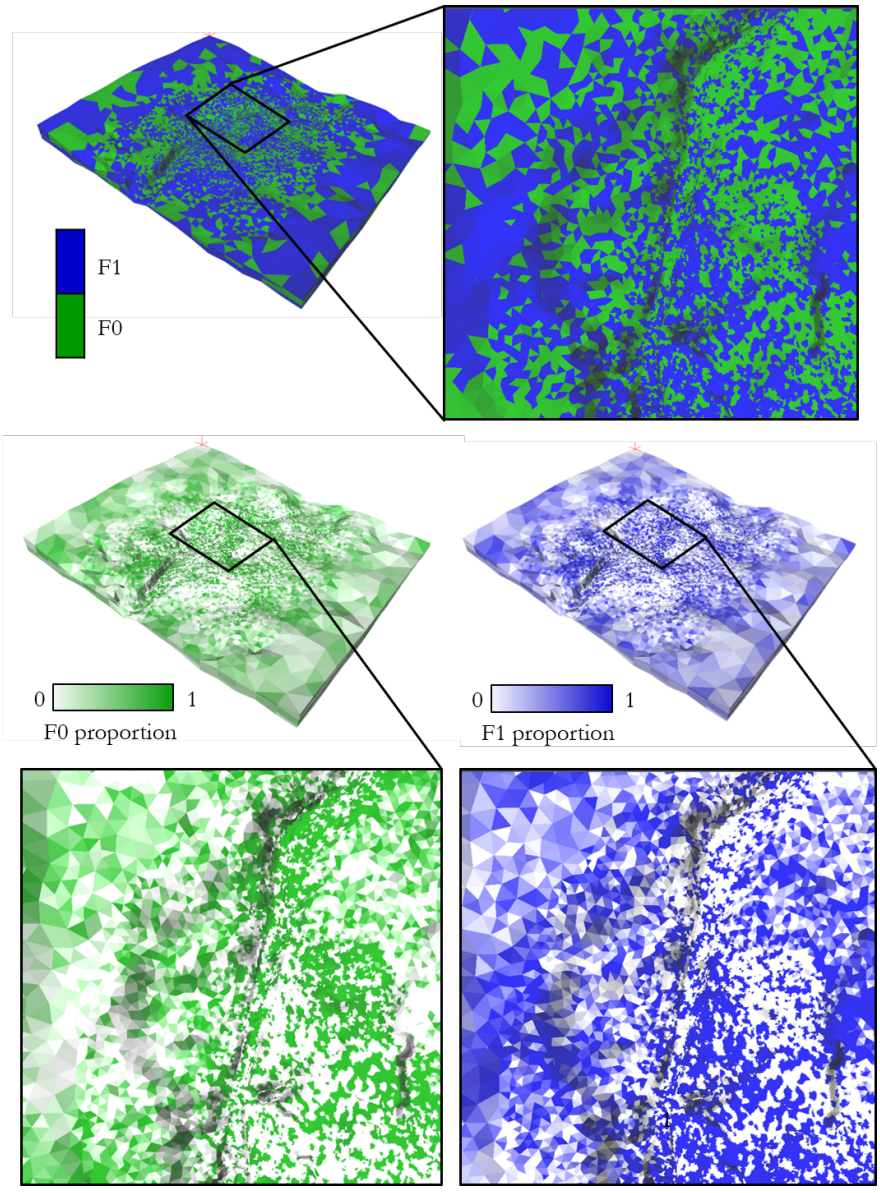

Figure 8.17: Map of dominant facies on top and corresponding simulated proportions of facies F0 and F1 at the bottom.

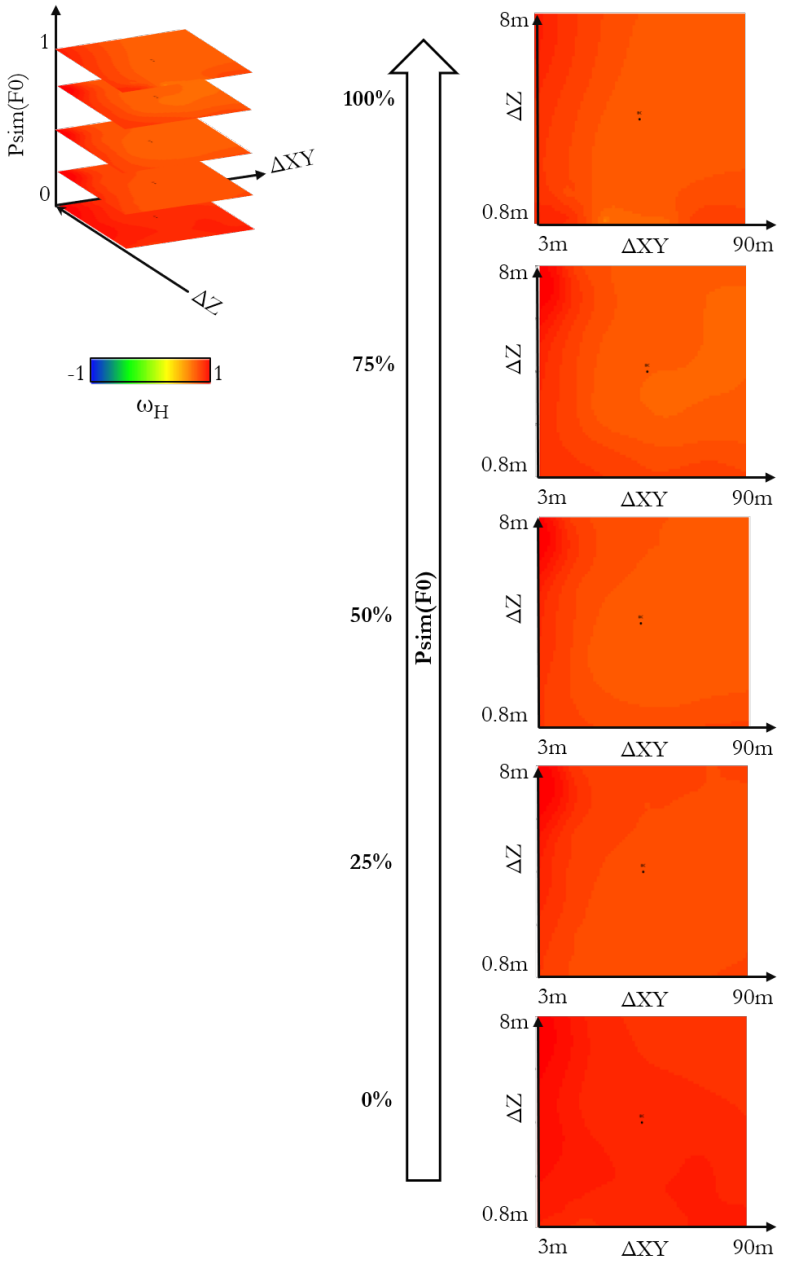

Figure 8.18: Metamodel of ω_H (top left), with surfaces for simulated proportions of facies F0: 0, 0.25, 0.5, 0.75 and 1.

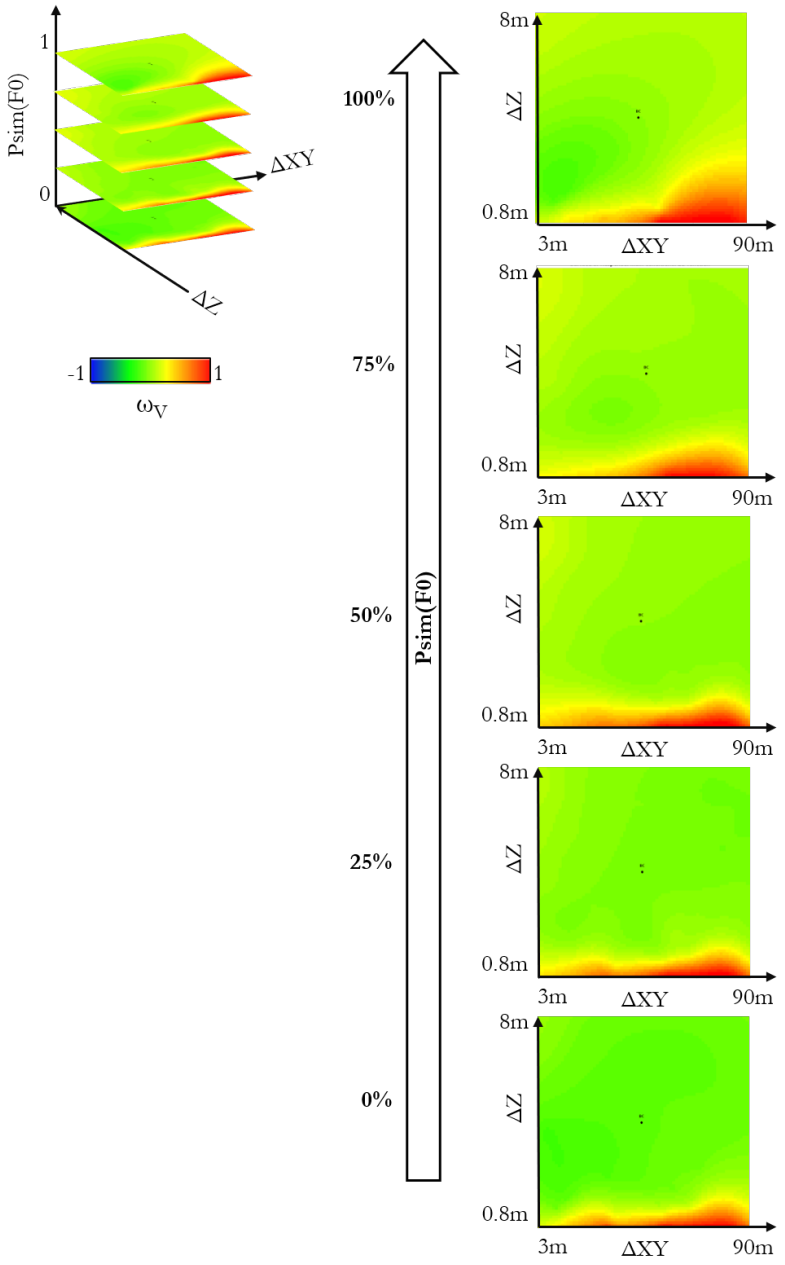

Figure 8.19: Metamodel of ω_V (top left), with surfaces for simulated proportions of facies F0: 0, 0.25, 0.5, 0.75 and 1.

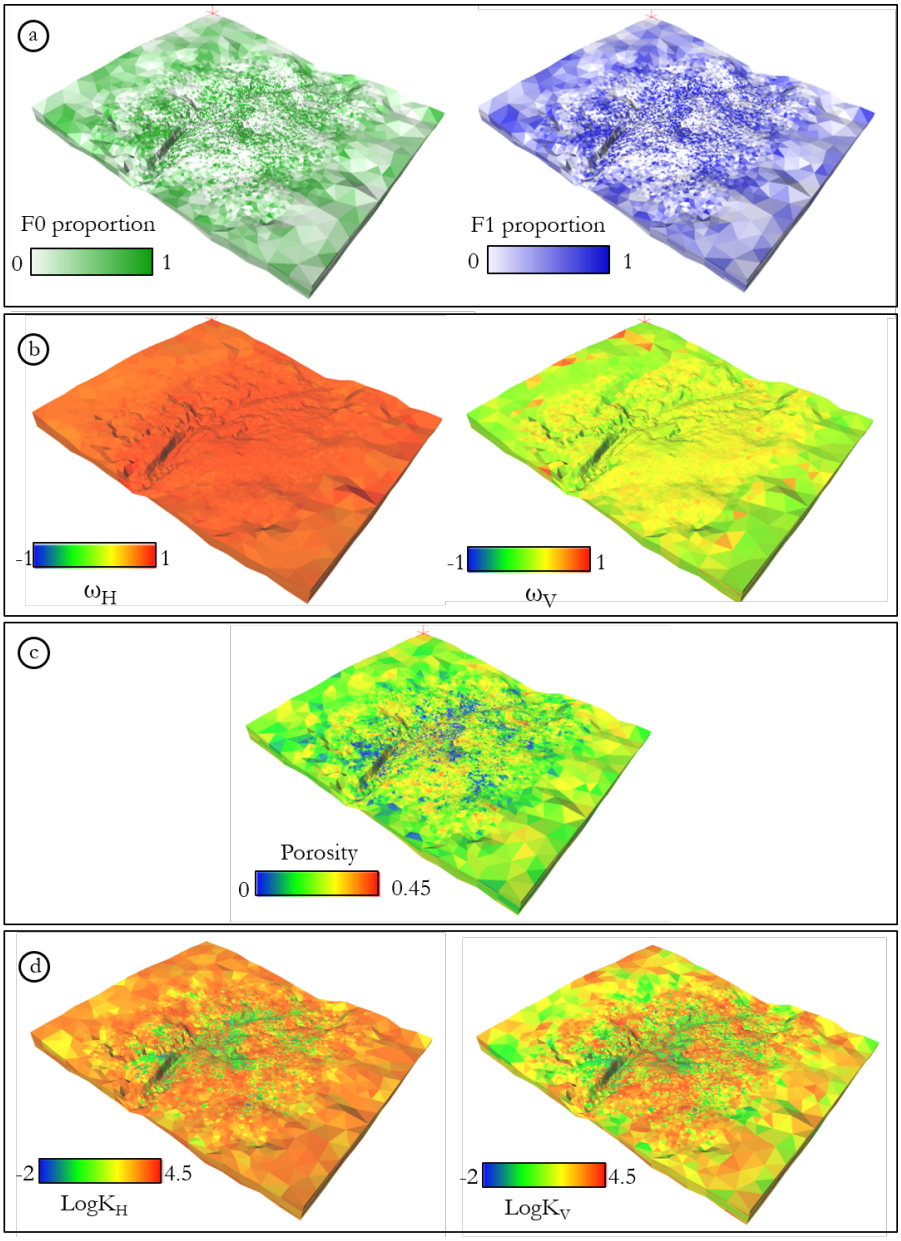

Figure 8.20: a) Recall of facies proportions on the grid. b) Properties of ω_H and ω_V. c) Porosity on the grid. d) Properties of LogK_H and LogK_V on Field X unstructured grid.

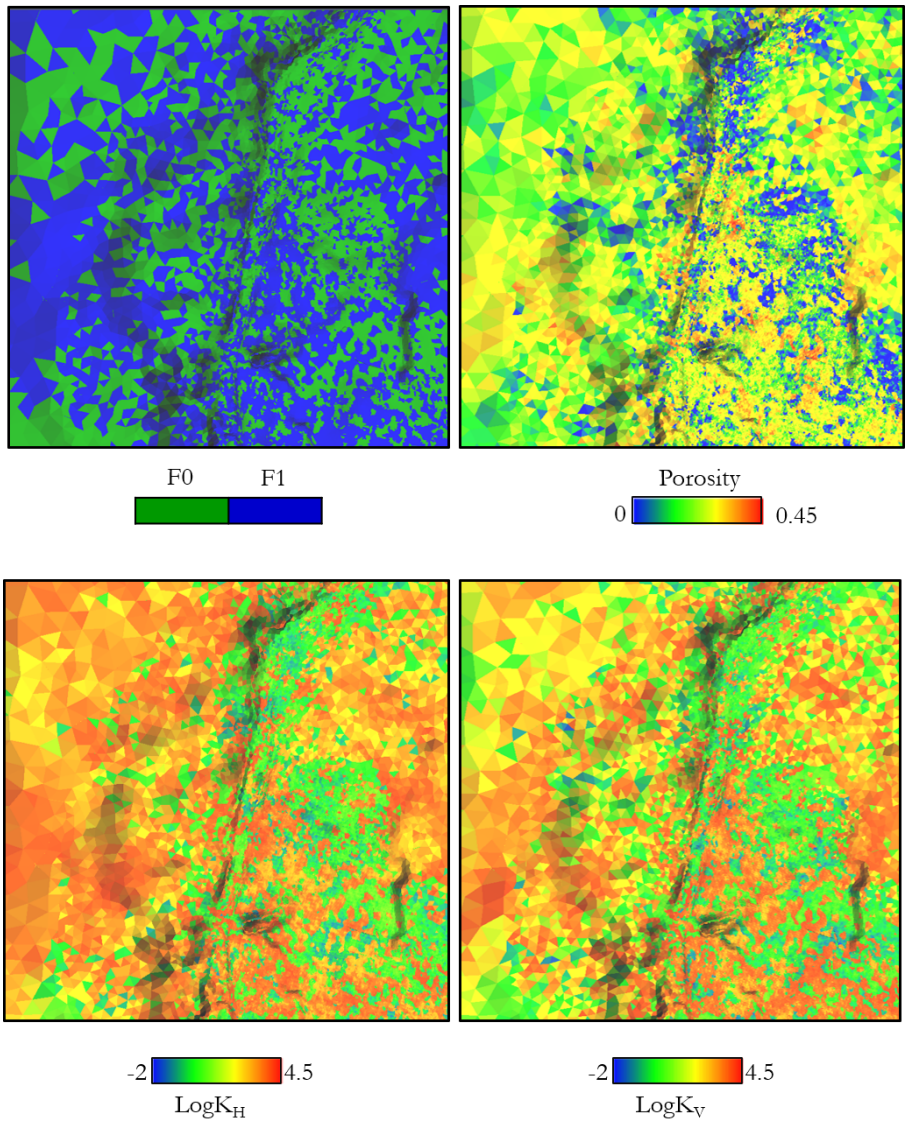

Figure 8.21: close-up: dominant facies and porosity properties (top) and LogK_H and LogK_V properties (bottom).

8.5 Conclusion

The results obtained in this chapter show the applicability of the method to a real case study, for industrial purposes. The approach has been applied using distributions and variograms derived from real

data. The whole process is available within Total internal geomodelling platform Sismage and is connected to the other already existing modules. The approach is general, it can be applied to any shape of the histograms. The user can decide whether he wants to obtain either K or $\log K$. The computation times are reasonable (approx. 40 minutes for the case without facies and 3 hours for the case with facies). Even though, for industrial purposes, the code would need to be accelerated. The author is aware of a main point that can be improved for decreasing computation times. Indeed, the pressure solver is used, for the moment, outside the Sismage platform, through an execution script, which is more time consuming than if the upscaler was directly implemented in Sismage. The results are consistent with the model statistics. However, a more complete analysis, including flow simulations like the one presented in Chapter 5, should still be performed.

Chapter 9

Conclusion

9.1 Main contributions

The change-of-support for permeability has been a topic of studies for a few decades now. The scope of research on these methods is still large.

The research presented in this document proposes a new workflow allowing to simulate directly permeability fields on unstructured grids accounting for support effects. The main originality of the method is that it allows bypassing on the one hand the use of a fine grid that would require using a large memory space and on the other hand the repeated and time consuming use of local upscaling on every fine-scale realization.

The approach consists in the following steps: after computing the size and aspect ratio of each cell of the unstructured grid, a series of numerical experiments are performed. They allow to determine, for some representative cell dimensions, the exponent ω by minimizing the error between reference permeabilities estimated numerically and power averages using the exponent ω. From these experiments, we construct a response surface or metamodel from which an ω value can be found for any cell geometry. Then, for every realization, several points are placed inside each cell and the permeability is simulated on these points using the Spectral Turning Bands approach. The power averaging technique is then applied using the value of ω derived from the response surface to obtain the equivalent permeability of the cell.

The main strength of this workflow is that the averaging exponents ω are estimated once for a given problem constrained by a permeability distribution, a variogram and an unstructured grid. After that, sev-

eral realizations of permeability fields can be obtained efficiently using Spectral Turning Bands.

The method is available for heterogeneous media with a single or two facies. We have shown the application of the approach to a toy example without facies. The results are encouraging regarding the reproduction of the model statistics. Moreover, we performed flow simulations to compare our results to a fine grid, showing successfully the consistency of our permeability properties. The method has also been applied, with one and two facies, to a real case study on Field X. This experiment highlighted the applicability of the approach for industrial real cases, in Total geomodeling platform *Sismage* and with reasonable computation times. The proposed method can be used as an extension to a previous method implemented in *Sismage*, that allows to generate geostatistical simulation of additive variables directly on unstructured grids (e.g. Biver et al., 2019).

9.2 Discussion and perspectives

Our results also raises some questions and directions for possible future research. We discuss below some clues and ideas that could be followed to answer these questions.

9.2.1 Upscaling parameters

The first question relates to the numerical upscaling method used in the experiments as a reference. Numerical upscaling is more general and flexible than analytical solutions, but the results are dependent on a few parameters such as the type of boundary conditions, or the choice of the averaging technique used for transmissibility computation (see Section 2.3.4).

Three main boundary conditions are used in general: permeameter-type, linearly-varying head, and periodic. In this paper, we presented results that were obtained with permeameter-type and linearly-varying head conditions. The resulting surfaces of response are clearly different, and so are the permeability properties. For the cases without facies, the differences between permeability properties are small, but they increase with the apparition of more heterogeneities. To select which boundary conditions are the most adequate under practical and reservoir conditions, additional research should be conducted. As there is no exact solution to the problem stated by numerical upscaling at our scale, the

idea would be to find out which boundary conditions bring the closest dynamic results to the ones obtained on a fine grid (considered more accurate). Experiments could be performed in the same way as done in Mourlanette et al. (2020). The results are affected by the choice of boundary conditions, but the general methodology itself would not be affected.

It is also known (see for example Romeu and Noetinger, 1995) that numerical upscaling methods can be biased when the grid cell size is smaller or close to the correlation scale of the permeability field. This bias is due to the underlying numerical scheme. In the case of finite difference or finite volumes, the scheme that is used to average the transmissibility between grid-blocks is directly affecting this error: the harmonic averaging formula employed by most popular commercial simulators leads to a systematic underestimation of the effective permeability. The effect of this averaging is visible on the 2D-case in Chapter 3.1, with a slight over (or under) estimation of the values when compared to the geometrical mean. For the experiments of the workflow that correspond to cells of the size of the heterogeneities, the choice of the averaging formula has an impact on the reference permeability value, and hence on the estimation of ω. In practice, a known solution for this issue is to refine the grid of the numerical models, but this leads to additional computational costs. This issue could be further investigated since the proposed method is flexible and can be applied with any transmissibility calculation options available in the pressure solver: harmonic, geometric or arithmetic. Again, it could be possible to analyse the impact of this choice on large scale flow simulations.

9.2.2 Power averaging

An important question is whether the power averaging formula is sufficient to capture the details of the spatial complexity of the permeability fields. Previous numerical experiments (e.g. Renard et al., 2000) have shown for example a broad dispersion of the equivalent permeabilities around power averages. However, and rather surprisingly, the numerical experiments conducted in this work show that the method is robust for the treated random fields. Moreover, the approximation made concerning a unique ω per cell dimensions and proportions of facies is acceptable in most cases (Chapter 3). The most problematic cases were the ones with object-based channels, with a strong contrast between shale and sand permeabilities and a strong anisotropy of the medium due to channels. Further studies should be performed to assess precisely

the factors impacting the quality of the approximation. Overall, its quality should be monitored during the whole surface of response process, by checking for each experiment that the power averaging distribution is well fitted to the reference distribution. An idea would be to store the remaining error of the ω optimization. This means that, even if we did not encounter this problem yet, the methodology would include a step to identify situations in which the method could have difficulties. The reference and power averaged distributions for each experiments should be kept. Then, in problematic situations, one could apply a quantile-to-quantile correction of permeability, replacing the permeability in cells flagged as "bad" by the corresponding reference, numerically upscaled, permeability.

9.2.3 Computational efficiency

In terms of computation time, the comparison between the method using a fine grid and ours showed that, for one single realization on a small grid, our method is slower. This is due to the requirement of conducting an ensemble of numerical simulation and upscaling to train the metamodels target to the simulation. This step is computationally expensive. It could be optimized in different ways. First, the upscaling for reference permeability is performed with a pressure solver that is, for the moment not integrated in the Sismage platform. The steps of 1) writing the fine grid permeability in a file, 2) run the upscaler by executing a script to upscale this permeability and 3) read the response given by the upscaler in a file, are really time consuming and could be replaced by an implementation of the uspcaler directly in Sismage. Moreover, we could store the results of these numerical experiments in a data base and retrieve them if the same type of cases are encountered multiple times instead of re-running the numerical computation. Even with this costly steps, our method is faster as soon as two realizations of permeability are performed, or if a very large grid is considered. We consider therefore that the complete cost of designing the experiment, running them and identifying the ω values is rapidly compensated.

9.2.4 Multiple facies

So far, the methodology is limited to two facies only. The limiting factor is the kriging of the metamodel. Indeed, we use an automated tool for covariance identification and kriging (detailed in Section 4.2.3) that is available only for the 2D and 3D cases. Having two facies implies only

one proportion axis (because facies proportions are complementary), so there are at maximum three dimensions for the metamodel. For more facies, we need a tool able to deal with at least 4 dimensions.

Therefore, to increase the number of facies, there is a need to rely either on an extension of the existing kriging metamodel tool or to look for an alternative with reasonable neighbouring options. We also note that in these cases, kriging should not be conducted in the space of proportions. This space has specific properties, in particular the sum of the proportions is always equal to 1. The parameter space is not cartesian anymore and it implies that we need a transformation to ensure that the kriging performs correctly in that space.

9.2.5 Non stationary proportions

Another important issue is that the proposed method does not account for non stationarity in the target proportions. We tested in section 6.1 the influence of the target and simulated proportions on the final distribution of permeability. We observed that the target proportions have little influence on the distribution of permeability while the simulated proportions do. While this is true, target proportions will still have an impact on the metamodels. Indeed, we wrote in Section 6.2.2 that the metamodel will not have points in every area of the parameter space. It is explained by the support effect: for the largest cells, the simulated proportion will tend toward the target proportion. For these cells, there will be no points in the metamodel far from the target proportion. Now, when one considers a non-stationary field of facies, i.e. a field where the target proportion of facies changes, the largest cells will have varying target proportions and corresponding varying simulated proportions. Then, it is important that the metamodel covers all the possible areas, including different simulated proportions for largest cells.

Regarding the methodology, the idea is to add the target proportions as an axis of the initial parameter space when designing the numerical experiments. Each experiment will have as coordinates the cell sizes and a target proportion of facies $F0$ (when working with two facies only). This will ensure that the $P_{simulated}$ values will vary even for large cells. The coordinates used to conduct the numerical experiments can be obtained with the same procedure as before (Section 6.2.2), creating D-dimensional vectors of the form (ΔM,Δm,Δt, P_{target}(F0)).

During the analysis of the numerical results, we will not consider P_{target}, but group the results having the same $P_{simulated}$ and use this proportion in the metamodels as done previously. In other words, we

propose only to modify the design of the numerical experiments, the rest of the methodology remains identical (see Chapter 6): the experiments are performed, creating points along the simulated proportions axis by sorting the blocks into $P_{simulated}$ groups. In the final parameters space, the P_{target} axis disappears because only $P_{simulated}$ has an impact on the value of ω. Once the metamodels are obtained, the non-stationary simulation on the grid is made possible by the Spectral Turning Bands presented in Emery and Arroyo (2017).

This routine would be easy to use when taking into account two facies, because there is only one axis of target proportion. However, as soon as one will want to work with more facies, the placement of the P random points in the initial space of parameters has to be done such that every point will have target proportion coordinates that sum to one.

To ensure that this constraint is properly respected, we could use the following methodology. For one point, let K be the number of facies. $(K-1)$ values are drawn randomly between 0 and 1. A zero and a one are added to this tab of random values and it is sorted in ascending order. By considering the intervals between the tab values,K proportions of facies which sum to one are obtained. They define the proportion coordinates of the point. This methodology has been tested with three facies to check if the coverage of the facies proportions space is good. The results are displayed in Figure 9.1 and are relevant.

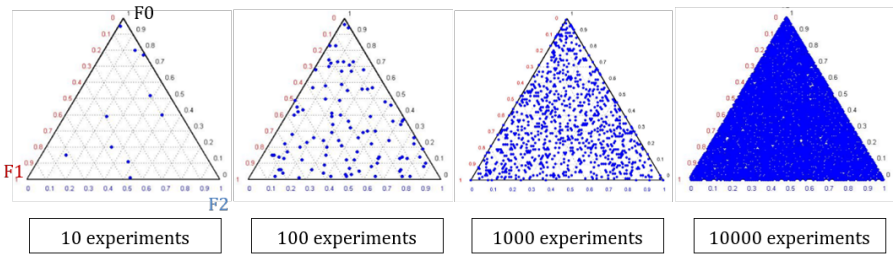

Figure 9.1: Distribution of the P candidate points in the facies proportions space. The higher P is, the better the coverage.

9.2.6 Anisotropy

The implementation of the proposed method considers only horizontally isotropic heterogeneities. The isotropy asumption permits to consider Mmt axes aligned to XYZ axes, but for anisotropic structures

such as channels, it will be different. Indeed, we defined Mmt axes such that they follow the main directions given by the global variogram. In anisotropic cases, the tensor of permeability will be calculated in Mmt space, but it has to be given to the dynamic simulator in XYZ space. A rotation of the tensor from Mmt to XYZ space would have to be performed. We want to note that it would be even more accurate to take into account the local anisotropy inside each cell to define local Mmt axes and perform local tensor rotations. Taking into account anisotropy is a key step to allow the simulation of more complex facies structures.

9.2.7 Multiphase flow

The proposed method allows to simulate directly the absolute permeability. For multiphase flow, this is not sufficient since the relative permeability needs to be upscaled as well (Eichel et al., 2005; Rabinovich et al., 2016). Simulating directly relative permeability curves on an unstructured grid while accounting for the support effect could be a next step in this research. The way to proceed is of course still very open. One idea could be to use an analytical approximation based on a power average that was developed recently in Total (Massonnat, 2017). This analytical method relies on the hypothesis that there is an adequacy between the spatial organization of the absolute permeability field and the one of the relative permeability field. It has, however, not yet been tested in a large number of cases and its consistency should be further investigated.

9.2.8 Gridding issues

Another question revolves around the definition of the unstructured grid. We have seen in Chapter 5 that, for flow simulations, the cells of our mesh between two wells were too coarse. It is common in practice that the mesh is built by engineers in order to get the best compromise: ensuring a global accuracy at the lowest numerical cost. Usually, in unstructured grids, very fine grid blocks are employed close to the wells or faults, while coarse blocks are used far from the wells. The largest numerical errors may occur in the transition zone with grid block sizes that may be compared to the size of the heterogeneities. Preux (2016), Gratien, Jean-Marc et al. (2016) and references therein offer some indicators to check the quality of the coarse reservoir model. These indicators permit to define the zones where the grid should be refined.

Bibliography

I. Aavatsmark, T. Barkve, O. Bøe, and T. Mannseth. Discretization on unstructured grids for inhomogeneous, anisotropic media. part i: Derivation of the methods. *SIAM Journal on Scientific Computing*, 19(5): 1700–1716, 1998.

R. Ababou. Random porous media flow on large 3-d grids: numerics, performance, and application to homogenization. In *Environmental Studies*, pages 1–25. Springer, 1996.

B. Abramovich and P. Indelman. Effective permittivity of log-normal isotropic random media. *J. Phys. A: Math. Gen.*, 28:693–700, 1995.

M. Akhurst, S. D. Hannis, M. F. Quinn, J.-Q. Shi, M. Koenen, F. Delprat-Jannaud, J.-C. Lecomte, D. Bossie-Codreanu, S. Nagy, Ł. Klimkowski, et al. Risk assessment-led characterisation of the sitechar uk north sea site for the geological storage of co2. *Oil & Gas Science and Technology–Revue d'IFP Energies nouvelles*, 70(4):567–586, 2015.

I. Antonov and V. Saleev. An economic method of computing lp_τ-sequences. *USSR Computational Mathematics and Mathematical Physics*, 19(1):252–256, 1979.

M. Armstrong, A. Galli, H. Beucher, G. Le Loc'h, D. Renard, B. Doligez, R. Eschard, and F. Geffroy. *Plurigaussian Simulations in Geosciences*. Springer Science & Business Media, 2011.

V. Artus and B. Nœtinger. Up-scaling two-phase flow in heterogenous reservoirs: Current trends. *Oil and Gas Science and Technology*, 59(2): 185–195, 2004.

C. Bennis, J.-F. Rainaud, M. Poudret, and M. Elkouhen. 3d meshes for structural, stratigraphy and reservoir frameworks. In *Shared Earth Modeling: Knowledge Driven Solutions for Building and Managing Subsurface 3D Geological Models*. IFP énergies nouvelles publications, 2013.

A. Bertoncello, J. Caers, P. Biver, and G. Caumon. Geostatistics on stratigraphic grids. In *Eighth Geostatistical Geostatistics Congress*, pages 677–686, Santiago, Chile, 2008. Gecamin, Ltd.

P. Biver, S. Fuet, and D. Allard. Direct geostatistical simulation on unstructured grids i: Recent improvments for additive variables. *Proceedings of the Fourth EAGE Conference on Petroleum Geostatistics, Florence, Italy*, 2019.

D. Blessent, R. Therrien, and C. W. Gable. Large-scale numerical simulation of groundwater flow and solute transport in discretely-fractured crystalline bedrock. *Advances in Water Resources*, 34(12):1539–1552, 2011.

O. Boe. Analysis of an upscaling method based on conservation of dissipation. *Transport in Porous Media*, 17:77–86, 1994.

E. Bonnet, O. Bour, N. Odling, P. Davy, I. Main, P. Cowie, and B. Berkowitz. Scaling of fracture systems in geological media. *Reviews of Geophysics*, 39(3):347–383, 2001.

A. Boschan and B. Nœtinger. Scale dependence of effective hydraulic conductivity distributions in 3d heterogeneous media: a numerical study. *Transport in porous media*, 94(1):101–121, 2012.

A. Botella. *Génération de maillages non structurés volumiques de modèles géologiques pour la simulation de phénomènes physiques.* PhD thesis, Université de Lorraine, 2016.

A. Boucher and R. Dimitrakopoulos. Block simulation of multiple correlated variables. *Mathematical Geosciences*, 41:215–237, 2009.

B. Bourbiaux, R. Basquet, M.-C. Cacas, J.-M. Daniel, and S. Sarda. An integrated workflow to account for multi-scale fractures in reservoir simulation models: Implementation and benefits. *Proceedings of the Abu Dhabi International Petroleum Exhibition and Conference*, 2002.

A. Brovelli and G. Cassiani. A combination of the hashin-shtrikman bounds aimed at modelling electrical conductivity and permittivity of variably saturated porous media. *Geophysical Journal International*, 180 (1):225–237, 2010.

J. Cardwell, W. T. and R. L. Parsons. Average permeabilities of heterogeneous oil sands. *Proceedings of the SPE Los Angeles Meeting of October 1944*, 1945.

G. Caumon, O. Grosse, and J.-L. Mallet. High Resolution Geostatistics on Coarse Unstructured Flow Grids. In *Geostatistics Banff 2004*, volume 14, pages 703–712. Springer Netherlands, 2005.

K. Chen, H. Chen, and P. Xu. A new relative permeability model of unsaturated porous media based on fractal theory. *Fractals*, 28(1), 2020.

J.-P. Chilès and P. Delfiner. *Geostatistics: modeling spatial uncertainty, 2nd edition.* Wiley, 2012.

M. A. Christie, M. Blunt, et al. Tenth spe comparative solution project: A comparison of upscaling techniques. In *SPE reservoir simulation symposium.* Society of Petroleum Engineers, 2001.

I. Colecchio, A. Boschan, A. Otero, and B. Nœtinger. On the multiscale characterization of effective hydraulic conductivity in random heterogeneous media: a historical survey and some new perspectives. *Advances in Water Resources*, 103594, 2020.

B. Corre. Techniques d'homogénéisation. homogénéisation des perméabilités absolues. composition des perméabilités relatives. Report, Total, EP/S/PRO/GTS/BC/91.065, 1991.

G. Dagan. Statistical theory of groundwater flow and transport: Pore to laboratory, laboratory to formation, and formation to regional scale. *Water Resources Research*, 22:120–134, 1986.

G. Dagan. Higher-order correction of effective permeability of heterogeneous isotropic formations of lognormal conductivity distribution. *Transport in Porous Media*, 12:279–290, 1993.

G. Dagan, A. Fiori, and I. Jankovic. Upscaling of flow in heterogeneous porous formations: Critical examination and issues of principle. *Advances in Water Resources*, 51:67–85, 2013.

M. Davis. Production of conditional simulations via the lu decomposition of the covariance matrix. *Mathematical Geology*, 19(2):91–98, 1987.

J.-R. de Dreuzy, P. de Boiry, G. Pichot, and P. Davy. Use of power averaging for quantifying the influence of structure organization on permeability upscaling in on-lattice networks under mean parallel flow. *Water Resources Research*, 46(8), 2010.

G. de Marsily. *Quantitative hydrogeology.* Paris School of Mines, Fontainebleau, 1986.

G. de Marsily, F. Delay, M. Teles, and T. Schafmeister. Some current methods to represent the heterogeneity of natural media in hydrogeology. *Hydrogeology Journal*, 6(1):115–130, 1998.

A. de Wit. Correlation structure dependence of the effective permeability of heterogeneous porous media. *Phys. Fluids*, 7(11):2553–2562, 1995.

A. J. Desbarats. Spatial averaging of hydraulic conductivity in three-dimensional heterogeneous porous media. *Mathematical Geology*, 24(3): 249–267, 1992.

C. Deutsch. Calculating effective absolute permeability in sandstone/shale sequences. *SPE Formation Evaluation*, 1989.

C. Deutsch and A. G. Journel. *GSLIB - Geostatistical Software Library and User's Guide*. Oxford University Press, 1992.

C. Deutsch, T. Tran, and Y. Xie. An approach to ensure histogram reproduction in direct sequential simulation. Technical report, Tech. rep. Center for Computational Geostatistics, University of Alberta, 2000.

C. Deutsch, T. T. Tran, and M. J. Pyrcz. Geostatistical assignment of reservoir properties on unstructured grids. *Proceedings of the SPE Annual Technical conference and exhibition, San Antonio, Texas*, 2002.

C. R. Dietrich. A simple and efficient space domain implementation of the turning bands method. *Water Resources Research*, 31(1):147–156, 1995.

J. Duquerroix, P. Lemouzy, B. Nœtinger, R. Romeu, et al. Influence of the permeability anisotropy ratio on large-scale properties of heterogeneous reservoirs. In *SPE Annual Technical Conference and Exhibition*. Society of Petroleum Engineers, 1993.

L. Durlofsky. Upscaling and gridding of fine scale geological models for flow simulation. *Proceedings of the 8^th Internationnal Forum on Reservoir Simulation, Stresa, Italy*, 2005.

L. J. Durlofsky. Numerical calculation of equivalent grid block permeability tensors for heterogeneous porous media. *Water Resources Research*, 27(5):699–708, 1991.

L. J. Durlofsky. Representation of grid block permeability in coarse scale models of randomly heterogeneous porous media. *Water Resources Research*, 28(7):1791–1800, 1992.

H. Eichel, R. Helmig, I. Neuweiler, and O. A. Cirpka. *Upscaling of Two-Phase Flow Processes in Porous Media*, pages 237–257. Springer Netherlands, 2005.

X. Emery. Testing the correctness of the sequential algorithm for simulating gaussian random fields. *Stochastic Environmental Research and Risk Assessment*, 18(6):401–413, 2004.

X. Emery and D. Arroyo. On a continuous spectral algorithm for simulating non-stationary gaussian random fields. *Stochastic environmental research and risk assessment*, 32(4):905–9019, 2017.

X. Emery and C. Lantuéjoul. TBSIM: A computer program for conditional simulation of three-dimensional gaussian random fields via the turning bands method. *Computers & Geosciences*, 32(10):1615–1628, 2006.

X. Emery and J. Ortiz. Two approaches to direct block-support conditional co-simulation. *Computers & Geosciences*, 37(8):1015–1025, 2011.

X. Emery, D. Arroyo, and E. Porcu. An improved spectral turning-bands algorithm for simulating stationary vector gaussian random fields. *Stochastic environmental research and risk assessment*, 30(7):1863–1873, 2016.

C. L. Farmer. Upscaling: a review. *International journal for numerical methods in fluids*, 40(1-2):63–78, 2002.

S. Geman and D. Geman. Stochastic relaxation, gibbs distributions, and the bayesian restoration of images. *IEEE Transactions on pattern analysis and machine intelligence*, 6:721–741, 1984.

J. Gómez-Hernández. *A stochastic approach to the simulation of block conductivity fields conditioned upon data measured at a smaller scale.* PhD thesis, Stanford University, 1991.

E. Goncalvès da Silva. Méthodes et analyse numériques. Lecture of the Institut Polytechnique de Grenoble, 2007.

P. Goovaerts. *Geostatistics for Natural Resources Evaluation.* Oxford University Press, 1997.

Gratien, Jean-Marc, Ricois, Olivier, and Yousef, Soleiman. Reservoir simulator runtime enhancement based on a posteriori error estimation techniques. *Oil Gas Sci. Technol. - Rev. IFP Energies nouvelles*, 71(5): 59, 2016.

H. Gross and A. Boucher. Geostatistics on unstructured grid - coordinate systems, connections and volumes. *Proceedings of the Petroleum Geostatistics conference, Biarritz, France*, 2015.

D. Guerillot, J. L. Rudkiewicz, C. Ravenne, G. Renard, and A. Galli. An integrated model for computer aided reservoir description : from outcrop study to fluid flow simulations. *Rev. Inst. Fr. Pét.*, 45(1):71–77, 1990.

Z. Hashin and S. Shtrikman. A variational approach to the theory of the effective magnetic permeability of multiphase materials. *Journal of applied Physics*, 33(10):3125–3131, 1962.

C. He, M. Edwards, and L. Durlofsky. Numerical calculation of equivalent cell permeability tensors for general quadrilateral control volumes. *Computational Geosciences*, 6:29–47, 2002.

F. Hein. Geology of bitumen and heavy oil: An overview. *Journal of Petroleum Science and Engineering*, pages 551–563, 2017.

F. Hein, C. Langenberg, C. Kidston, H. Berhane, T. Berezniuk, and D. Cotterill. A comprehensive field guide for facies characterization of the athabasca oil sands, northeast alberta. *Alberta Energy and Utilities Board Special Report*, 13:415, 2001.

F. Hein, D. Leckie, S. Larter, and J. Suter. *Heavy-oil and oil-sand petroleum systems in Alberta and beyond*, chapter A regional geologic framework for the Athabasca oil sands, northeastern Alberta, Canada., pages 207–250. American Association of Petroleum Geologists Tulsa, OK, 2013.

F. J. Hein and D. K. Cotterill. The athabasca oil sands—a regional geological perspective, fort mcmurray area, alberta, canada. *Natural Resources Research*, 15(2):85–102, 2006.

F. J. Hein, D. K. Cotterill, R. Rice, et al. *Subsurface geology of the Athabasca Wabiskaw-McMurray succession: Lewis-Fort McMurray area, northeastern Alberta (NTS 74D/14)*. Alberta Energy and Utilities Board, 2006.

Z. Heinemann. Interactive generation of irregular simulation grids and its practical applications. In *University of Tulsa Centennial Petroleum Engineering Symposium*. Society of Petroleum Engineers, 1994.

G. Hirasaki and P. O'Dell. Representation of reservoir geometry for numerical simulation. *Society of Petroleum Engineers Journal*, 10(04), 1970.

L. Holden, B. Nielsen, and S. Sannan. Upscaling of permeability using global norms. *Proceedings of the 7th European Conference on the Mathematics of Oil Recovery, Baveno, Italy*, 2000.

A. H. Hosseini, O. Leuangthong, C. V. Deutsch, et al. An integrated approach to permeability modeling using micro-models. In *International Thermal Operations and Heavy Oil Symposium*. Society of Petroleum Engineers, 2008.

P. Indelman and G. Dagan. Upscaling of conductivity of heterogeneous formations: General approach and application to isotropic media. *Transport in Porous Media*, 12(2):161–183, 1993.

O. Jaquet, R. Namar, and P. Siegel. Upscaler : guide technique & d'utilisation, memorandum upscaler 009/004. Report, In2Earth, 2017.

A. G. Journel. *Modeling Uncertainty: Some Conceptual Thoughts*, pages 30–43. Springer Netherlands, 1994.

A. G. Journel and C. J. Huijbregts. *Mining geostatistics*, volume 600. Academic press London, 1978.

A. G. Journel and W. Xu. Posterior identification of histograms conditional to local data. *Mathematical Geology*, 26(3):323–359, 1994.

A. G. Journel, C. Deutsch, and A. J. Desbarats. Power averaging for block effective permeability. *Proceedings of the SPE California Regional Meeting, Oakland, California*, 1986.

S. A. Khan and A. G. Dawson. Method of upscaling permeability for unstructured grids, 2004. US Patent 6,826,520 B1.

R. Kruel Romeu. *Ecoulement en milieux heterogenes: prise de moyenne de permeabilite en regimes permanent et transitoire*. PhD thesis, Paris 6, 1994.

C. Lantuéjoul. *Geostatistical simulation: models and algorithms*. Springer-Verlag Berlin Heidelberg, 2002.

C. Lantuéjoul and N. Desassis. Simulation of a gaussian random vector: a propagative version of the gibbs sampler. In *The 9th international geostatistics congress*, pages 174–181, 2012.

G. Le Loc'h. *Étude de la composition des perméabilités par des méthodes variationnelles*. Thesis, Paris, ENMP, 1987.

G. Le Loc'h. An efficient strategy for combining the permeabilities : Practical application on a simulated reservoir. In M. Armstrong, editor, *Geostatistics*, pages 557–568. Springer Netherlands, 1989.

P. Lemouzy. Calcul de la perméabilité absolue effective. Technical Report RF40 2685, Institut Français du Pétrole, 1991.

Q. Liao, G. Lei, Z. Wei, D. Zhang, and S. Patil. Efficient analytical upscaling method for elliptic equations in three-dimensional heterogeneous anisotropic media. *Journal of Hydrology*, 583:124560, 2020.

R. Löhner. Automatic unstructured grid generators. *Finite Elements in Analysis and Design*, 24:111–134, 1997.

J. Mallet. Space-time mathematical framework for sedimentary geology. *Mathematical Geology*, 36:1–32, 2004.

J. Manchuk, O. Leuangthong, and C. Deutsch. *Geostatistics Banff 2004*, chapter Direct Geostatistical Simulation on Unstructured Grids, pages 85–94. Springer Netherlands, 2005.

J. G. Manchuk, M. J. Mlacnik, and C. Deutsch. Upscaling permeability to unstructured grids using the multipoint flux approximation. *Petroleum Geoscience*, 18(2):239–248, 2012.

A. Mantoglou and J. L. Wilson. The turning bands method for simulation of random fields using line generation by a spectral method. *Water Ressources Research*, 18(5):1379–1394, 1982.

M. Masihi, P. Gago, and P. King. Estimation of the effective permeability of heterogeneous porous media by using percolation concepts. *Transport in Porous Media*, 114:169–199, 2016.

G. Massonnat. Method, program and computer system for scaling the modelling data for a hydrocarbon deposit, 2009. patent WO 034253A1.

G. Massonnat. Upscaling des kr - homogénéisation analytique 3d adaptée à la dimension des mailles du modèle. Technical report, Total, 2017.

G. Matheron. Composition des perméabilités en milieu poreux hétérogène, méthode de schwydler et règles de pondération. *Revue de l'Institut Français du Pétrole*, XXII(3):443–466, 1967a.

G. Matheron. *Éléments pour une théorie des milieux poreux*. Masson, 1967b.

G. Matheron. The intrisic random functions and their applications. *Advances in Applied Probability*, 5:439–468, 1973.

G. Matheron. Forecasting block grade distributions: The transfer functions. In M. Guarascio, M. David, and C. Huijbregts, editors, *Advanced Geostatistics in the Mining Industry*, pages 237–251. Springer Netherlands, 1976.

G. Matheron. Change of support for diffusion-type random functions. *Journal of the International Association for Mathematical Geology*, 17 (2):137–165, 1985.

G. Matheron. Quelques inégalités pour la perméabilité effective d'un milieu poreux hétérogène. *Cahiers de Géostatistique*, Fascicule 3:1–20, 1993.

R. Merland, G. Caumon, B. Lévy, and P. Collon-Drouaillet. Voronoi grids conforming to 3d structural features. *Computational Geosciences*, 18:373–383, 2014.

K. Michael, A. Golab, V. Shulakova, J. Ennis-King, G. Allison, S. Sharma, and T. Aiken. Geological storage of co2 in saline aquifers — a review of the experience from existing storage operations. *International journal of greenhouse gas control*, 4:659 – 667, 2010.

M. J. Mlacnik, A. W. Harrer, and Z. E. Heinemann. Locally streamline-pressure-potential-based pebi grids. *Proceedings of the SPE Reservoir Symposium, Houston, Texas*, 2003.

P. Mourlanette, P. Biver, P. Renard, B. Noetinger, G. Caumon, and Y. Perrier. Direct simulation of non-additive properties on unstructured grids. *Advances in Water Resources*, 143, 2020.

A. Nasr, M. Abd-Elmegeed, and A. Hassan. Using power averaging technique to upscale contaminant transport in heterogeneous porous media. *Journal of engineering and applied science*, 65(4):283–305, 2018.

I. Neuweiler and H.-J. Vogel. Upscaling for unsaturated flow for non-gaussian heterogeneous porous media. *Water Resources Research*, 43(3), 2007.

B. Nœtinger. The effective permeability of a heterogeneous porous medium. *Transport in Porous Media*, 15:99–127, 1994.

B. Nœtinger and Y. Gautier. Use of the fourier-laplace transform and of diagrammatical methods to interpret pumping tests in heterogeneous reservoirs. *Advances in water resources*, 21(7):581–590, 1998.

B. Nœtinger and A. Haas. Permeability averaging for well tests in 3d stochastic reservoir models. *Proceedings of the SPE Annual Technical Conference and Exhibition, Denver, Colorado*, 1996.

B. Nœtinger and G. Zargar. Multiscale description and upscaling of fluid flow in subsurface reservoirs. *Oil & Gas Science and Technology*, 59(2):119–139, 2004.

R. Nunes and J. Almeida. Parallelization of sequential gaussian, indicator and direct simulation algorithms. *Computers & Geosciences*, 36(8): 1042–1052, 2010.

R. Nussbaumer, G. Mariethoz, E. Gloaguen, and K. Holliger. Which path to choose in sequential gaussian simulation. *Mathematical Geosciences*, 50:97–120, 2018.

B. Oz, C. Deutsch, T. Tran, and Y. Xie. Dssim-hr: A fortran 90 program for direct sequential simulation with histogram reproduction. *Computers & Geosciences*, 29(1):39–51, 2003.

S. Painter and V. Cvetkovic. Upscaling discrete fracture network simulations: An alternative to continuum transport models. *Water Resources Research*, 41(2):1–10, 2005.

C. L. Palagi and K. Aziz. Use of voronoi grid in reservoir simulation. *SPE Advanced Technology Series*, 2(2):69–77, 1994.

G. Pinder and W. Gray. *Finite Elements Simulation in Surface and Subsurface Hydrology*. Academic Press, New York, 1977.

C. Preux. About the use of quality indicators to reduce information loss when performing upscaling. *Oil & Gas Science and Technology–Revue d'IFP Energies nouvelles*, 71(1):7, 2016.

M. Prévost, F. Lepage, L. Durlofsky, and J.-L. Mallet. Unstructured 3d gridding and upscaling for coarse modelling of geometrically complex reservoirs. *Petroleum Geoscience*, 11:339–345, 2005.

P. Quinlivan, A. Batten, M. Wibowo, S. Hinchliffe, D. Rahayu, I. Doria, A. Yahmadi, and H. Y. T. Tondang. Assessing geothermal tariffs in the face of uncertainty, a probabilistic approach. In *Proceedings World Geothermal Congress*, 2015.

A. Rabinovich, L. Boxiao, and L. J. Durlofsky. Analytical approximations for effective relative permeability in the capillary limit. *Water Resources Research*, 52(10):7645–7667, 2016.

P. Renard. *Modélisation des écoulements en milieux poreux hétérogènes. Calcul des perméabilités équivalentes.* PhD thesis, École des Mines de Paris, 1997.

P. Renard and G. de Marsily. Calculating equivalent permeability: a review. *Advances in Water Resources*, 20(5-6):253–278, 1997.

P. Renard, G. Le Loc'h, E. Ledoux, G. de Marsily, and R. Mackay. A fast algorithm for the estimation of the equivalent hydraulic conductivity of heterogeneous media. *Water Resources Research*, 36(12):3567–3580, 2000.

P. Renard, A. Genty, and F. Stauffer. Laboratory determination of the full permeability tensor. *Journal of Geophysical Research: Solid Earth*, 106(B11):26443–26452, 2001.

R. Romeu and B. Noetinger. Calculation of internodal transmissivities in finite difference models of flow in heterogeneous porous media. *Water Resources Research*, 31(4):943–959, 1995.

P. Samier. Homogénéisation des perméabilités absolues (applications score et progres) - ps 2/90. Report, Société nationale elf aquitaine (production), 1990.

X. Sanchez-Vila, A. Guadagnini, and J. Carrera. Representative hydraulic conductivities in saturated groundwater flow. *Reviews of Geophysics*, 44, 2006.

J. Santiago, M. Claeys-Bruno, and M. Sergent. Construction of space-filling designs using wsp algorithm for high dimensional spaces. *Chemometrics and Intelligent Laboratory Systems*, 113:26–31, 2012.

Schlumberger. Eclipse reservoir simulation software: Reference manual, 2014.

M. Sergent. *Contribution de la Méthodologie de la recherche expérimentale à l'élaboration de matrices uniformes: application aux effets de solvants et de substituants*. PhD thesis, Aix-Marseille 3, 1989.

M. Sergent, R. Phan Tan Luu, and J. Elguero. Statistical analysis of solvent scales. part 1. *Anales de quimica*, 93(2):71–75, 1997a.

M. Sergent, R. Phan Tan Luu, and J. Elguero. Statistical analysis of solvent scales. part 2. *Anales de quimica*, 93(5):295–300, 1997b.

M. Shinozuka and C. M. Jan. Digital simulation of random processes and its applications. *Journal of Sound and Vibration*, 25(1):111–128, 1972.

A. Soares. Direct sequential simulation and cosimulation. *Mathematical Geology*, 33(8):911–926, 2001.

V. C. Tidwell and J. L. Wilson. Laboratory method for investigating permeability upscaling. *Water Resources Research*, 33(7):1607–1616, 1997.

A. F. B. Tompson, R. Ababou, and L. W. Gehlar. Implementation of the three-dimensional turning bands random field generator. *Water Resources Research*, 25(10):2227–2243, 1989.

T. Tran. The "missing scale" and direct simulation of block effective properties. *Journal of Hydrology*, 183(1-2):37–56, 1996.

T. T. Tran, C. V. Deutsch, Y. Xie, et al. Direct geostatistical simulation with multiscale well, seismic, and production data. In *SPE annual technical conference and exhibition*. Society of Petroleum Engineers, 2001.

C. Vogt, D. Mottaghy, A. Wolf, V. Rath, R. Pechnig, and C. Clauser. Reducing temperature uncertainties by stochastic geothermal reservoir modelling. *Geophysical Journal International*, 181(1):321–333, 2010.

J. E. Warren and H. S. Price. Flow in heterogeneous porous media. *Proceedings of the 35^{t}h Annual Fall Meeting of SPE, Denver*, 1960.

R. Weijermars and A. Khanal. High-resolution streamline models of flow in fractured porous media using discrete fractures: Implications for upscaling of permeability anisotropy. *Earth-Science Reviews*, 194: 399–448, 2019.

X.-H. Wen and J. J. Gomez-Hernandez. Upscaling hydraulic conductivities in heterogeneous media: an overview. *Journal of Hydrology*, 183: 9–32, 1996.

O. Wiener. Abhandlungen der mathematish-physischen klasse der koniglichen sachsi-schen gesellschaft der wissenschaften, 1912.

E. Wigniolle and G. Massonnat. Use of well test interpretations to constrain the small scale petrophysical anisotropy (k_v/k_h). *Proceedings of the SPE Reservoir Characterisation and Simulation Conference and Exhibition, Abu Dhabi, UAE*, 2013.

J. B. Witter, W. J. Trainor-Guitton, and D. L. Siler. Uncertainty and risk evaluation during the exploration stage of geothermal development: A review. *Geothermics*, 78:233–242, 2019.

V. Zaytsev. *Méthodes stochastiques pour la modélisation d'incertitudes sur les maillages non structurés*. PhD thesis, PSL Research University, 2016.

V. Zaytsev, P. Biver, H. Wackernagel, and D. Allard. Change-of-support models on irregular grids for geostatistical simulation. *Mathematical Geosciences*, 2015.

H. Zhou, L. Li, and J. Gómez-Hernández. Three-dimensional hydraulic conductivity up-scaling in groundwater modeling. *Computers & Geosciences*, 36(10):1224–1235, 2010.